Since January 2020 Elsevier has created a COVID-19 resource centre with free information in English and Mandarin on the novel coronavirus COVID-19. The COVID-19 resource centre is hosted on Elsevier Connect, the company's public news and information website.

Chemical Engineering Journal 405 (2021) 126806

Contents lists available at ScienceDirect

Chemical Engineering Journal

journal homepage: www.elsevier.com/locate/cej

Review

Recent advances in photodegradation of antibiotic residues in water

Xiuru Yang[a], Zhi Chen[a,*], Wan Zhao[a], Chunxi Liu[a], Xiaoxiao Qian[a], Ming Zhang[b], Guoying Wei[a], Eakalak Khan[c], Yun Hau Ng[d], Yong Sik Ok[e,*]

[a] College of Materials and Chemistry, China Jiliang University, 258 Xueyuan Street, Xiasha Higher Education Zone Hangzhou, 310018, China
[b] Department of Environmental Engineering, China Jiliang University, 258 Xueyuan Street, Xiasha Higher Education Zone Hangzhou, 310018, China
[c] Department of Civil and Environmental Engineering and Construction, University of Nevada, Las Vegas, NV 89154, USA
[d] School of Energy and Environment, City University of Hong Kong, Tat Chee Avenue, Kowloon, Hong Kong Special Administrative Region, China
[e] Korea Biochar Research Center, APRU Sustainable Waste Management & Division of Environmental Science and Ecological Engineering, Korea University, Seoul, South Korea

HIGHLIGHTS

- A summary of key recent advances in photocatalytic removal of antibiotics in water.
- Special emphasis on the strategies for improving the photodegradation efficiency.
- Major challenges and critical perspectives on photocatalysis of antibiotics.

GRAPHICAL ABSTRACT

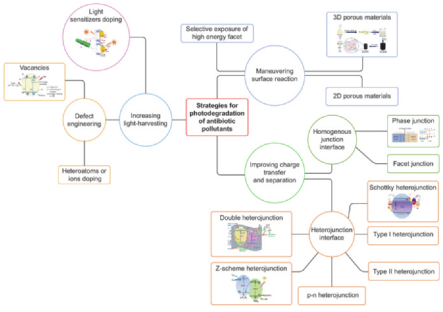

ARTICLE INFO

Keywords:
Clean water and sanitation
Green and sustainable remediation
High-performance photocatalyst
Advanced materials
Reaction mechanisms for photodegradation

ABSTRACT

Antibiotics are widely present in the environment due to their extensive and long-term use in modern medicine. The presence and dispersal of these compounds in the environment lead to the dissemination of antibiotic residues, thereby seriously threatening human and ecosystem health. Thus, the effective management of antibiotic residues in water and the practical applications of the management methods are long-term matters of contention among academics. Particularly, photocatalysis has attracted extensive interest as it enables the treatment of antibiotic residues in an eco-friendly manner. Considerable progress has been achieved in the implementation of photocatalytic treatment of antibiotic residues in the past few years. Therefore, this review provides a comprehensive overview of the recent developments on this important topic. This review primarily focuses on the application of photocatalysis as a promising solution for the efficient decomposition of antibiotic residues in water. Particular emphasis was laid on improvement and modification strategies, such as augmented light harvesting, improved charge separation, and strengthened interface interaction, all of which enable the design of powerful photocatalysts to enhance the photocatalytic removal of antibiotics.

1. Introduction

In the last few decades, antibiotics have been broadly utilized not only for human therapies, such as curing infectious diseases like COVID-19, transplants, chemotherapy, and surgical interventions, but also for therapeutic and non-therapeutic purposes in aquaculture and

* Corresponding authors.
E-mail addresses: zchen@cjlu.edu.cn (Z. Chen), yongsikok@korea.ac.kr (Y. Sik Ok).

https://doi.org/10.1016/j.cej.2020.126806
Received 2 June 2020; Received in revised form 11 August 2020; Accepted 24 August 2020
Available online 31 August 2020

Table 1
Methods for antibiotic degradation or removal in water.

Treatment	Materials	Antibiotic	Operating conditions	Disadvantages	Ref.
Adsorption processes	Anionic surfactant sodium dodecyl sulfate (SDS)	Amoxicillin Ampicillin	Contact time: 40 min Agitation speed: 350 rpm Temperature: 40 °C pH: 4	Low removal capacities; difficult separation; secondary environmental pollution; unsatisfactory recycling ability	[13]
	KOH-modified biochar	Norfloxacin Sulfamerazine Oxytetracycline	Temperature: 15–35 °C pH 3–9		[14]
	Graphene oxide/cellulose nanofibril hybrid aerogel	Doxycycline Chlortetracycline Oxytetracycline Tetracycline	Temperature: 25 °C		[15]
	Pyrogenic carbonaceous materials	Ciprofloxacin	Contact time: 72 h Temperature: 25 °C pH 7.5 and 9.5		[16]
	Clean and dried *Kigelia pinnata* modified with ionic liquid	Ibuprofen Ketoprofen Ampicillin Diclofenac	pH 2.5 or 5		[17]
	Manure-derived biochars	Lincomycin	pH 6 or 10		[18]
	Lanthanum modified diatomite	Tetracycline antibiotics	Contact time: 24 h pH 3–10		[19]
Adsorption processes	Grape stalk	Ofloxacin Chrysoidine	pH 4, 7, and 9	Low removal capacities; difficult separation; secondary environmental pollution; unsatisfactory recycling capacity	[20]
	Cleaned and dried *Pachydictyon coriaceum* and *Sargassum hemiphyllum*	Tetracycline	Temperature: 15–35 °C pH 3–9 Salinity: 0–100 mM NaCl		[21]
	Spent mushroom substrate	Sulfamethyldiazine Sulfamethazine Sulfathiazole Sulfamethoxazole	Temperature: 15 °C pH 3–11		[22]
Coagulation /flocculation /sedimentation	Amino-acid-modified-chitosan flocculants	Norfloxacin Sulfadiazine Tylosin	Temperature: 25 °C pH 6, 7, 8	Antibiotics cannot be completely removed and secondary pollution occurs readily	[23]
Ozonation	Ozone	Amoxicillin Doxycycline Ciprofloxacin Sulfadiazine	Neutral pH	Demands high equipment and energy costs	[24]
	Ozone/zero-valent iron	Flumequine	Contact time: 1h Initial pH 2.5 Fe (0) dosage: 60 g/L Ozone flow rate: 0.25 L/min Temperature: 30 °C		[25]
Ozonation	Medium-high frequency ultrasound and ozone	Amoxicillin	Medium-high ultrasonic frequency waves: 575, 861, 1141 kHz pH 7, 10	Demands high equipment and energy costs	[26]
	Ozone	Flumequine	Contact time: 6 min Temperature: 25 °C pH 3, 5, 7, 9, 11		[27]
	Ozone	Ofloxacin	Temperature: 25 °C pH: 2, 7, 12		[28]
	Multistage ozone and biological treatment system	Amoxicillin	Temperature: 25 °C pH: 10	Complex; high operating costs; continuous use is impractical	[29]
	Chemical coagulation and microfiltration	Ibuprofen Ephedrine Propranolol	Different doses of ZnO nanoparticles: 0.5, 0.7, 1.0, 1.3, 1.5, 1.7 g/L pH 7, 9		[30]
	Electric coagulation and photo-electro-Fenton process	Metronidazole	pH: 1, 3, 5, 7, 9 Metronidazole concentration: 50 mg/L Voltage: 5–30 V H_2O_2: 0–0.02 mol/L Temperature: ~20 °C UV at 230 nm Number of UV lamps: 1–4		[31]
Combined processes	A membrane bioreactor (MBR) integrated with solar Fenton oxidation	Sulfamethoxazole Erythromycin Clarithromycin	H_2O_2: 20–100 mg/L pH: 2.8 [Fe^{2+}]: 5 mg/L	Complex; high operating costs; impracticability in continuous use	[32]
	Integrated adsorption-membrane filtration process	Norfloxacin Ofloxacin	pH: 7 Temperature: 25 °C UV at 276 nm and 293 nm pressure range: 34.47–172.36 kPa		[33]
	Ultraviolet, chlorination, ozone disinfection	Antibiotic resistance genes	Chlorine concentrations: 2–32 mg/L Ozone concentration: 2–10 mg/L UV (mJ/cm^2): 10–160		[34]

(*continued on next page*)

Table 1 (*continued*)

Treatment	Materials	Antibiotic	Operating conditions	Disadvantages	Ref.
	Adsorptive magnetic ion exchange resin	Sulfamethoxazole Tetracycline Amoxicillin	Contact time: 30 min Temperature: 25 °C MIEX resin dosage: 5 mL/ LAntibiotic: 1000 μg/L		[30]
	Nanofiltration and chlorination	Sulfanilamide Sulfadiazine Sulfamethoxazole Sulfadimethoxine	Membrane effective area: 40.92 cm^2 Operating pressure: 5 bar Temperature: 25 °C Flow rate: 120–150 mL/min Initial pH: 5.6, 7.2, 10 Initial concentration: 2.0×10^{-5} M		[35]

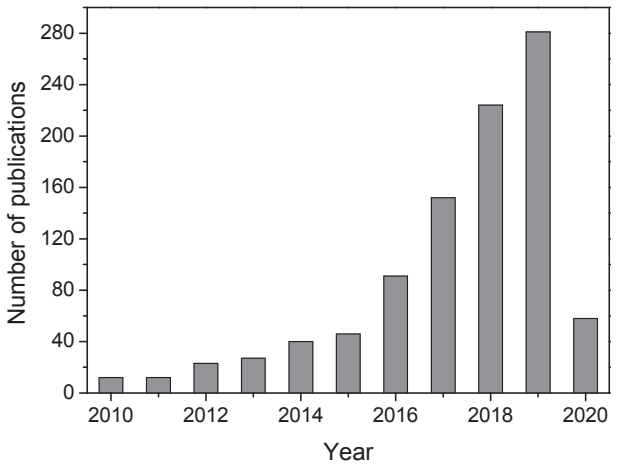

Fig. 1. Number of search results of recent publications addressing the photocatalytic treatment of antibiotic residues using "photocatalytic" and "antibiotic treatment" as keywords (collected from the Web of Science Core Database: March 9, 2020).

animal husbandry and for enhancing crop production [1,2]. However, the use and overuse as well as the delayed metabolism of antibiotics have led to the inevitable discharge of their residues into aquatic environments, resulting in refractory pollution sources [3]. Conventional wastewater treatment plants (WWTPs) cannot efficiently remove antibiotic residues [4,5]. This leads to their distribution into ecological systems [6,7] and eventually into the human body through the food chain or drinking water [8–10]. Moreover, the long residence times of antibiotic residues in aquatic environments, even at low concentrations, may lead to the propagation of bacteria with antibiotic resistance and even multiple drug resistance, which may cause life-threatening infections [3,11,12]. Therefore, developing an effective approach to degrade or remove antibiotic residues from aquatic environments is crucial.

Different methods have been developed to treat antibiotic residues in water and wastewater before their final release into the environment. Table 1 summarizes the current main approaches, including traditional techniques and newly developed methods.

These current methods can be loosely classified into three types according to the treatment mechanisms or principles involved: physical removal, biological treatment, and chemical degradation. As shown in Table 1, physical methods such as adsorption, sedimentation, flocculation, and filtration only separate the antibiotic residues from the water and generate problematic products such as brine and contaminated adsorbents. Alternatively, biological approaches have recently emerged, and most antibiotic residues in the environment can be removed through this route [36–38]. However, the artificial introduction of active organisms into aquatic environments may disrupt the ecological balance of their biomes, which may cause irreversible ecosystem damage. Moreover, biological processes suffer from some key disadvantages such as being time-consuming and often unreliable. Therefore, the chemical degradation of antibiotics has gained strong interests.

Different chemical approaches such as ozonation, chlorination, and Fenton's oxidation have been developed for the treatment of antibiotic residues in water, as shown in Table 1. Unfortunately, complete mineralization is difficult to achieve or may otherwise be prohibitively lengthy. In some cases, these methods may kill non-target organisms due to their low selectivity, which causes unintended damages [39,40]. Additionally, this method incurs high capital and high operating costs. Combinations of physical and chemical degradation processes can significantly reduce the toxicity of treated effluents during the removal of antibiotic residues from water. Nevertheless, these methods are complex and costly [41].

Alternatively, photocatalysis has broad application prospects for environmental remediation due to its unique advantages, including (1) easily-attainable reaction conditions (i.e., near ambient temperature and mostly ambient pressure), the use of oxygen in the air to produce a powerful oxidant, and the use of solar radiation as an energy source; (2) potentially complete decomposition of organic pollutants into innocuous inorganic molecules such as carbon dioxide and water; (3) strong redox ability, low cost, no adsorption saturation, and long durability. Therefore, photocatalysis has increasingly garnered worldwide interest and has been broadly implemented in novel energy extraction and environmental control strategies.

Photocatalysis is an advanced oxidation process that has previously been applied in the treatment of antibiotic residues. As shown in Fig. 1, less than 40 studies had been published on the photocatalytic treatment of antibiotic residues, prior to 2014. However, a sharply increasing number of publications on this subject have been released thereafter. Substantial progress has been made in recent years; however, photocatalysis still suffers from some key imperfections, including insufficient visible light utilization, rapid annihilation of photogenerated carriers, and incomplete mineralization, all of which strongly restrict its commercial application. A thorough overview concerning the fundamentals, improvement, and modification of strategies and challenges of the photocatalytic treatment of antibiotic residues was yet to be compiled, and therefore, these topics have been comprehensively addressed herein.

This article comprehensively reviews the latest advances in the photocatalytic treatment of antibiotic residues in water. Specifically, the fundamentals of photocatalysis will be introduced. Different strategies will then be summarized and classified, followed by a discussion on the improvement and modification strategies to enhance the photocatalytic degradation of antibiotics. Finally, this review will conclude with a summary of major challenges and key perspectives.

2. Basic principles of photodegradation

When a semiconductor is exposed to irradiation with energy beyond its optical band gap, electrons are excited and shifted from its valence band (VB) towards the conduction band (CB), producing an equal number of positively charged holes in the VB. When the potential of VB

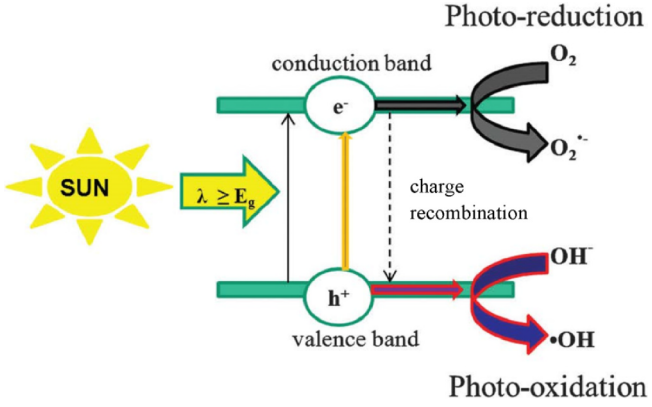

Fig. 2. Schematic representation of the semiconductor photocatalysis process [44]

vs NHE is more positive than $H_2O/\bullet OH(+2.72VvsNHE)$ or $OH^-/\bullet OH(+1.89VvsNHE)$, and the potential of CB vs NHE is more negative than$O_2/\bullet O_2^-(-0.33$ V vs NHE), the semiconductor will be able to generate •OH and $\bullet O_2^-$. Thereafter, the photoinduced electrons and holes separate and migrate to the surface of the semiconductor, and redox reactions will occur at the reactive site on the semiconductor surface (Fig. 2) [42,43].

The reaction mechanisms of semiconductor photocatalysis are typically expressed by the following equations [45,46]:

Semiconductor + Light Energy ($\lambda \geq E_g$)→ Semiconductor ($e_{cb}^- + h_{vb}^+$) (1)

$h_{vb}^+ + H_2O \rightarrow H^+ + \bullet OH$ ($H_2O/\bullet OH$| + 2.72VvsNHE) (2)

$h_{vb}^+ + OH^- \rightarrow \bullet OH$ ($OH^-/\bullet OH$| + 1.89VvsNHE) (3)

$e_{cb}^- + O_2 \rightarrow \bullet O_2^-$ ($O_2/\bullet O_2^-$| − 0.33 V vs NHE) (4)

Pollutant + Active species (h_{vb}^+, e_{cb}^-, •OH, $\bullet O_2^-$)→Degradation Products (5)

Through these chemical processes, solar energy can be directly converted and effectively utilized. For instance, Zhao *et al.* [47] successfully prepared ZnSe quantum dot (QD)/g-C_3N_4 composites with remarkable photocatalytic properties and utilized them for the photocatalytic degradation of ceftriaxone sodium. Based on the results, •OH and h^+ were found to be the main active materials. The potential reaction mechanisms are described below.

ZnSe QDs/g-C_3N_4 + hν → $h^+ + e^-$

$h^+ + H_2O \rightarrow H^+ + \bullet OH$

$e^- + 1/2O_2 + H^+ \rightarrow \bullet OH$

h^+ + •OH + Ceftriaxone sodium → $CO_2 + H_2O$ + other small molecules

However, limited optical utilization and the quick annihilation of photoexcited electron-hole pairs diminish the effects of photocatalytic activity. Photocatalysts are able to overcome these deficits, provided that they meet the following criteria: (1) appropriate spectral absorption range, (2) proper band energy structure for sufficient separation and transport of electron–hole pairs, and (3) adequate active sites for adsorption or reaction [48–50]. It is essential to satisfy all three of the aforementioned prerequisites to improve photocatalytic efficiency, and abundant efforts have been made to systematically design photocatalysts and optimize photocatalytic dynamics.

3. Strategies for photocatalytic activity improvement

The photocatalytic treatment of antibiotic residues in aquatic environments has recently become the focus of much attention, and diverse strategies have been proposed to improve the photocatalytic efficiency (Scheme 1). Examples of such reported strategies are summarized in Table 2.

3.1. Strategies to increase light harvesting

3.1.1. Defect engineering to increase light harvesting

Defects play two distinct roles in the photocatalytic process: (1) they act as trapping sites for electrons or holes. Depending on the nature of the defects (deep trap or shallow trap), it may improve the diffusion length of charge carriers (shallow trap) or promote the charge recombination (deep trap) thus reducing the photocatalytic efficiency; (2) they may extend the light absorption by modulating the electronic structure of the photocatalyst (e.g. creation of midgap impurities level), thereby influencing the photocatalytic activity. However, elaborative designs such as vacancy construction and elemental doping are necessary to take full advantage of the improvements and avoid or minimize the disadvantages [187–190].

3.1.1.1. Vacancies for the improvement of light absorption. Vacancies are types of point defects that not only manipulate the composition of catalysts without introducing impurities but also allow for the customization of suitable band structures by modulating their types and concentrations. The concentration of the vacancies should be controlled within a delicately balanced range. Excessive vacancies would provide too many recombination centers for photoinduced electrons and holes, whereas insufficient vacancies would fail to achieve the desired photocatalytic performance. Vacancies may be categorized into three types: 1) anion vacancies (such as sulfur [191–195], halogen [196–199], nitrogen [200–202] and oxygen vacancies (OV) [203–207]), 2) cationic vacancies (such as bismuth [208–210], carbon [211] and titanium vacancies [212–215]), and 3) mixed vacancies, which combine anion and cation vacancies [216,217]. For example, mesoporous ZrO_2 containing abundant oxygen vacancies was successfully synthesized by Zhang *et al.* [52] via a template-less solvothermal approach, following calcination. The absorption edge of the obtained sample was extended into the visible range, and the modified surface characteristics promoted adsorption ability towards organic compounds, leading to an enhancement of the visible-light-driven photodegradation of organic contaminants. Similarly, brown $ZnWO_{4-x}$ nanorods containing oxygen vacancies exhibited a broadened photo-absorption capacity from the ultraviolet (UV) to the near-infrared (NIR) region, whereas conventional white $ZnWO_4$ nanorods without OV exhibited a UV absorption onset at 365 nm [54].

Fig. 3 shows the existence of an OV-mid-gap state and three possibilities for electron excitation: (i) UV-driven direct excitation from the VB towards the CB, (ii) visible-light-induced jump from VB to OV defect states, and (iii) near-infrared-light-driven transition from the OV-derived defect state to the CB [54]. The induced defect, or the inter-band energy level, enables electron jumps with less energetic illumination, thereby improving the light harvest capacity of $ZnWO_{4-x}$ nanorods with abundant OV [54]. Moreover, Liu *et al.* [218] reported that anion vacancy could be produced in a TiO_2 lattice when Ti^{3+} was present. Excess energy levels below the CB would be induced in the presence of these anion vacancies [219–222]. Overlapping of these levels with CB occurs by increasing the concentration of these vacancies, resulting in a decreased bandgap of TiO_2. Therefore, the visible-light-driven transition can take place from intrinsic VB to Ti^{3+} states. This behavior can extend the optical response to an onset wavelength of longer than 400 nm [223].

3.1.1.2. Heteroatoms or ion doping for light response improvement. The introduction of heteroatoms or ions into the photocatalyst, in the form of dopant, is an effective light response management method. Nonmetal dopants (e.g., C [224,225], B [226–229], P [57,230], S [231,232], N [233–236], and halogen [237,238]) and metallic dopants (e.g. Fe^{3+} [239,240], Ce^{3+} [62], Cr^{3+} [241], W^{6+} [242], Ti^{4+} [243], Cu^{2+} [241], Co^{2+} [244,245] and Er^{3+} [246]) were most widely studied in semiconductor photocatalysts, especially metal oxides. Generally, a method can either introduce an impurity energy

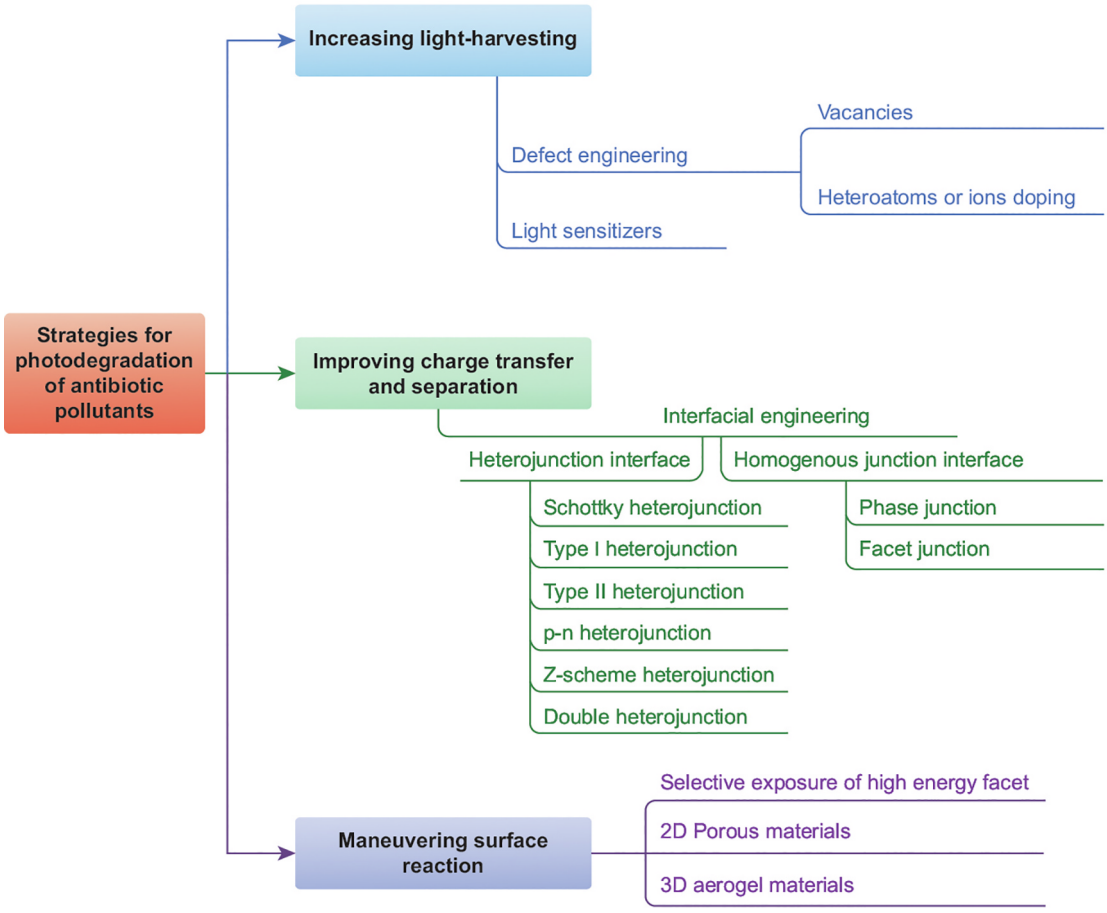

Scheme 1. Strategies for photocatalytic efficiency improvement.

level lower than the CB minimum or higher than the VB maximum to narrow down the bandgap, enhancing light absorption.

Recently, N-doped TiO_2 photocatalysts with tunable doping contents were prepared by calcining sol–gel TiO_2 powder in the presence of NH_3 flow at 450–800 °C [247]. The light absorption capacity of samples prepared at a temperature region of 450–600 °C increased gradually with temperature, and their colors varied from pale yellow to emerald green as a result of the production of N 2p (localized states) beyond the VB of TiO_2 and the generation of OV (Fig. 4(a)). When NH_3 treatment reached T > 600 °C, anatase TiO_2 was transformed into rutile, leading to a remarkable reduction in its Brunauer-Emmett-Teller (BET) area and the production of a TiN layer on the TiO_2 surface. The materials treated at 700 and 800 °C exhibited a conspicuous response to a wide range of spectra spanning from the visible to the NIR range, which originated from the production of OV and Ti^{3+} defects. Similarly, Wang *et al.* [248] synthesized lantern-shaped g-C_3N_4 with a Eu^{3+} dopant and found that a doping level was developed below the CB upon the introduction of Eu^{3+}, resulting in a narrower bandgap and lowering the electron position compared to that of raw CN. This improved both the optical light response and photocatalytic performance.

In some cases, co-doping (e.g., the addition of two non-metals [57,231], two metal ions [246], or a metal ion paired with a non-metal ion [63]) has been used to avoid imbalances of charges during aliovalent doping [187]. For example, b/N-TDHG (black Ti^{3+}/N co-doped TiO_2/diatomite hybrid granule) could be obtained from a sol–gel process [63]. The light absorption of b/N-TDHG (Fig. 4(b)) exhibited a more pronounced redshift than other TDHG counterparts. Particularly, it had the strongest visible-light response among all obtained photocatalysts, which resulted from the synergistic action of co-doped N and Ti^{3+}.

3.1.2. Addition of light sensitizers to enhance light absorption

The addition of photosensitizers is another simple method of enhancing the photoactivity of wide bandgap semiconductors in visible light. In recent years, a variety of QDs (e.g., ZnSe QDs [47], carbon QDs (CQDs) [64–66,68,69,249–253], graphene [254], CdS [255,256], Fe_3O_4 [257], g-C_3N_4 [258], $CsPbBr_3$ [259] and MoS_2 [260]) have been combined into semiconductors to enhance light absorption. Among them, CQDs have become the most widely used QDs to upgrade wide-bandgap semiconductors owing to their low cost, non-toxicity, and high stability [250,261]. For example, up-converting CQDs were immobilized on the surface of $La_2Ti_2O_7$ (LTO) nanosheets to promote visible-light-induced photocatalysis [252]. The pristine (i.e., unmodified) LTO nanosheets had no optical response from 400 to 800 nm (Fig. 5(a)). In contrast, all CQD/$La_2Ti_2O_7$ (C-LTO) composites exhibited distinct responses in the above range, and the response could be modulated accordingly by changing the amount of CQD.

Zhao *et al.* [253] successfully synthesized TiO_2 nanotube (CQD/TNTs) composites with an outstanding photocatalytic performance. These CQD co-catalysts had remarkable up-converting photoluminescence (PL) features. Longwave infrared rays (LWIR, > 600 nm) absorption could be converted into optical light of shorter than 600 nm, enabling the production of IR-induced electrons and holes on TNTs (Fig. 5(b)). Additionally, the introduction of CQDs can accelerate the harvesting of photoexcited electrons and prolong the lifetime of photoinduced carriers.

3.2. Interfacial engineering strategies for carrier migration improvement

The construction of a junction interface is a typical approach to facilitate photocatalysis by modulating the separation/migration of the

Table 2
Summary of previous studies using different strategies to improve photocatalytic degradation of antibiotics.

Strategies	Catalysts and concentration	Light source	Antibiotic and concentration	Degradation efficiency	Ref.
Vacancies	BiOCl with abundant oxygen vacancies 0.5 g/L	300-W Xe lamp ($\lambda > 420$ nm)	Tetracycline hydrochloride 10 mg/L	Approximately 87% optimum within 2 h	[51]
Vacancies	Oxygen vacancy-rich mesoporous ZrO_2 1 g/L	300-W Xe lamp ($\lambda > 420$ nm)	Tetracycline hydrochloride 40 mg/L	Approximately 80% optimum within 150 h	[52]
Vacancies	BiOBr microspheres with oxygen vacancies 1 g/L	10-W LED lamp (0.4 $mW{\cdot}cm^{-2}$)	Tetracycline (TC) 20 mg/L	Approximately 94% optimum within 90 min	[53]
Vacancies	$ZnWO_{4-x}$ nanorods with oxygen vacancy 0.2 g/L	Hg lamp 300-W UV or 300-W Xe lamp (UV–Vis-NIR)	Tetracycline 20 mg/L	Approximately 91% optimum within 90 min	[54]
Vacancies	Bi_2MoO_6 with oxygen vacancy 0.4 g/L	300-W Xe lamp ($\lambda > 400$ nm)	Ciprofloxacin 20 mg/L	Approximately 55% optimum within 120 min	[55]
Doping	Carbon-doped g-C_3N_4 0.5 g/L	Sunlight	Tetracycline 20 mg/L	Approximately 90% optimum within 90 min	[56]
Doping	P-O co-doped g-C_3N_4 1 g/L	350-W Xe lamp ($\lambda > 420$ nm)	Enrofloxacin10 mg/L	Approximately 90% within 80 min	[57]
Doping	I and K co-doped g-C_3N_4 2 g/L	300-W Xe lamp ($\lambda > 420$ nm)	Sulfamethoxazole 10 mg/L	Approximately 99% optimum within 45 min	[58]
Doping	Bi^{3+}/g-C_3N_4 0.2 g/L	300-W Xe lamp ($\lambda > 420$ nm)	Tetracycline 10 mg/L	Approximately 94% optimum within 30 min	[59]
Doping	Cr^{3+}/$SrTiO_3$ 1 g/L	250-W Xe lamp ($\lambda > 420$ nm)	Tetracycline 10 mg/L	Approximately 70% optimum within 60 min	[60]
Doping	Fe^{2+}/Fe^{3+} immobilized on TiO_2/fly-ash cenospheres 2 g/L	150-W tungsten halogen lamp ($\lambda > 420$ nm)	Ciprofloxacin 10 mg/L	Approximately 80% optimum within 60 min	[61]
Doping	Ce^{3+} doped Bi_2O_3 0.6 g/L	300-W lamp (visible light)	Tetracycline 20 mg/L	Approximately 89% optimum within 180 min	[62]
Doping	Ti^{3+}/N co-doped TiO_2/diatomite granule 5 g/L	150-W Xenon lamp with a UV light filter	Tetracycline 10 mg/L	92% optimum within 150 min	[63]
Quantum dots	CQDs modified Bi_2MoO_6 1 g/L	300-W Xe lamp ($\lambda > 400$ nm)	Ciprofloxacin 20 mg/L	88% optimum within 2h	[64]
Quantum dots	CQDs/BiOBr microspheres 1 g/L	Visible light irradiation	Ciprofloxacin 1 g/L	Approximately 65% optimum within 180 min	[65]
Quantum dots	TiO_2/C-dots 0.1 g/L-0.5 g/L	Average intensity sunlight irradiation (72 klx)	Levofloxacin 10 mg/L	Approximately 99% optimum within 90 min	[66]
Quantum dots	ZnSe QDs/g-C_3N_4 Not provided	300-W Xe lamp ($\lambda > 400$ nm)	Ceftriaxone sodium Concentration not provided	Approximately 80% optimum within 120 min	[47]
Quantum dots	Ag_2O/TiO_2 quantum dots 0.25 g/L	400-W halogen bulb (similar to sunlight)	Levofloxacin 10 mg/L	Approximately 81% optimum within 90 min	[67]
Quantum dots	CQDs/BiOI 0.5 g/L	300-W Xe lamp ($\lambda > 400$ nm)	Tetracycline 20 mg/L	Approximately 70% optimum within 120 min	[68]
Quantum dots	CQDs/BiOBr 0.3 g/L	300-W Xe lamp ($\lambda > 400$ nm)	Tetracycline 20 mg/L	Approximately 60% optimum within 120 min	[69]
Quantum dots	MoS_2 modified Zn-$AgIn_5S_8$ quantum dots 0.1 g/L	250-W Xe lamp ($\lambda > 420$ nm)	Tetracycline 10 mg/L	Approximately 74% optimum within 4 min	[70]
Quantum dots	3D ZnS-RGO nanospheres 1 g/L	300-W Hg vapor lamp	Norfloxacin 20 mg/L	92% optimum within 4h	[71]
Phase junction	Porous core–shell homojunction 0.5 g/L	UV lamp (254 nm, 90 W, Philips)	Tetracycline hydrochloride 50 mg/L	Approximately 81% within 300 min	[72]
Facet junction	$CaCu_3Ti_4O_{12}$ Co-exposed (0 0 1) and (1 1 1) facets 0.4 g/L	300-W Xe lamp visible light	Tetracycline 0.24 g/L	Approximately 99% within 50 min	[73]
Facet junction	AgBr tetradecahedrons with co-exposed (1 0 0) and (1 1 1) facets 1 g/L	500-W halogen tungsten lamp ($\lambda > 420$ nm)	Sulfadiazine 20 mg/L	Approximately 90% optimum within 90 min	[74]
Schottky heterojunction	Ag/Ag_2MoO_4 0.4 g/L	500-W Xe lamp ($\lambda > 420$ nm)	Ciprofloxacin 20 mg/L	Approximately 99% optimum within 60 min	[75]
Schottky heterojunction	Ag/TiO_2 (hollow nanosphere) 0.5 g/L	125-W high-pressure Hg lamp, ($\lambda > 435.8$ nm)	Metronidazole 15 mg/L	Approximately 95% optimum within 120 min	[76]
Schottky heterojunction	Bi/BiOBr (nano-flowers) 0.8 g/L	300-W Xe lamp ($\lambda > 420$ nm)	Tetracycline hydrochloride Ciprofloxacin and Doxycycline 1 g/L	Approximately 100% optimum within 30 min	[77]
Schottky heterojunction	BiOCl-Ag (2D) 1.0 g/L	200-W Xe arc lamp ($\lambda < 420$ nm)	Sulfonamides 10 mg/L	Approximately 80% optimum within 5h	[78]
Schottky heterojunction	Ag/Bi_3O_4Cl 0.5 g/L	250-W Xe lamp ($\lambda > 420$ nm)	Tetracycline 10 mg/L	Approximately 94% optimum within 120 min	[79]
Schottky heterojunction	Ag/CCN 0.5 g/L	300-W Xe lamp ($\lambda > 420$ nm)	Tetracycline 10 mg/L	75% optimum within 15 min	[80]
Schottky heterojunction	Pt/g-C_3N_4 0.5 g/L	300-W Xe lamp ($\lambda > 400$ nm)	Tetracycline hydrochloride 20 mg/L	Approximately 84% optimum within 40 min	[81]
Schottky heterojunction	Bi (Spheres)/g-C_3N_4 0.5 g/L	300-W Xe lamp ($\lambda > 420$ nm)	Amoxicillin 100 mg/L	Approximately 5% optimum within 4 h	[82]
Schottky heterojunction	W-doped $BaTiO_3$ 0.2 g/L	Visible light irradiation	Tetracycline 20 mg/L	Approximately 80% optimum within 3h	[83]
Schottky heterojunction	Fe, Co, Ni, Fe-Co-, and Fe-Ni-doped ZnO 0.6 g/L	300-W Xe lamp ($\lambda = 365$ nm)	Oxytetracycline 20 mg/L	Approximately 87% optimum within 2h	[84]

(*continued on next page*)

Table 2 (*continued*)

Strategies	Catalysts and concentration	Light source	Antibiotic and concentration	Degradation efficiency	Ref.
Schottky heterojunction	Pt/Bi/TiO_2 1 g/L	300-W halogen-tungsten lamp (λ > 420 nm)	Amoxicillin 10 mg/L	Approximately 87% optimum within 2h	[85]
Schottky heterojunction	Au/Pt/g-C_3N_4 1 g/L	500-W Xe lamp (λ > 400 nm)	Tetracycline hydrochloride 20 g/L	Approximately 90% optimum within 3h	[86]
Schottky heterojunction	0D Bi nanodots/2D Bi_3NbO_7 nanosheets 0.5 g/L	300-W Xe lamp (λ > 400 nm)	Ciprofloxacin 10 mg/L	Approximately 86% optimum within 120 min	[87]
Type II heterojunction	AgI/$BiVO_4$ 0.3 g/L	300-W Xe lamp (λ > 420 nm)	Tetracycline (TC) 20 mg/L	Approximately 94% optimum within 1h	[88]
Type II heterojunction	3D porous CdS/TiO_2 1 g/L	300-W Xe lamp (λ > 420 nm)	Tetracycline and oxytetracycline (OTC) 40 mg/L	Approximately TC: 67% and OTC: 81% optimums within 50 min	[89]
Type II heterojunction	$MgFe_2O_4/MoS_2$	Radiation intensity: 47 mW/cm^2	Tetracycline 10 mg/L	Approximately 92% optimum within 120 min	[90]
Type II heterojunction	$ZnWO_4$-CdS 1 g/L	300-W Xe lamp (λ > 420 nm)	Ciprofloxacin 15 mg/L	Approximately 90% optimum within 1h	[91]
Type II heterojunction	ZnO@ZnS nanorod 3 × 3 cm chip	500-W Xe lamp	Tetracycline 10 mg/mL	Approximately 80% within 140 min	[92]
Type II heterojunction	$MoS_2/PbBiO_2I$ 0.3 g/L	300-W Xe lamp (λ > 400 nm)	Ciprofloxacin 10 mg/L	Approximately 80% optimum within 6h	[93]
Type II heterojunction	$Bi_2SiO_5/Bi_{12}SiO_{20}$ 1 g/L	100-W high-pressure Hg lamp	Tetracycline 10 mg/L	Approximately 79% optimum within 30 min	[94]
Type II heterojunction	$SrTiO_3/Fe_2O_3$ 1 g/L	250-W Xe lamp (λ > 420 nm)	Tetracycline 10 mg/L	Approximately 83% optimum within 140 min	[95]
Type II heterojunction	p-C_3N_4/f-BiOBr 1 g/L	250-W Xe lamp (λ > 400 nm)	Tetracycline 30 mg/L	Approximately 94% optimum within 300 min	[96]
Type II heterojunction	$Bi_2O_7Sn_2$-$Bi_7O_9I_3$ 1 g/L	Halogen lamp as simulated solar light	Tetracycline 35 mg/L	80% optimum within 90 min	[97]
Type II heterojunction	$NiFe_2O_4/Bi_2O_3$ 1 g/L	150-W xenon lamp (λ > 420 nm)	Tetracycline 10 mg/L	Approximately 91% optimum within 90 min	[98]
Type II heterojunction	$BiVO_4$/rGO 0.9 g/L	250-W Xe lamp (λ > 420 nm)	Tetracycline 25 mg/L	99% optimum within 90 min	[99]
Type II heterojunction	$SrTiO_3$ nanocube coated CdS microsphere 1 g/L	250-W Xe lamp (λ > 400 nm)	Ciprofloxacin 10 mg/L	Approximately 94% optimum within 120 min	[100]
Type II heterojunction	g-$C_3N_4/BiPO_4$ 0.3 g/L	250-W high-pressure Hg lamp	Ciprofloxacin 10 mg/L	Approximately 97% optimum within 120 min	[101]
Type II heterojunction	g-C_3N_4/Ag_3PO_4 0.5 g/L	300-W Xe lamp (λ > 400 nm)	Ciprofloxacin Concentration not provided	Approximately 67% optimum within 15 min	[102]
Type II heterojunction	$In_2S_3/NaTaO_3$ 0.5 g/L	300-W Xe lamp	Tetracycline hydrochloride 10 mg/L	Approximately 80% optimum within 180 min	[103]
Type II heterojunction	Polyaniline/$Bi_4O_5Br_2$ 0.4 g/L	Visible light (λ > 420 nm)	Ciprofloxacin 10 mg/L Tetracycline 20 mg/L	CIP: 99% optimum within 50 min, TC: approximately 86% optimum within 240 min	[104]
Type II heterojunction	CdS nanoparticles/porous carbon polyhedrons 1 g/L	300-W Xe lamp (λ > 420 nm)	Cephalexin 20 mg/L	Approximately 90% optimum within 90 min	[105]
Type II heterojunction	Microsphere-like $In_2S_3/InVO_4$ 0.5 g/L	300-W Xe lamp (λ > 420 nm)	Tetracycline 10 mg/L	Approximately 71% optimum within 60 min.	[106]
Type II heterojunction	g-$C_3N_4/Bi_4O_5Br_2$ 0.5 g/L	300-W Xe arc lamp	Ciprofloxacin 10 mg/L	Approximately 67% optimum within 150 min	[107]
Type II heterojunction	Bi_2WO_6/g-C_3N_4 1 g/L	300-W Xe lamp UV light	Ceftriaxone sodium 10 mg/L	Approximately 94% optimum within 120 min	[108]
Type II heterojunction	Flower-root shaped Bi_2O_3/Bi_2MoO_6 0.4 g/L	500-W Xe lamp (λ > 420 nm)	Tetracycline 10 mg/L	Approximately 70% optimum within 190 min	[109]
Type II heterojunction	Covalent triazine framework modified BiOBr nanoflake 0.2 g/L	500-W Xe lamp	Tetracycline 10 mg/L Ciprofloxacin 10 mg/L	Approximately TC: 90% and CIP: 60% optimums within 50 min	[110]
Type II heterojunction	mpg-C_3N_4 and Bi_2WO_6 nest-like structure 0.5 g/L	300-W Xe lamp (λ > 420 nm)	Tetracycline hydrochloride 50 mg/L	Approximately 75% optimum within 120 min	[111]
Type II heterojunction	TiO_2 nanoparticle/$SnNb_2O_6$ nanosheet heterojunctions 1 g/L	500-W tungsten lamp	Tetracycline hydrochloride 35 mg/L	Approximately 76% optimum within 240 min	[112]
Type II heterojunction	$Bi_4Ti_3O_{12}$/BiOCl (2D/0D) composite 0.67 g/L	300-W Xe lamp	Tetracycline hydrochloride 20 mg/L	Approximately 84% optimum within 150 min	[113]
Type II heterojunction	2D-2D g-$C_3N_4/Bi_4O_5Br_2$ 0.1 g/L	300-W Xe lamp (λ > 400 nm)	Ciprofloxacin 10 mg/L	Approximately 50% optimum within 30 min	[114]
Type II heterojunction	2D/2D $Bi_4Ti_3O_{12}$/I-BiOCl 0.375 g/L	350-W Xe arc lamp (λ > 420 nm)	Ciprofloxacin 10 mg/L Tetracycline hydrochloride 10 mg/L	Approximately 90% optimum within 120 min	[115]
Type II heterojunction	Carbon-doped carbon nitride/$Bi_{12}O_{17}Cl_2$ 1 g/L	300-W Xe lamp (λ > 420 nm)	Tetracycline 20 mg/L	94% optimum within 60 min	[116]
Type II heterojunction	$CuBi_2O_4$/CuO 1 g/L	Visible light (λ > 400 nm)	Metronidazole 50 mg/L	36% optimum within 120 min	[46]

(*continued on next page*)

Table 2 (*continued*)

Strategies	Catalysts and concentration	Light source	Antibiotic and concentration	Degradation efficiency	Ref.
p-n heterojunction	p-n type BiOCl/titanium phosphate nanoplates 0.4 g/L	300-W Xe lamp	Ciprofloxacin 5 mg/L	Approximately 100% within 5 min	[117]
p-n heterojunction	p-n type CoO/g-C_3N_4 0.5 g/L	300-W Xe lamp (λ > 420 nm)	Tetracycline 10 mg/L	Approximately 90% within 60 min	[118]
p-n heterojunction	p-n type $Cu_2O/SrTiO_3$ 1 g/L	150-W Xe lamp (λ > 420 nm)	Tetracycline 10 mg/L	Approximately 79% within 100 min	[119]
p-n heterojunction	p-n type flower-like BiOCl/BiOCOOH p-n 1 g/L	300-W Xe lamp simulated sunlight	Tetracycline 20 mg/L	Approximately 80% within 60 min	[120]
p-n heterojunction	p-n type Ag_2O/g-C_3N_4 1 g/L	500-W Xe lamp (λ > 400 nm)	Tetracycline hydrochloride 20 mg/L	Approximately 94% within 3h	[121]
p-n heterojunction	p-n type Co_3O_4-C_3N_4 0.5 g/L	Sunlight	Tetracycline 48 mg/L	Approximately 97% within 180 min	[122]
p-n heterojunction	p-n type 3D flower-like BiOBr/Bi_2SiO_5 1 g/L	300-W Xe lamp (λ > 420 nm)	Tetracycline 20 mg/L	91% within 120 min	[123]
p-n heterojunction	n-p type SnO_2 nanoparticles/BiOI 1 g/L	300-W Xe lamp (λ > 420 nm)	Oxytetracycline hydrochloride 10 mg/L	Approximately 94% optimum within 90 min	[124]
p-n heterojunction	p-n type N-graphene QDs-BiOI/$MnNb_2O_6$ 0.5 g/L	250-W Xe lamp (λ > 420 nm)	Tetracycline 10 mg/L	Approximately 87% optimum within 60 min	[125]
p-n heterojunction	p-n type Fe_3O_4 quantum dots modified BiOCl/$BiVO_4$ 0.5 g/L	300-W Xe lamp (λ > 420 nm)	Sulfamethoxazole (SMX, 5 mg/L), TC (20 mg/L), norfloxacin (NOR, 10 mg/L), and CIP (10 mg/L)	SMX: 91% within 90 min, TC: 87% within 30 min, NOR: 89% within 60 min, CIP: 87% within 90 min	[126]
Double heterojunction	CDs/MoS_2/TiO_2 nanobelt 0.5 g/L	250-W Xe lamp (λ > 420 nm)	Tetracycline 10 mg/L	Approximately 82% within 3h	[127]
Double heterojunction	(g-C_3N_4)-ZnO/halloysite nanotubes (HNTs) 1 g/L	350-W Xe arc lamp	Tetracycline 20 mg/L	Approximately 87% optimum within 60 min	[128]
Double heterojunction	Ultrathin g-C_3N_4 nanosheets coupled with amorphous Cu doped FeOOH nanoclusters as 2D/0D heterogeneous catalysts 0.2 g/L	500-W Xe lamp (λ > 420 nm)	Tetracycline 10 mg/L	Approximately 90% within 40 min	[129]
Double heterojunction	2D/2D/2D CoAl-LDH/g-C_3N_4/RGO ternary heterojunction 0.25 g/L	300-W halogen lamp visible-light irradiation	Tetracycline 20 mg/L	Approximately 100% optimum within 60 min	[130]
Double heterojunction	Ag-$AgVO_3$/g-C_3N_4 0.2 g/L	300-W Xe lamp (λ > 410 nm)	Tetracycline 30 mg/L	Approximately 84% optimum within 120 min	[131]
Double heterojunction	$ZnFe_2O_4$/Ag/Ag_3VO_4 1 g/L	Visible-light irradiation	Tetracycline 10 mg/L	Approximately 60% within 10 min	[132]
Double heterojunction	NiS and MoS_2 nanosheet co-modified g-C_3N_4 ternary heterostructure 1 g/L	250-W metal halide lamp (λ > 400 nm)	Tetracycline 10 mg/L Ciprofloxacin 10 mg/L	Approximately CIP: 71% and TC: 96% optimums, within 120 min	[133]
Double heterojunction	AgCl/Ag_3PO_4/ g-C_3N_4 1 mg/L	Visible-light irradiation (λ > 400 nm)	Sulfamethoxazole 50 mg/L	Approximately 100% optimum within 90 min	[134]
Double heterojunction	3D Ag_3PO_4/TiO_2@MoS_2 0.5 g/L	800-W Xe arc lamp	OTC 5 mg/L ENR 5 mg/L	Approximately OTC: 75%, ENR: 92% within 10 min	[135]
Double heterojunction	Bi_2O_3/BiOCl supported on graphene sand (BO/BOC/GSC) composite (BO/BOC/CT) 0.5 g/L	Solar light intensity (35 × 103 ± 1000 lx)	Oxytetracycline 46 mg/L Ampicillin 37 mg/L	BO/BOC/GSC: approximately 90% for AMP and OTC BO/BOC/CT: approximately 80% for AMP and OTC	[136]
Double heterojunction	Core-shell structured Fe_3O_4@SiO_2@CdS 0.2 g/L	1000-W tungsten-halide lamp (Philips) (λ > 420 nm)	Tetracycline 100 mg/L	Approximately 80% optimum within 21 min	[137]
Double heterojunction	RGO-CdS/ZnS 0.5 g/L	300-W Xe lamp (λ > 420 nm)	Tetracycline 15 mg/L	Approximately 90% optimum in 60 min	[138]
Double heterojunction	TiO_2/Bi_2WO_6/carbon fibers 3 g/L	300-W Xe lamp (λ > 400 nm)	Tetracycline hydrochloride 10 mg/L	Approximately 95% optimum within 60 min	[139]
Z-scheme heterojunction	Z-scheme beta-Bi_2O_3@g-C_3N_4 core/shell nanocomposite 0.5 g/L	250-W Xe lamp (λ > 420 nm)	Tetracycline 10 mg/L	Approximately 80% optimum within 50 min	[140]
Z-scheme heterojunction	Z-scheme WO_3-g-C_3N_4 0.5 g/L	300-W Xe arc lamp (1.5 AM solar simulator)	Sulfamethoxazole 10 mg/L	Approximately 92% optimum within 4h	[141]
Z-scheme heterojunction	Z-scheme AgI nanoparticle-sensitized Bi_5O_7I microspheres 0.5 g/L	300-W Xe lamp (λ > 400 nm)	TC (20 mg/L), DTC (10 mg/L), OTC (10 mg/L), or CIP (10 mg/L)	Approximately TC: 95%, DTC: 90%, OTC: 80% and CIP: 90% optimums within 40 min	[142]
Z-scheme heterojunction	Z-scheme CdTe/TiO_2 0.8 g/L	400-W halogen lamp (λ > 400 nm)	Tetracycline hydrochloride 20 mg/L	Approximately 78% optimum within 30 min	[143]
Z-scheme heterojunction	Type II AgI/$CuBi_2O_4$ Z-scheme AgBr/$CuBi_2O_4$ 0.5 g/L	300-W Xe lamp (λ > 420 nm)	Tetracycline 10 mg/L	Approximately Type II catalyst: 80% and Z-scheme catalyst: 90% optimums within 30 min	[144]
Z-scheme heterojunction	Z-scheme mesoporous Sn_3O_4 nanoclusters/g-C_3N_4 nanosheets 0.5 g/L	500-W Xe lamp (λ > 420 nm)	Tetracycline hydrochloride 10 mg/L	Approximately 72% optimum within 120 min	[145]

(*continued on next page*)

Table 2 (*continued*)

Strategies	Catalysts and concentration	Light source	Antibiotic and concentration	Degradation efficiency	Ref.
Z-scheme heterojunction	Z-scheme Bi_3TaO_7 QDs/g-C_3N_4 nanosheets (NSs) 0.5 g/L	LED lamp (λ = 420 nm, 86 W)	CIP and CPX 10 mg/L	Approximately CIP: 91%, CPX: 77% CPX within 120 min	[146]
Z-scheme heterojunction	Z-scheme WO_3 nanosheet/$K^+Ca_2Nb_3O_{10}^-$ ultrathin nanosheet 1 g/L	250-W xenon lamp as simulated sunlight (no filters).	Tetracycline hydrochloride 35 mg/L	Approximately 86% optimum within 120 min	[147]
Z-scheme heterojunction	Z-scheme AgI/BiOBr 0.5 g/L	300-W Xe lamp (λ > 420 nm)	Ciprofloxacin 10 mg/L	Approximately 91% optimum within 1h	[148]
Z-scheme heterojunction	Z-scheme Ag_3PO_4/g-C_3N_4 0.05 g/L	300-W Xe lamp (λ > 400 nm)	Sulfamethoxazole 1 mg/L	Approximately 99% optimum within 90 min	[149]
Z-scheme heterojunction	Z-scheme CdS-Au-$BiVO_4$ (010) 0.5 g/L	300-W Xe lamp (λ > 420 nm)	Tetracycline 10 mg/L	91% optimum within 90 min	[150]
Z-scheme heterojunction	Z-scheme $BiVO_4$/Ag/Cu_2O 0.4 g/L	300-W Xe lamp (λ > 420 nm)	Tetracycline 20 mg/L	Approximately 91% optimum within 90 min	[151]
Z-scheme heterojunction	Z-scheme $ZnFe_2O_4$/Ag/PEDOT 0.2 g/L	250-W xenon lamp (1.8 × 105 lx)	Tetracycline 20 mg/L	Approximately 72% optimum within 120 min	[152]
Z-scheme heterojunction	Organic-inorganic Z-scheme PANI/Ag/Ag_2MoO_4 ~ 0.2 g/L	40-W UV tube (Phillips)	Ciprofloxacin 3 mg/L	Approximately 100% optimum within 40 min	[153]
Z-scheme heterojunction	Z-scheme (001) BiOCl-Au-CdS 1 g/L	300-W Xe lamp (AM 1.5)	Sulfadiazine 20 mg/L	Approximately 91% optimum within 4h	[154]
Z-scheme heterojunction	Z-scheme iodine vacancy-rich BiOI/Ag@AgI 0.3 g/L	300-W Xe lamp (λ > 420 nm)	Tetracycline 20 mg/L	Approximately 86% optimum within 60 min	[155]
Z-scheme heterojunction	Z-scheme Ag_2CO_3/Ag/WO_3 0.5 g/L	300-W Xe lamp (λ > 420 nm)	CIP and TC 10 mg/L	Approximately CIP: 84% and TC: 81% optimums within 90 min	[156]
Z-scheme heterojunction	Z-scheme AgI/Ag/Bi_3TaO_7 0.5 g/L	300-W Xe lamp (visible light)	Sulfamethoxazole 5 mg/L	Approximately 98% optimum within 100 min	[157]
Z-scheme heterojunction	Z-scheme MIL-53(Fe)/Ag/g-C_3N_4 80 mg/L	Visible light	Clioquinol 10 mg/L	95% optimum within 100 min	[158]
Z-scheme heterojunction	Z-scheme $CeVO_4$/3D RGO aerogel/$BiVO_4$ 0.5 g/L	500-W Xe lamp	Tetracycline 20 mg/L	Approximately 100% optimum within 60 min	[159]
Z-scheme heterojunction	TCPP/rGO/Bi_2WO_6 0.3 g/L	300-W Xe lamp (λ > 420 nm)	Tetracycline 15 mg/L	Approximately 84% optimum within 60 min	[160]
Z-scheme heterojunction	Z-scheme Ag_3PO_4/Bi_2S_3/Bi_2O_3 1 g/L	300-W Xe lamp (λ > 420 nm)	Sulfamethazine (SAZ) and cloxacillin (CLX) 10 mg/L	Approximately SAZ: 99% and CLX: 90% optimums within 90 min	[161]
Z-scheme heterojunction	RGO-Ag_2O/TiO_2 0.4 g/L	350-W Hg lamp (λless than356 nm), 300-W Xe arc lamp (visible light), 300-W infrared lamp, and 156-W APOLLO solar simulator	Tetracycline 10 mg/L	100% and approximately 100% optimums within 60 min, approximately 90% optimums within 120 min	[162]
Z-scheme heterojunction	Z-scheme g-C_3N_4/Ag_2CO_3/graphene oxide 0.8 g/L	300-W Xe lamp (λ > 420 nm)	Tetracycline 20 mg/L	Approximately 82% optimum within 60 min	[163]
Z-scheme heterojunction	Z-scheme nitrogen-doped graphene QDs-$BiVO_4$/g-C_3N_4 0.5 g/L	250-W Xe lamp (λ > 420 nm)	Tetracycline 10 mg/L	Approximately 91% optimum within 30 min	[164]
Z-scheme heterojunction	Z-scheme graphitic carbon nitride (CN) and reduced graphene oxide (rGO) with AP 1 g/L	Both intense sunlight and weak indoor light irradiation	Norfloxacin 10 mg/L	Approximately 100% optimum within 30 min and 85% optimum within 2h	[165]
Z-scheme heterojunction	Z-scheme WO_3/Fe_3O_4/g-C_3N_4 1 g/L	300-W Xe lamp (λ > 400 nm)	Tetracycline 20 mg/L	89% optimum within 120 min	[166]
Z-scheme heterojunction	Z-scheme nitrogen-doped hollow mesoporous carbon spheres (N-HMCs) modified g-C_3N_4/Bi_2O_3 1 g/L	300-W Xe lamp (λ > 420 nm)	Tetracycline hydrochloride (TCH) and ciprofloxacin hydrochloride (CFH) 10 mg/L	Approximately 90% and 80% optimum within 60 min	[167]
Exposing active facets	$Bi_2O_2(OH)(NO_3)$ nanosheets with (001) active exposing facets 1 g/L	UV light irradiation (300-W Hg lamp)	Tetracycline hydrochloride 10 mg/L	Approximately 98% optimum within 25 min	[168]
Exposing active facets	Ultrathin $Bi_2O_2(OH)_xCl_{2-x}$ solid solution with exposed (001) facets 0.5 g/L	Visible light (420-nm LED)	Ciprofloxacin 20 mg/L	Approximately 90% optimum within 150 min	[169]
Exposing active facets	Nanosheet $BiVO_4$ with oxygen vacancies and exposed (001) facets 1 g/L	500-W Xe lamp without optical filters to simulate the sunlight	Oxytetracycline 20 mg/L	Approximately 96% optimum within 2h	[170]
Exposing active facets	Various well-defined Bi_2WO_6 crystals ~ 0.67 g/L	300-W Xe lamp (λ > 420 nm)	Ciprofloxacin 10 mg/L	Approximately 70% optimum within 5h	[171]
Exposing active facets	Doped BiOCl nanoplates ~ 0.67 g/L	300-W Xe lamp (λ > 420 nm)	Tetracycline hydrochloride 30 mg/L	Approximately 90% optimum within 100 min	[172]
Exposing active facets	(001) Ag@NC-TiO_2 square nanosheets 1 g/L	350-W Xe arc lamp (λ > 420 nm)	Ciprofloxacin 10 mg/L	Approximately 97% optimum within 150 min	[173]
Exposing active facets	TiO_2@g-C_3N_4 core–shell quantum 1 g/L	Xe lamp irradiation.	Tetracycline 20 mg/L	Approximately 100% optimum within less than 10 min	[174]

(*continued on next page*)

Table 2 (*continued*)

Strategies	Catalysts and concentration	Light source	Antibiotic and concentration	Degradation efficiency	Ref.
Porous materials	Intercalate structure g-C_3N_4@ATP 1 g/L	300-W Xe lamp (λ > 420 nm)	Tetracycline 20 mg/L	Approximately 90% optimum within 2h	[175]
Porous materials	3D hierarchical mesoporous BiOI Optimum 1.5 or 0.68 g/L	1000-W tungsten halogen lamp (λ > 420 nm)	Tetracycline hydrochloride Optimum 2.1 or 2 mg/L	Approximately 100% optimum within 37.5 or 101.5 min	[176]
Porous materials	BiOI hollow microspheres 1 g/L	300-W Xe lamp (λ > 400 nm)	Tetracycline 20 mg/L	80% optimum within 120 min	[177]
Porous materials	Ultra-thin Bi_2MoO_6 nanosheets 0.5 g/L-1.5 g/L	Sunlight	Ofloxacin 10 mg/L	Approximately 71% optimum within 90 min	[178]
Tailoring morphology	Rod-like SrV_2O_6 2–9 g/L	500-W tungsten lamp (λ > 400 nm)	Metronidazole 20 mg/L	98% optimum within 60 min	[179]
Tailoring morphology	TiO_2 nanobelts	Simulative solar light	Amikacin 5 mg/L	Approximately 70% optimum within 150 min	[180]
Tailoring morphology	ZnO Nanotubes 0.035 g/L	300-W Xe lamp (AM1.5 filter (1000 Wm^{-2}))	Ciprofloxacin 6.6 mg/L	Approximately 12% optimum within 2h	[181]
Tailoring morphology	$Bi_5FeTi_3O_{15}$ 0.4 g/L	300-W Xe lamp (λ > 420 nm)	Tetracycline hydrochloride 4.8 mg/L	Approximately 99% optimum within 1h	[182]
Tailoring morphology	Navel-like Bi_2WO_6 hierarchical microspheres	UV light irradiation (λ = 365 nm)	Norfloxacin (Concentration not provided)	Approximately 67% optimum within 8h	[183]
Tailoring morphology	spearhead-like g-C_3N_4 1 g/L	Xe lamp (35 W, 6000 K)	Tetracycline 20 mg/L	Approximately 70% optimum within 180 min	[184]
3D aerogel	g-C_3N_4@CA/B-PET 5 g/L	Artificial solar light (125 mW/cm^2)	Sulfaquinoxaline sodium 10 mg/L	Approximately 100% optimum within 60 min	[185]
3D aerogel	$BiVO_4$/3D RGO aerogel/$CeVO_4$ 0.5 g/L	500-W Xe lamp (visible light)	Tetracycline 20 mg/L	Approximately 90% optimum within 120 min	[159]
3D aerogel	3D MoS_2 nanosheets/graphene aerogel 0.8 mg/L	300-W Xe lamp (λ > 420 nm)	Tetracycline hydrochloride 60 mg/L	Approximately 10% optimum within 75 min	[186]

photoinduced electrons and holes at the interface. Therefore, in-depth studies have been conducted to design photocatalyst junction interfaces to monitor carrier migration capabilities. According to their phase composition, junction interfaces can be divided into homogenous junction interfaces and heterojunction interfaces.

3.2.1. Homogenous junction interfaces

Homogenous junction interfaces are built by identical compounds in the absence of additional components and have been the focus of significant interest. The construction of homogenous junction interfaces is primarily based on the established phase junction or facet junction, creating an effective migration pathway for the photoinduced charges.

3.2.2. Phase junction

Most crystals (e.g., TiO_2 [262–270], CdS [271], Bi_2O_3 [272], MoS_2 [273] and $ZnIn_2S_4$ [274]) have many different natural or artificial phases. The construction of the phase junction is a significant approach to improve the photocatalytic performance through accelerating the migration of electrons and holes. Many studies have been conducted on the design of photocatalyst phase junctions to boost carrier migration characteristics and capabilities [275,276]. Jia *et al.* [277] studied the theoretical basis of the phase changes and interfacial characteristics of Cu_2ZnSnS_4 with a hetero-phase junction. A type-II band structure could be formed at the hetero-phase junction of (101), (110), and (100) facets, thereby facilitating the photoelectric capacity. However, type-I heterojunctions may be aligned at the phase junction of (112) and (001) facets, hindering the generation of charges and improving optoelectronic properties owing to a high potential barrier. Similarly, according to the band engineering design theory, a bonding-region-width-controlled phase junction surrounded by cubic CdS and a hexagonal counterpart was designed by Ai *et al.* [271]. The electron–hole separation was optimized at an appropriate bonding region width (0.76 nm), which exhibited the highest photocatalytic efficiency (45% quantum efficiency) among all the examined samples, in addition to good photocorrosion resistance.

Artificial phases caused by vacancies or self-doping have been used to construct a phase junction to control the separation of electrons and holes. Recently, Cao *et al.* [201] constructed a g-C_3N_4 p-n homojunction through introducing nitrogen vacancies (NVs). The differences in Mott-Schottky plots between bulk g-C_3N_4 (CN) and PN-2 indicated that the

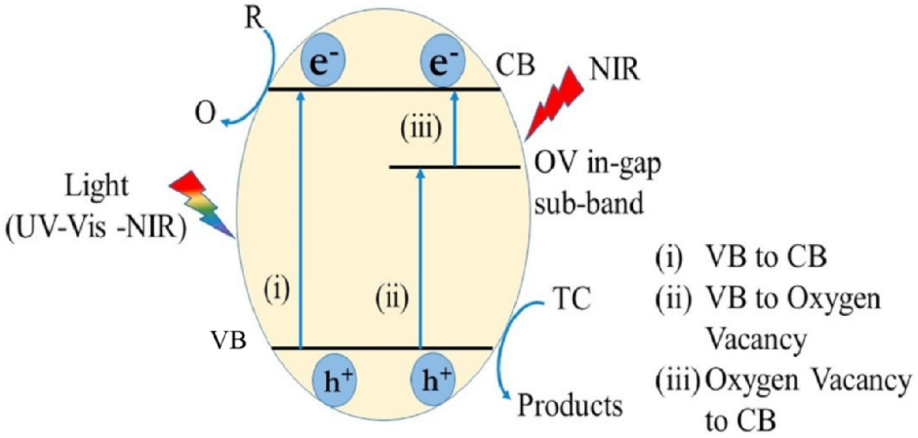

Fig. 3. Schematic of the OV-induced photocatalytic process on $ZnWO_{4-x}$ [54]

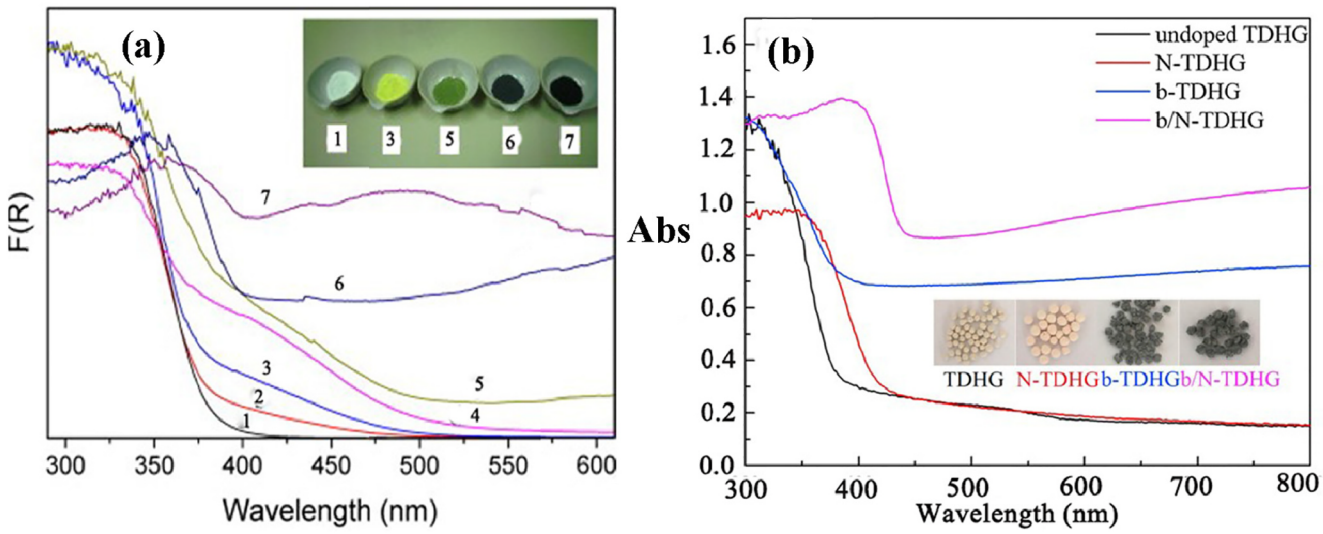

Fig. 4. (a) UV–vis diffuse reflectance spectra of a) 1) raw TiO_2 (500), and N-TiO_2 (T) samples prepared at 2) 450, 3) 500, 4) 550, 5) 600, 6) 700 and 7) 800 °C [247], (b) diffuse reflection spectra (DRS) curves of undoped and doped TDHG [63], Inset: Photographs of TDHG, N-TDHG, b -TDHG and b/N-TDHG photocatalysts.

conductivity characteristics of the homojunction were consistent with a p-n model (Fig. 6 (a) and (b)). Additionally, the PN-2 homojunction exhibited a distinct improvement in its photocatalytic performance to treat Rhodamine B (RhB), compared to CN, which was attributed to the efficient separation of the photoexcited charges at the PN-2 homojunction (Fig. 6 (c) and (d)). Chade Lv *et al.* [278] synthesized Bi^{5+}-BVO (Bi^{5+}-self-doped $Bi_4V_2O_{11}$) nanotubes and formed p-n homojunctions by implementing the oxygen vacancy strategy. Density functional theory (DFT) simulations and laboratory findings reveal that Bi^{5+} auto-doping reduces the bandgap of $Bi_4V_2O_{11}$ (BVO), thereby enhancing light capture. Furthermore, Bi^{5+} auto-doping confers both n- and p-type semiconductor characteristics to BVO, which enables the construction of p-n homojunctions to delay the quick annihilation of electrons and holes.

3.2.3. Facet engineering

Previous studies have reported that, unlike isolated surfaces, the coexistence of multiple crystal planes in single particles could be recognized as interactive surfaces with synergistic effects [279,280]. This means that redox reactions occur locally at the separate planes, resulting in spatial charge separation in semiconductors. For example, multi-morphologic silver bromide (AgBr) crystals containing distinct exposed planes were prepared by synchronously injecting silver nitrate and potassium bromide precursors [74]. The shape and exposed planes of the target sample could be easily modulated by varying the density of Br^- ions, which can significantly reduce the surface barrier of (100) and (111) planes and affect their growth rates. C-AgBr ((100) facet exposed cubes), T-AgBr ((100) and (111) facet exposed tetradecahedrons), and O-AgBr ((111) facet exposed octahedrons) could be obtained at specific Br^- concentrations of 10^0, $10^{0.5}$, and 10^1 mM. The obtained T-AgBr exhibited improved photocatalytic performance for the degradation of methyl orange (MO) and sulfadiazine (SD) owing to the formed facet heterojunction structures between the (111) and (100) facets. When irradiated with optical light, the electrons and holes are separately transported to the (100) and (111) facets. Therefore, electrons and holes could not merely be efficiently separated, but back-

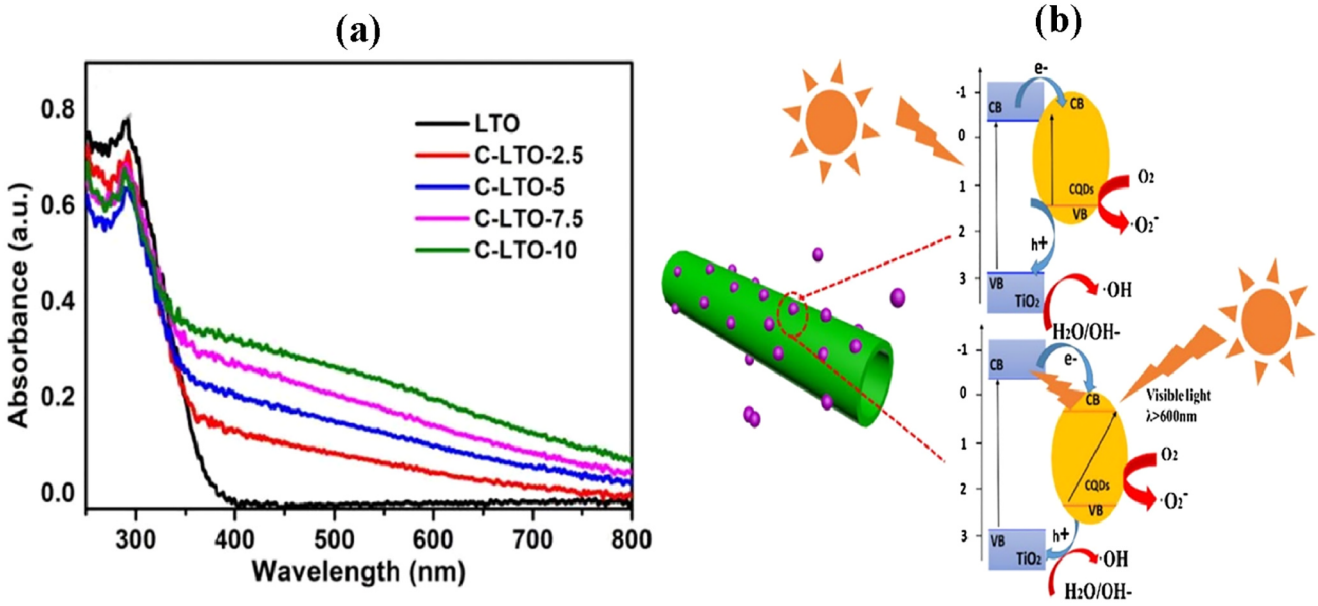

Fig. 5. (a) Light absorption curves [252] and (b) photocatalytic mechanisms of CQD/TNT photocatalyst [253]

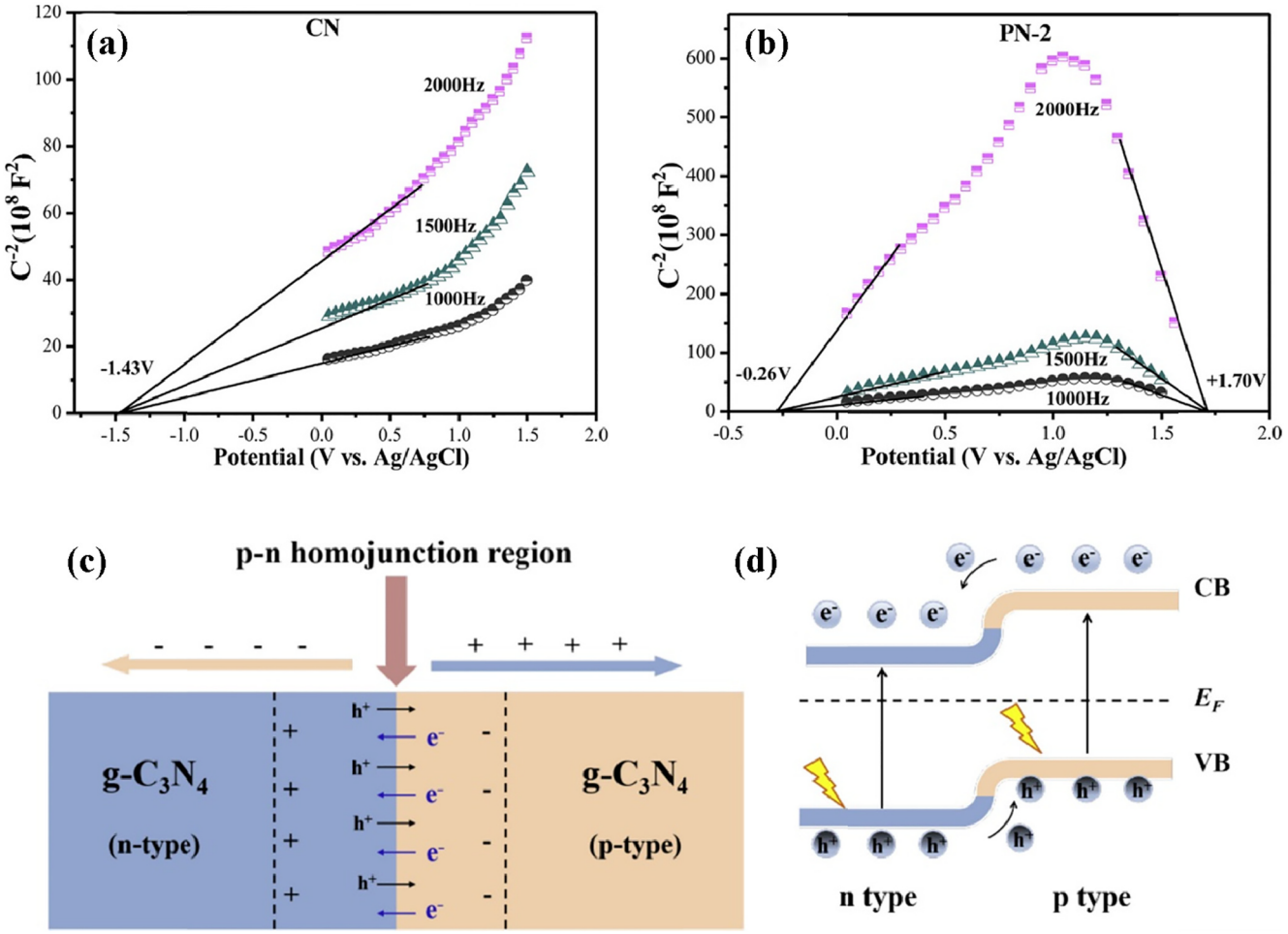

Fig. 6. Mott-Schottky curves on (a) CN and (b) PN-2; (c and d) schematic of carrier migration at the p-n homojunction [201]

reaction was effectively prevented owing to the isolation of active redox sites.

3.2.4. Heterojunction interfaces

The formation of homojunctions is considerably challenging owing to its complexity and high cost. Therefore, the creation of heterojunction interfaces has been proposed as an alternative to improve charge separation efficiency and has been widely investigated in the past decades [281]. Typically, heterojunctions are divided into five categories: (1) Schottky heterojunctions, (2) type I heterojunctions, (3) type II heterojunctions, (4) p-n heterojunctions, and (5) Z-scheme heterojunctions.

3.2.5. Schottky heterojunctions

At the semiconductor–metal interface, photoinduced electrons may typically flow from the former to the latter to match their Fermi energies and form a Schottky barrier. The formed Schottky junction can efficiently capture the electron, which promotes electron-hole separation. To further comprehend the mechanisms by which the Schottky junction improves photocatalysis, He *et al.* [282] prepared a series of Schottky-junction Ag-loaded carbon nitride fibers (Ag/CNFs) through loading $NaBH_4$-reduced Ag on preformed CNFs. The Schottky-type Ag/CNFs exhibited outstanding photodegradation performance for tetracycline (TC) under visible irradiation. The enhanced photodegradation activity resulted from the synergistic effect between surface plasmon resonance (SPR) on silver nanoparticles (Ag NPs) and the efficient isolation of the photoinduced carriers at the constructed Schottky heterojunction. Moreover, on account of the SPR absorption of specific metals, the light response could even be extended to the entire sunlight range. Therefore, in addition to promoting charge separation, semiconductors and plasmonic metals could also jointly improve light harvesting.

Jiang and co-workers synthesized a novel Ag/Bi_3O_4Cl photocatalyst with different amounts of Ag via a facile photo-deposition process [79]. The TC degradation on 1.0 wt% Ag/Bi_3O_4Cl was drastically more pronounced, compared to pristine Bi_3O_4Cl, and 94.2% TC could be degraded in 120 min (Fig. 7(a)). The improved photocatalytic properties resulted from the synergism of the photoinduced electrons on Bi_3O_4Cl and SPR from Ag NPs, which improved visible-light harvesting and facilitated the isolation of photoinduced electrons and holes (Fig. 7(b)).

In other studies, bimetallic-supported semiconductor catalysts (Pt/Au/TiO_2 [283,284], Au/Ag/TiO_2 [285], Pd-Cu/TiO_2 [286] and Ag-Cu/TiO_2 [287]) exhibited super activity and high selectivity, which cannot be found in single metals owing to the synergistic effect of bimetals. For example, Xue et al. [86] prepared plasmonic Au/Pt/g-C_3N_4 via a simple calcination-photo-deposition process. The prepared heterostructure photocatalyst exhibited an optimized photodegradation performance for antibiotic tetracycline hydrochloride (TC-HCl) treatment, and the visible-light-driven degradation was 3.4 times higher than that of pristine g-C_3N_4 (Fig. 7(c)). This enhanced photodegradation performance was attributed to the synergism between the SPR absorption on Au and the electron-trap effect of Pt NPs, which facilitated the light-harvesting capability and isolation of photoinduced charges on g-C_3N_4, thereby jointly boosting the photocatalytic properties. Similarly, TiO_2 nanotube arrays (Au-Pt/TNTAs) with small quantities of Au-Pt were

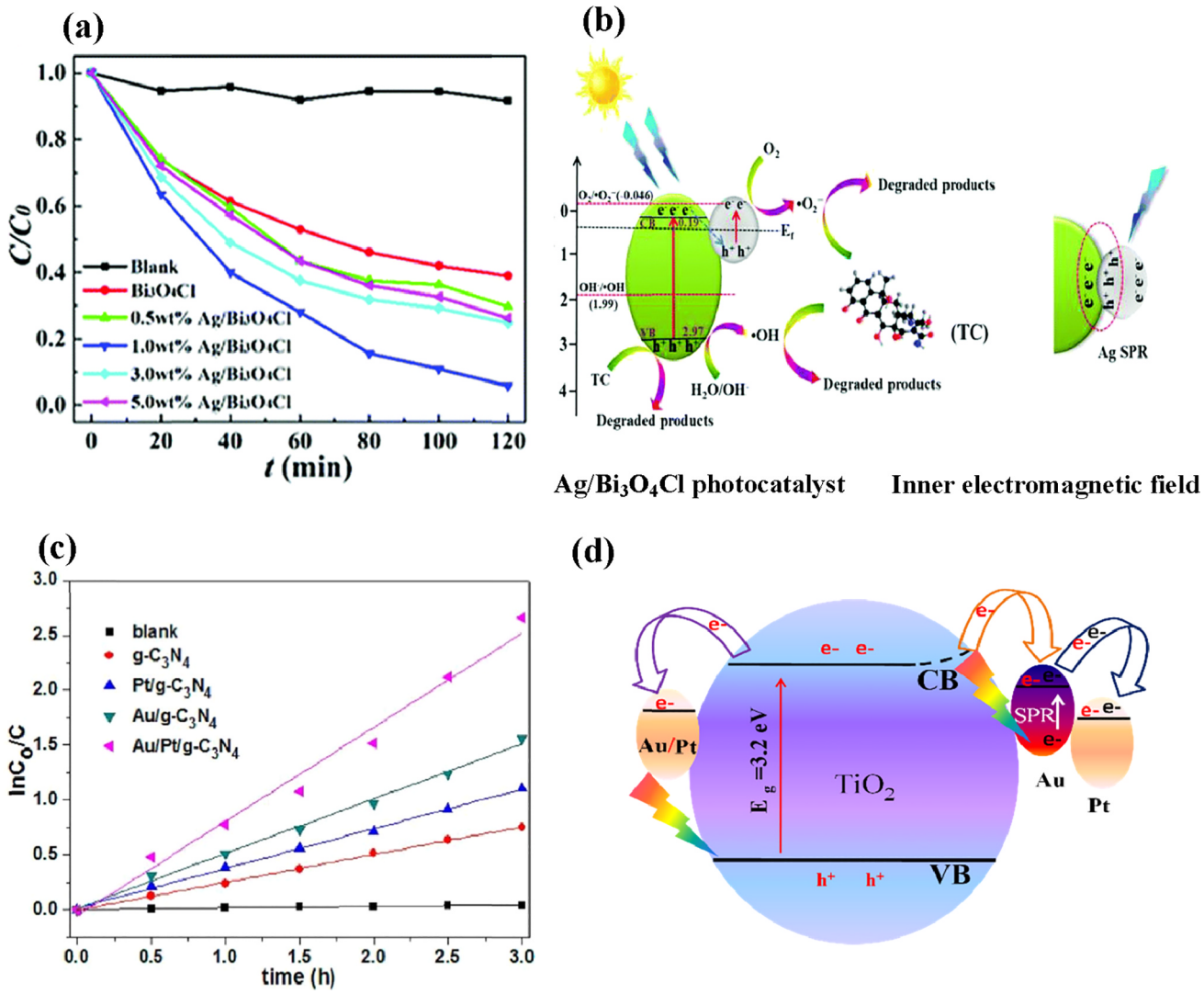

Fig. 7. (a) Photodegradation of TC by the as-synthesized plasmonic Ag/Bi_3O_4Cl under visible irradiation, (b) possible photocatalytic mechanisms on the Ag/Bi_3O_4Cl samples [79], (c) photocatalytic kinetics of prepared g-C_3N_4, Pt/g-C_3N_4, Au/g-C_3N_4, and Au/Pt/g-C_3N_4 nanocomposites [86] (d) schematic of the g-C_3N_4 photoinduced charge transport [284]

successfully prepared. Notably, these structures exhibited remarkably enhanced visible-light harvesting and carrier separation capacity. These enhancements in photodegradation activity derived from the synergism from interfacial Schottky junctions and the synergistic effect between ternary Au, Pt, and TNTAs (Fig. 7(d)) [284].

3.2.6. *Type I or II heterojunctions*

Compared to single semiconductors, the formation of type I semiconductor heterojunctions can promote photocatalytic efficiency. However, electrons and holes are enriched on the same semiconductor, which cannot effectively restrain the recombination of photoinduced electrons and holes. This makes type I semiconductor heterojunctions questionable prospects for photocatalytic property improvement [288,289]. To date, large numbers of traditional type II heterojunctions have been intensively investigated, some of which have rendered drastically optimized photocatalysis performances. For example, compared to pristine $MgFe_2O_4$, newly synthesized $MgFe_2O_4/MoS_2$ heterojunctions can accelerate electron–hole dissociation, albeit without extending the light-harvesting scope [90]. The as-synthesized $MgFe_2O_4/MoS_2$ sample delivered a prominent photoelectrochemical performance in TC treatment and H_2 evolution owing to its unique bandgap structure. In another study, a novel 2D-2D thin-layered g-C_3N_4/$Bi_4O_5Br_2$ type II heterojunction was synthesized by Ji's group [114] through a simple ionic-liquid-assisted solvothermal process (Fig. 8). This 2D g-C_3N_4 component had a layered microstructure, providing enough potential to successfully build intense interface interactions with exfoliated $Bi_4O_5Br_2$ nanosheets. Implementing the 2D layered g-C_3N_4 component provided several clear advantages, including an enlarged specific surface area (SBET), broadened optical light harvesting range, optimized electron–hole separation, and accelerated transport of the interfacial electrons and holes, all of which enhanced the photocatalytic performance of the $Bi_4O_5Br_2$ system within a given light range.

3.2.7. *p-n heterojunction*

Schottky and type II heterojunctions may successfully split electron–hole pairs. However, it is still necessary to restrain the superfast electron–hole annihilation at the interface. Therefore, p-n heterojunctions have been implemented and widely used to manage photocatalytic properties. For instance, Kang *et al.* [118] constructed a high-performance CoO/g-C_3N_4 p-n junction through a simple solvothermal process. The prepared p-n junction exhibited excellent visible-light-induced photocatalytic properties and consistency for TC treatment. These excellent photocatalytic properties were attributed to the production of an interfacial electric field around the junction, which

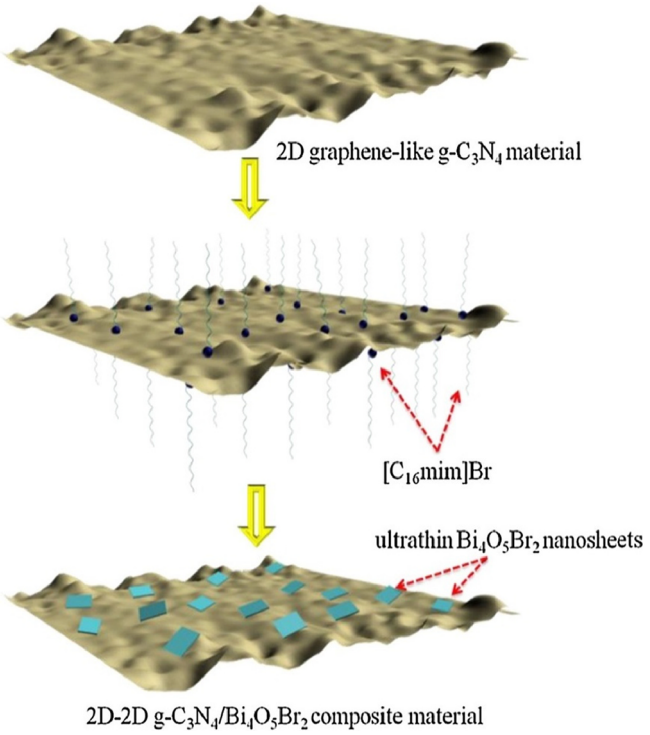

Fig. 8. Preparation process for g-C_3N_4/$Bi_4O_5Br_2$ nanocomposites [114]

effectively prevented the annihilation of photo-induced charges. Furthermore, a SnO_2/BiOI n-p heterojunction was successfully achieved by Wen *et al.* [124] by depositing SnO_2 NPs onto the outer surface of BiOI nanosheets. The obtained n-p heterojunction exhibited a strong visible-light-driven photocatalysis capacity and durability for the degradation of MO and oxytetracycline HCl. This excellent photocatalytic activity resulted from the constructed p-n heterojunction, which significantly limited the annihilation of electrons and holes.

Similarly, a novel three-dimensional (3D) layered BiOBr/Bi_2SiO_5 p-n heterostructure was successfully synthesized to efficiently degrade TC [123]. The prepared BiOBr/Bi_2SiO_5 p-n heterostructure exhibited an optimized visible-light-driven photocatalytic degradation of TC, which was 3.6-fold higher than that of BiOBr. Moreover, this high TC photodegradation performance remained constant for 5 cycles. This optimized photodegradation property of the BiOBr/Bi_2SiO_5 heterostructure was ascribed to the following factors: (1) the introduced BiOBr facilitated light harvesting within a broad optical range, and (2) the formed p-n heterojunction restrained the annihilation of photoinduced electrons and holes. These features prominently promoted the generation of ·OH, $\cdot O_2^-$, and H^+, leading to a promoted photocatalytic activity.

3.2.8. Z-scheme heterojunction

The development of Z-scheme photocatalysis was inspired by photosynthetic systems in nature and has attracted tremendous interests since the first report of a conventional Z-scheme photosystem in 1979 (Fig. 9(a)) [290,291]. Depending on the charge transport route involved, Z-scheme photosystems are classified as conventional, all-solid-state, and direct, which are distinguished by the specific transport medium used to facilitate the charge transport of reversible redox ion pairs, electronic conductors, and direct interfacial contacts, respectively [291–295]. For example, Ma et al. prepared a Z-scheme WO_3/$K^+Ca_2Nb_3O_{10}^-$ binary 2D-2D heterojunction photocatalyst from a facile hydrothermal co-assembly method at ambient conditions [147]. The as-prepared WO_3/$K^+Ca_2Nb_3O_{10}^-$ photocatalyst exhibited a remarkable improvement in the photodegradation of TC-HCl under simulated sunlight irradiation, compared to pristine WO_3 and $K^+Ca_2Nb_3O_{10}^-$. 20%-WO_3/$K^+Ca_2Nb_3O_{10}^-$ exhibited the maximum activity, which was 5.1 and 2 times higher than those of WO_3 and $K^+Ca_2Nb_3O_{10}^-$, respectively. These enhanced properties and sustainability were attributed to the tightly-coupled heterointerfaces, increased SBET area, optimized optical-capturing capability, and improved carrier dynamics of the semiconductor in the Z-scheme procedure.

Yang *et al.* [155] designed a new Z-scheme heterostructure Ag@AgI/VI-BOI (iodine-vacancy-rich BiOI), whereby Ag@AgI NPs were loaded locally on the outer surface of defect-rich BiOI nanosheets. This Z-scheme heterostructure possessed a remarkable visible-light-induced photocatalysis capacity for TC treatment, which was significantly higher than those of pristine BiOI, VI-BOI, and Ag@AgI. The enhanced photocatalytic properties of this Z-scheme heterostructure originated from the synergistic action between VI (iodine vacancies), interface junctions between AgI and VI-BOI, and Ag^0. A direct visible-light-induced solid-state C_3N_4 NS/TNTAs (g-C_3N_4 nanosheet/TiO_2 nanotube array) Z-scheme heterostructure (Fig. 9(b)) was successfully fabricated in-situ by adding preformed g-C_3N_4 nanosheets into the anodizing bath solution [296]. Enhanced photocatalytic performances and good stability were observed on nanosheet-supplemented photocatalysts, and g-C_3N_4(60)/TNTAs exhibited an optimum activity for the degradation of rhodamine B (RhB) and colorless TC-HCl. The optimized photodegradation performance was derived from an enhanced light harvesting capacity, a suppressed carrier recombination, and an extended carrier lifetime.

3.2.9. Double heterojunction

In addition to heterojunctions, double heterojunctions such as QDs Schottky heterojunctions combined with type II, Z-scheme heterojunction [127,130–132], type I combined with Z-scheme heterojunctions, and double Z-scheme heterojunctions have been applied to treat antibiotics (e.g., tetracycline hydrochloride, ciprofloxacin, oxytetracycline, ciprofloxacin, etc.) in water [135]. Tang *et al.* [297] prepared ternary Ag/$CuNb_2O_6$/$CuFe_2O_4$ heterostructures. The prepared multicomponent heterostructures exhibited stronger visible-light-induced photodegradation properties towards methylene blue (MB) and the pesticide imidacloprid than their single ($CuNb_2O_6$) and binary (Ag/$CuNb_2O_6$ or $CuNb_2O_6$/$CuFe_2O_4$) counterparts. The excellent photodegradation performance of the obtained ternary heterostructure was attributed to an enhanced visible-light harvesting capacity and rapid charge recombination restraint.

Jo *et al.* [130] developed a novel ternary 2D/2D/2D-configured LDH/CN/RGO heterostructure (CoAl-layered double hydroxide/g-C_3N_4/reduced graphene oxide) from a simple one-step hydrothermal synthesis. The prepared LDH/CN/RGO heterostructure exhibited a significantly superior visible-light-induced photodegradation activity for the treatment of Congo red (CR) and TC in water. Particularly, the LDH/CN/RGO heterostructure containing RGO (1 wt%) and LDH (15 wt%) featured optimum photodegradation properties in all the synthesized photocatalysts. The significantly enhanced photodegradation efficiency and outstanding consistency of the heterostructure LDH/CN/RGO were primarily attributed to the intense interface interaction between the CN, LDH, and RGO components (Fig. 10). This strong interfacial effect was further facilitated by the specifically arranged 2D/2D/2D microstructure, which ultimately accelerated the charge transport at the interface and efficiently separated photoinduced electrons and holes.

3.3. Strategies to manage surface reactions

Although charges can be effectively separated, recombination in the process of electron transport remains problematic when the charges cannot be consumed promptly due to low activity or limited active sites on the semiconductor surface. Therefore, strategies have been proposed to promote intrinsic active sites on photocatalysts and the adsorption of pollutants.

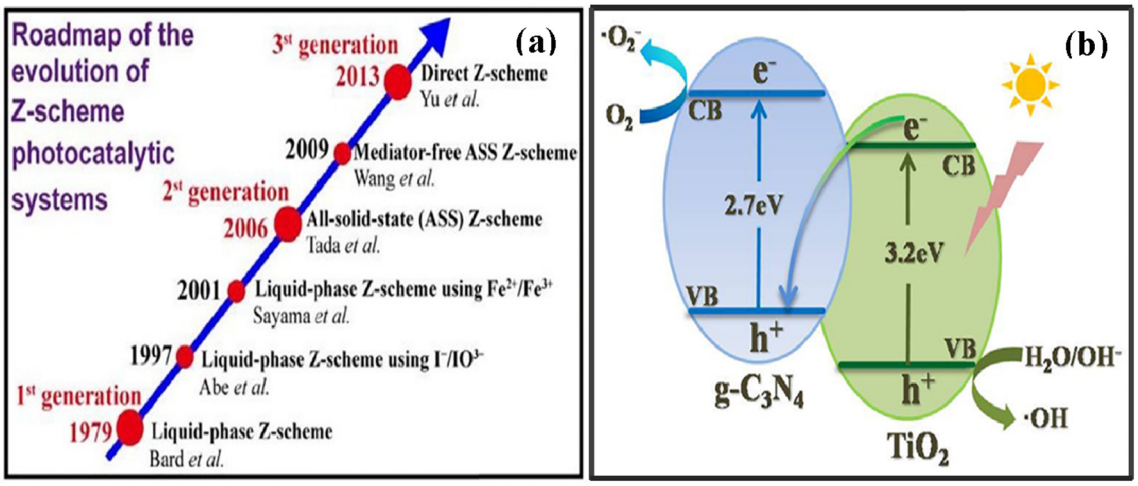

Fig. 9. (a) Roadmap of Z-scheme photocatalytic system evolution [293]; (b) suggested photoinduced charge transport on g-C_3N_4(60)/TNTAs [296]

3.3.1. Selective exposure of high energy facets

Typically, the redox reactions that occur on the outer surface or interface of semiconductors are highly susceptible to the exposed facets. Based on crystal anisotropy data, it is widely known that different crystal facets have different atomic arrangements, which result in different physical and chemical properties, including anisotropic surface electronic structures, tunable surface energy, and diverse molecule absorption abilities and reactivities [279].

Hao *et al.* [168] synthesized $Bi_2O_2(OH)(NO_3)$ nanosheets (BON-NS) with a predominant exposure of the reactive (0 0 1) plane through a wet-chemical process using sodium dodecylbenzene sulfonate (SDBS) as a template. They found that the BON-NS samples consisted of loosely stacked nanosheets, which provided an exceptionally high specific surface area, as well as more efficient charge separation. This feature was likely derived from the dominant exposure of reactive (0 0 1) facet and the $[Bi_2O_2(OH)]^+$ stacking layers down the *c* axis, which induces the orientation of an auto-built electric field. This allows the developed BON-NS to have an elevated capability for carrier separation and migration, leading to significantly superior UV-light photocatalysis performance for the treatment of antibiotics (tetracycline hydrochloride) than their bulk counterparts [168]. Additionally, hexagonal WO_3 (h-WO_3) was synthesized by employing sodium sulfate and ammonium sulfate as end-capping reagents through diverse hydrothermal methods [298]. Particularly, h-WO_3 NSs with exposed (0 0 2) planes exhibited the highest visible-light photodegradation performance owing to their large BET surface and interior electron–hole separation on high-energy (0 0 2) reactive planes.

3.3.2. Preparation of 2D porous materials

Porous materials have numerous notable advantages, including a high-density active core that facilitates photocatalytic reactions, high light absorption rates derived from the reflection and scattering of incident light within the pores, and high specific surface areas that improve the adsorption of contaminants and accelerate surface reactions.

Two-dimensional (2D) materials, including black phosphorus (BP), transition metal dichalcogenides (TMDs), metal oxides, metal carbides, metal nitrides, hexagonal boron nitride (h-BN), g-C_3N_4, and layered double hydroxides (LDH), have attracted substantial interest in the field of photocatalysis [299–301]. When performing as photocatalysts, the high BET surface and abundant surface reactive sites of 2D candidates may result in enhanced catalytic activity. To further improve photocatalytic properties, 2D porous materials with a more accessible BET surface and additional reactive sites are developed to completely expose the active sites to the contaminants and participate in the oxidation–reduction process, which degrades the contaminants and produces H_2/O_2.[302] Unfortunately, 2D porous materials, such as $MoSe_2$

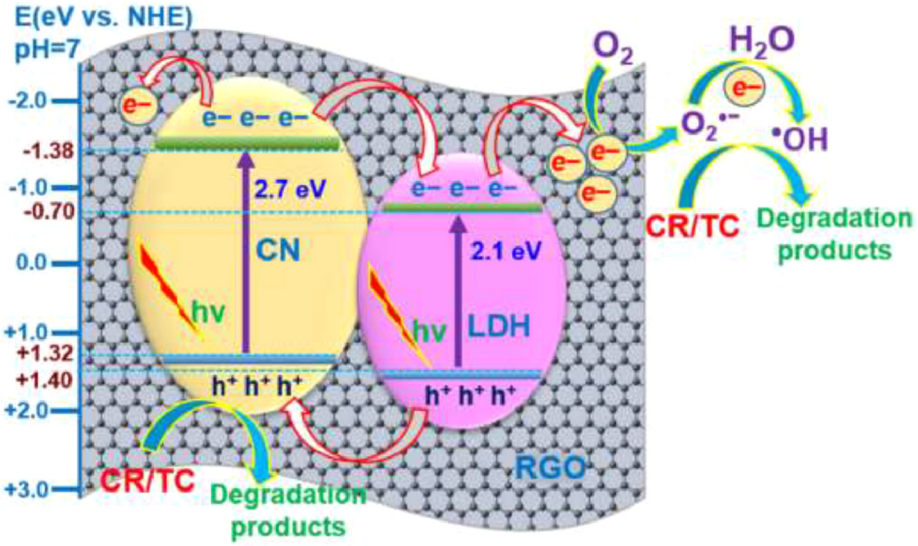

Fig. 10. Photocatalytic degradation mechanisms of CR and TC by a ternary LDH/CN/RGO heterostructure [130]

[303,304], MoS_2 [305–307], and g-C_3N_4 [308–322] are mostly used in photocatalytic hydrogen evolution or photodegradation of organic dyes and are rarely applied for the degradation of antibiotics. Nonetheless, 2D porous materials could be promising candidates for the photocatalytic treatment of antibiotics.

Kang *et al.* [311] prepared few-layer g-C_3N_4 NSs with foamy pores by ultrafast liquid-N_2-frozen exfoliation of its bulk counterpart within 10 s. The foamed porous super-thin g-C_3N_4 NSs exhibited interesting advances such as well-crystallized characteristics, a narrowed energy band, an additional unveiled edge, a slightly-augmented BET surface (135.6 m^2/g) with an increased mesopore, and an enhanced charge transport capability. Unlike massive g-C_3N_4, the super-thin porous g-C_3N_4 exhibited a remarkably promoted capability to generate reactive oxygen species (ROS) and a 4-fold improvement in performance for visible-light-excited RhB decomposition. This primarily resulted from an increase in reactive sites and a shortened route for charge transport. These results suggest that this technology could be further developed to generate high-performance super-thin g-C_3N_4 NSs for contaminant treatment.

Template-free 2D porous super-thin g-C_3N_4 NSs with doped oxygen atoms were synthesized by She *et al.* [316]. The photodegradation performance (60.8%) of MO and the mean H_2 production speed (~189.3 $\mu mol \cdot h^{-1}$) were nearly 71 and 5.2 times higher than those in the bulk phase, respectively. This enhanced photocatalysis derived from unique features such as an enriched adsorbable/reactive site, a reinforced oxidation–reduction capability and enhanced charge migration.

3.3.3. Preparing 3D aerogel materials

Aerogel photocatalysts with 3D continuous network structures can provide ultra-large accessible surface areas, rich porosities, and a large number of photocatalytic active sites, which can result in high absorption capacity and enhanced photocatalytic performance. Moreover, 3D aerogel materials can solve the problem of dispersion and recovery of photocatalytic materials in practical applications [186]. Liu *et al.* [159] recently fabricated ternary $CeVO_4$/3D RGO (reduced graphene oxide) aerogel/$BiVO_4$ photocatalysts (Fig. 11) and used them for visible-light-induced O_2 generation and TC removal. The synthesized aerogel composites displayed a well-defined 3D hierarchical microstructure built by the two vanadates and RGO. The optimum heterostructure exhibited a significantly facilitated visible-light-excited H_2O oxidation capacity as well as TC degradation. This optimized photocatalysis capacity resulted from the large BET surface and ternary Z-scheme heterojunction of the aerogel. These features enabled the 3D RGO aerogel to connect to the other semiconductors and act as distinct dual pathways to further enhance the charge transport.

A freestanding MoS_2 nanosheets/graphene aerogel (3D MoS_2 NS/GA) heterostructure was recently created through a simple hydrothermal process [186]. The obtained 3D MoS_2 NS/GA exhibited an excellent visible-light photodegradation efficiency for TC-HCl disposal with superior stability and reusability. Chen *et al.* [185] prepared powerful cellulose aerogel/blended polyester fibers (3D g-C_3N_4@CA/B-PET) via a simple process by supporting g-C_3N_4 NSs on B-PET reinforced cellulose aerogel (CA). The prepared g-C_3N_4@CA/B-PET photocatalyst exhibited a superior photocatalytic performance to treat sulfaquinoxaline sodium and Cr (VI), compared to pristine g-C_3N_4. Moreover, heterostructure g-C_3N_4@CA/B-PET aerogel can be easily recycled and reused and is remarkably resistant to light and water currents.

4. Summary and outlook

The hazards of antibiotics and their treatment methods were briefly discussed herein, followed by a discussion on the current state of photocatalytic degradation of antibiotics in water. Photocatalysis plays an important role in treating antibiotic residues in water due to its superb features. However, efforts have to be made to further improve the efficiency for the wide application of this technology. The strategies for the improvement of degradation efficiency are the following:

(1) increasing light-harvesting capacity via defect engineering
(2) enhancing charge separation via interface engineering
(3) accelerating surface reaction.

These strategies are promising based on previous studies. However, for further practical applications, many challenges remain to be addressed:

a) It is difficult to identify the exact occurrence, formation, concentration, and types of defects (especially for vacancies) using current characterization techniques. This produces barriers for understanding the relationship between the structure and performance, which limits the further development of these technologies.
b) The construction of traditional heterojunctions via interface

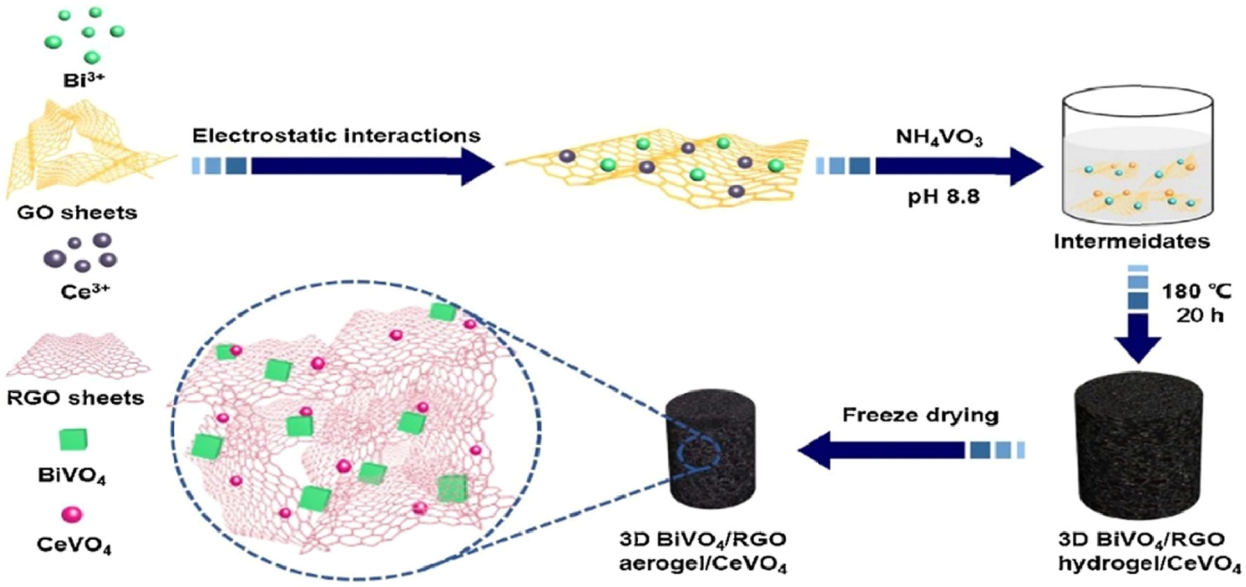

Fig. 11. Synthesis of $BiVO_4$/RGO/$CeVO_4$ heterostructures [159]

engineering has been intensively studied. Nonetheless, only a few previous studies have focused on homojunctions and double heterojunctions, given that current preparation methods are complex, time-consuming, non-eco-friendly, and theoretically lacking.

c) The BET surface and the number of active sites of a catalyst are key factors for accelerating surface reactions. In addition to increasing the specific surface area by controlling catalyst morphology, the selective exposure of highly active high-specific-surface-area crystal faces has recently become a popular research topic. However, most of these materials are used for hydrogen production, with few instances of antibiotic treatment applications.

Despite these challenges, this review provides valuable information on improvement and modification strategies for the design of high-performance photocatalysts to treat antibiotic residues in water. Besides, it is difficult to treat the antibiotic residues in practice by a sole technology. Innovating a complex system comprising photocatalysis and photoelectrocatalysis or electrocatalysis could be a promising alternative for the efficient removal of antibiotic residues in water. This review provides new insights into the design of high-efficiency photocatalysts for the degradation of antibiotic residues, thereby furthering the development of photocatalysis for water treatment and other fields.

Declaration of Competing Interest

The authors declare that they have no known competing financial interests or personal relationships that could have appeared to influence the work reported in this paper.

Acknowledgments

This work was supported by the Zhejiang Provincial Natural Science Foundation of China (No. LY17E020008), the Technology Foundation for Selected Overseas Chinese Scholars of Zhejiang Province, and Fundamental Research Funds for the Provincial Universities of Zhejiang (2020YW53). This work was also carried out with the support of the Cooperative Research Program for Agriculture Science and Technology Development (Project No. PJ014758), the Rural Development Administration in the Republic of Korea.

References

[1] K.-R. Kim, G. Owens, S.-I. Kwon, K.-H. So, D.-B. Lee, Y.S. Ok, Occurrence and environmental fate of veterinary antibiotics in the terrestrial environment, Water Air Soil Pollut. 214 (2011) 163–174, https://doi.org/10.1007/s11270-010-0412-2.

[2] S. Rodriguez-Mozaz, S. Chamorro, E. Marti, B. Huerta, M. Gros, A. Sanchez-Melsio, C.M. Borrego, D. Barcelo, J.L. Balcazar, Occurrence of antibiotics and antibiotic resistance genes in hospital and urban wastewaters and their impact on the receiving river, Water Res. 69 (2015) 234–242, https://doi.org/10.1016/j.watres.2014.11.021.

[3] J.F. Kerrigan, K.D. Sandberg, D.R. Engstrom, T.M. LaPara, W.A. Arnold, Small and large-scale distribution of four classes of antibiotics in sediment: association with metals and antibiotic resistance genes, Environ. Sci. Processes Impacts 20 (2018) 1167–1179, https://doi.org/10.1039/c8em00190a.

[4] Q.T. Dinh, E. Moreau-Guigon, P. Labadie, F. Alliot, M.J. Teil, M. Blanchard, M. Chevreuil, Occurrence of antibiotics in rural catchments, Chemosphere 168 (2017) 483–490, https://doi.org/10.1016/j.chemosphere.2016.10.106.

[5] K.G. Karthikeyan, M.T. Meyer, Occurrence of antibiotics in wastewater treatment facilities in Wisconsin, USA, Sci. Total Environ. 361 (2006) 196–207, https://doi.org/10.1016/j.scitotenv.2005.06.030.

[6] G. Siedlewicz, A. Bialk-Bielinska, M. Borecka, A. Winogradow, P. Stepnowski, K. Pazdro, Presence, concentrations and risk assessment of selected antibiotic residues in sediments and near-bottom waters collected from the Polish coastal zone in the southern Baltic Sea-Summary of 3 years of studies, Mar. Pollut. Bull. 129 (2018) 787–801, https://doi.org/10.1016/j.marpolbul.2017.10.075.

[7] D. Dong, L. Zhang, S. Liu, Z. Guo, X. Hua, Antibiotics in water and sediments from Liao River in Jilin Province, China: occurrence, distribution, and risk assessment, Environ. Earth Sci. 75 (2016) 1202, https://doi.org/10.1007/s12665-016-6008-4.

[8] Y.M. Awad, S.-C. Kim, S.A.M. Abd El-Azeem, K.-H. Kim, K.-R. Kim, K. Kim, C. Jeon, S.S. Lee, Y.S. Ok, Veterinary antibiotics contamination in water, sediment, and soil near a swine manure composting facility, Environ. Earth Sci. 71 (2013) 1433–1440, https://doi.org/10.1007/s12665-013-2548-z.

[9] A.U. Rajapaksha, M. Vithanage, J.E. Lim, M.B. Ahmed, M. Zhang, S.S. Lee, Y.S. Ok, Invasive plant-derived biochar inhibits sulfamethazine uptake by lettuce in soil, Chemosphere 111 (2014) 500–504, https://doi.org/10.1016/j.chemosphere.2014.04.040.

[10] M. Vithanage, A.U. Rajapaksha, X. Tang, S. Thiele-Bruhn, K.H. Kim, S.-E. Lee, Y.S. Ok, Sorption and transport of sulfamethazine in agricultural soils amended with invasive-plant-derived biochar, J. Environ. Manage. 141 (2014) 95–103, https://doi.org/10.1016/j.jenvman.2014.02.030.

[11] M.M. McConnell, L. Truelstrup Hansen, R.C. Jamieson, K.D. Neudorf, C.K. Yost, A. Tong, Removal of antibiotic resistance genes in two tertiary level municipal wastewater treatment plants, Sci. Total Environ. 643 (2018) 292–300, https://doi.org/10.1016/j.scitotenv.2018.06.212.

[12] M. Jimenez-Tototzintle, I.J. Ferreira, S. da Silva Duque, P.R. Guimaraes Barrocas, E.M. Saggioro, Removal of contaminants of emerging concern (CECs) and antibiotic resistant bacteria in urban wastewater using UVA/TiO_2/H_2O_2 photocatalysis, Chemosphere 210 (2018) 449–457, https://doi.org/10.1016/j.chemosphere.2018.07.036.

[13] A. Boukhelkhal, O. Benkortbi, M. Hamadache, Use of an anionic surfactant for the sorption of a binary mixture of antibiotics from aqueous solutions, Environ. Technol. 40 (2018) 3328–3336, https://doi.org/10.1080/09593330.2018.1472301.

[14] J. Luo, X. Li, C. Ge, K. Müller, H. Yu, P. Huang, J. Li, D.C.W. Tsang, N.S. Bolan, J. Rinklebe, H. Wang, Sorption of norfloxacin, sulfamerazine and oxytetracycline by KOH-modified biochar under single and ternary systems, Bioresour. Technol. 263 (2018) 385–392, https://doi.org/10.1016/j.biortech.2018.05.022.

[15] J. Wang, Q. Yao, C. Sheng, C. Jin, Q. Sun, One-Step Preparation of Graphene Oxide/Cellulose Nanofibril Hybrid Aerogel for Adsorptive Removal of Four Kinds of Antibiotics, Journal of Nanomaterials 2017 (2017) 1–10, https://doi.org/10.1155/2017/5150613.

[16] Q. Zhao, S. Zhang, X. Zhang, L. Lei, W. Ma, C. Ma, L. Song, J. Chen, B. Pan, B. Xing, Cation-Pi Interaction: A Key Force for Sorption of Fluoroquinolone Antibiotics on Pyrogenic Carbonaceous Materials, Environ. Sci. Technol. 51 (2017) 13659–13667, https://doi.org/10.1021/acs.est.7b02317.

[17] I.A. Lawal, B. Moodley, Sorption mechansim of pharmaceuticals from aqueous medium on ionic liquid modified biomass, J. Chem. Technol. Biotechnol. 92 (2017) 808–818, https://doi.org/10.1002/jctb.5063.

[18] C.H. Liu, Y.H. Chuang, H. Li, B.J. Teppen, S.A. Boyd, J.M. Gonzalez, C.T. Johnston, J. Lehmann, W. Zhang, Sorption of Lincomycin by Manure-Derived Biochars from Water, J. Environ. Qual. 45 (2016) 519–527, https://doi.org/10.2134/jeq2015.06.0320.

[19] G. Li, Y. Feng, W. Zhu, X. Zhang, Enhanced adsorptive performance of tetracycline antibiotics on lanthanum modified diatomite, Korean J. Chem. Eng. 32 (2015) 2109–2115, https://doi.org/10.1007/s11814-015-0058-2.

[20] V.M. Nurchi, M. Crespo-Alonso, M.I. Pilo, N. Spano, G. Sanna, R. Toniolo, Sorption of ofloxacin and chrysoidine by grape stalk. A representative case of biomass removal of emerging pollutants from wastewater, Arabian J. Chem. 12 (2019) 1141–1147, https://doi.org/10.1016/j.arabjc.2015.01.006.

[21] W.C. Li, M.H. Wong, A comparative study on tetracycline sorption by Pachydictyon coriaceum and Sargassum hemiphyllum, Int. J. Environ. Sci. Technol. 12 (2014) 2731–2740, https://doi.org/10.1007/s13762-014-0690-0.

[22] A. Zhou, Y. Zhang, R. Li, X. Su, L. Zhang, Adsorptive removal of sulfa antibiotics from water using spent mushroom substrate, an agricultural waste, Desalin. Water Treat. 57 (2016) 388, https://doi.org/10.1080/19443994.2014.979239.

[23] S. Jia, Z. Yang, K. Ren, Z. Tian, C. Dong, R. Ma, G. Yu, W. Yang, Removal of antibiotics from water in the coexistence of suspended particles and natural organic matters using amino-acid-modified-chitosan flocculants: A combined experimental and theoretical study, J. Hazard. Mater. 317 (2016) 593–601, https://doi.org/10.1016/j.jhazmat.2016.06.024.

[24] O.A. Alsager, M.N. Alnajrani, H.A. Abuelizz, I.A. Aldaghmani, Removal of antibiotics from water and waste milk by ozonation: kinetics, byproducts, and antimicrobial activity, Ecotoxicol. Environ. Saf. 158 (2018) 114–122, https://doi.org/10.1016/j.ecoenv.2018.04.024.

[25] Y. Ji, Z. Pan, D. Yuan, B. Lai, Advanced Treatment of the Antibiotic Production Wastewater by Ozone/Zero-Valent Iron Process, CLEAN - Soil, Air, Water 46 (2018) 1700666, https://doi.org/10.1002/clen.201700666.

[26] R. Kidak, S. Dogan, Medium-high frequency ultrasound and ozone based advanced oxidation for amoxicillin removal in water, Ultrason. Sonochem. 40 (2018) 131–139, https://doi.org/10.1016/j.ultsonch.2017.01.033.

[27] M. Feng, L. Yan, X. Zhang, P. Sun, S. Yang, L. Wang, Z. Wang, Fast removal of the antibiotic flumequine from aqueous solution by ozonation: Influencing factors, reaction pathways, and toxicity evaluation, Sci. Total Environ. 541 (2016) 167–175, https://doi.org/10.1016/j.scitotenv.2015.09.048.

[28] K.S. Tay, N. Madehi, Ozonation of ofloxacin in water: by-products, degradation pathway and ecotoxicity assessment, Sci. Total Environ. 520 (2015) 23–31, https://doi.org/10.1016/j.scitotenv.2015.03.033.

[29] R.B.P. Marcelino, M.M.D. Leao, R.M. Lago, C.C. Amorim, Multistage ozone and biological treatment system for real wastewater containing antibiotics, J. Environ. Manage. 195 (2017) 110–116, https://doi.org/10.1016/j.jenvman.2016.04.041.

[30] S.S.M. Hassan, H.I. Abdel-Shafy, M.S.M. Mansour, Removal of pharmaceutical compounds from urine via chemical coagulation by green synthesized ZnO-nanoparticles followed by microfiltration for safe reuse, Arabian J. Chem. 12 (2016) 4074–4083, https://doi.org/10.1016/j.arabjc.2016.04.009.

[31] B. Kamarehie, F. Ahmadi, F. Hafezi, A. Abbariki, R. Heydari, M.A. Karami, Experimental data of electric coagulation and photo-electro-phenton process efficiency in the removal of metronidazole antibiotic from aqueous solution, Data in

Brief 18 (2018) 96–101, https://doi.org/10.1016/j.dib.2018.03.003.
[32] P. Karaolia, I. Michael-Kordatou, E. Hapeshi, J. Alexander, T. Schwartz, D. Fatta-Kassinos, Investigation of the potential of a Membrane BioReactor followed by solar Fenton oxidation to remove antibiotic-related microcontaminants, Chem. Eng. J. 310 (2017) 491–502, https://doi.org/10.1016/j.cej.2016.04.113.
[33] V. Sharma, R. Vinoth Kumar, K. Pakshirajan, G. Pugazhenthi, Integrated adsorption-membrane filtration process for antibiotic removal from aqueous solution, Powder Technol. 321 (2017) 259–269, https://doi.org/10.1016/j.powtec.2017.08.040.
[34] J. Zheng, C. Su, J. Zhou, L. Xu, Y. Qian, H. Chen, Effects and mechanisms of ultraviolet, chlorination, and ozone disinfection on antibiotic resistance genes in secondary effluents of municipal wastewater treatment plants, Chem. Eng. J. 317 (2017) 309–316, https://doi.org/10.1016/j.cej.2017.02.076.
[35] M.R. Ramli, N.M. Sulaiman, M.A. Mohd, M.F. Rabuni, Performance of chlorination process during nanofiltration of sulfonamide antibiotic, Water Sci. Technol. 72 (2015) 1611–1620, https://doi.org/10.2166/wst.2015.367.
[36] B. Akyon, M. McLaughlin, F. Hernandez, J. Blotevogel, K. Bibby, Characterization and biological removal of organic compounds from hydraulic fracturing produced water, Environ. Sci. Processes Impacts 21 (2019) 279–290, https://doi.org/10.1039/c8em00354h.
[37] Z. Cetecioglu, M. Atasoy, Biodegradation and inhibitory effects of antibiotics on biological wastewater treatment systems, Toxicity and Biodegradation Testing (2018) 29–55.
[38] J. Zhang, H. Lin, J. Ma, W. Sun, Y. Yang, X. Zhang, Compost-bulking agents reduce the reservoir of antibiotics and antibiotic resistance genes in manures by modifying bacterial microbiota, Sci. Total Environ. 649 (2019) 396–404, https://doi.org/10.1016/j.scitotenv.2018.08.212.
[39] L.V. de Souza Santos, A.M. Meireles, L.C. Lange, Degradation of antibiotics norfloxacin by Fenton, UV and UV/H_2O_2, J. Environ. Manage. 154 (2015) 8–12, https://doi.org/10.1016/j.jenvman.2015.02.021.
[40] M.S. Yahya, N. Oturan, K. El Kacemi, M. El Karbane, C. Aravindakumar, M.A. Oturan, Oxidative degradation study on antimicrobial agent ciprofloxacin by electro-Fenton process: kinetics and oxidation products, Chemosphere 117 (2014) 447–454, https://doi.org/10.1016/j.chemosphere.2014.08.016.
[41] V. Homem, L. Santos, Degradation and removal methods of antibiotics from aqueous matrices-a review, J. Environ. Manage. 92 (2011) 2304–2347, https://doi.org/10.1016/j.jenvman.2011.05.023.
[42] S. Chang, X. Yang, Y. Sang, H. Liu, Highly Efficient Photocatalysts and Continuous-Flow Photocatalytic Reactors for Degradation of Organic Pollutants in Wastewater, Chem Asian J 11 (2016) 2352–2371, https://doi.org/10.1002/asia.201600363.
[43] U.I. Gaya, A.H. Abdullah, Heterogeneous photocatalytic degradation of organic contaminants over titanium dioxide: a review of fundamentals, progress and problems, J. Photochem. Photobiol., C 9 (2008).
[44] J.C. Colmenares, R. Luque, Heterogeneous photocatalytic nanomaterials: prospects and challenges in selective transformations of biomass-derived compounds, Chem Soc Rev 43 (2014) 765–778, https://doi.org/10.1039/c3cs60262a.
[45] E.S. Elmolla, M. Chaudhuri, Photocatalytic degradation of amoxicillin, ampicillin and cloxacillin antibiotics in aqueous solution using UV/TiO_2 and UV/H_2O_2/TiO_2 photocatalysis, Desalination 252 (2010) 46–52, https://doi.org/10.1016/j.desal.2009.11.003.
[46] A.C. Nogueira, L.E. Gomes, J.A.P. Ferencz, J.E.F.S. Rodrigues, R.V. Gonçalves, H. Wender, Improved Visible Light Photoactivity of $CuBi_2O_4$/CuO Heterojunctions for Photodegradation of Methylene Blue and Metronidazole, The Journal of Physical Chemistry C 123 (2019) 25680–25690, https://doi.org/10.1021/acs.jpcc.9b06907.
[47] Y. Zhao, Y. Wang, H. Shi, E. Liu, J. Fan, X. Hu, Enhanced photocatalytic activity of ZnSe QDs/g-C_3N_4 composite for Ceftriaxone sodium degradation under visible light, Mater. Lett. 231 (2018) 150–153, https://doi.org/10.1016/j.matlet.2018.08.034.
[48] R. Saravanan, F. Gracia, A. Stephen, Basic Principles, Mechanism, and Challenges of Photocatalysis, Nanocomposites for Visible Light-induced Photocatalysis (2017) 19–40.
[49] W. Tu, Y. Zhou, Z. Zou, Versatile Graphene-Promoting Photocatalytic Performance of Semiconductors: Basic Principles, Synthesis, Solar Energy Conversion, and Environmental Applications, Adv. Funct. Mater. 23 (2013) 4996–5008, https://doi.org/10.1002/adfm.201203547.
[50] H.L. Tan, F.F. Abdi, Y.H. Ng, Heterogeneous photocatalysts: an overview of classic and modern approaches for optical, electronic, and charge dynamics evaluation, Chem Soc Rev 48 (2019) 1255–1271, https://doi.org/10.1039/c8cs00882e.
[51] J. Sun, H. Xu, D. Li, Z. Zou, Q. Wu, G. Liu, J. Yang, L. Sun, D. Xia, Ultrasound-assisted synthesis of a feathery-shaped BiOCl with abundant oxygen vacancies and efficient visible-light photoactivity, New J. Chem. 42 (2018) 19571–19577, https://doi.org/10.1039/c8nj04165b.
[52] J. Zhang, Y. Gao, X. Jia, J. Wang, Z. Chen, Y. Xu, Oxygen vacancy-rich mesoporous ZrO_2 with remarkably enhanced visible-light photocatalytic performance, Sol. Energy Mater. Sol. Cells 182 (2018) 113–120, https://doi.org/10.1016/j.solmat.2018.03.023.
[53] J. Lyu, Z. Hu, Z. Li, M. Ge, Removal of tetracycline by BiOBr microspheres with oxygen vacancies: Combination of adsorption and photocatalysis, J. Phys. Chem. Solids 129 (2019) 61–70, https://doi.org/10.1016/j.jpcs.2018.12.041.
[54] M.I. Osotsi, D.K. Macharia, B. Zhu, Z. Wang, X. Shen, Z. Liu, L. Zhang, Z. Chen, Synthesis of $ZnWO_{4-x}$ nanorods with oxygen vacancy for efficient photocatalytic degradation of tetracycline, Progress in Natural Science: Materials International 28 (2018) 408–415, https://doi.org/10.1016/j.pnsc.2018.01.007.
[55] X. Xu, X. Ding, X. Yang, P. Wang, S. Li, Z. Lu, H. Chen, Oxygen vacancy boosted photocatalytic decomposition of ciprofloxacin over Bi_2MoO_6: Oxygen vacancy engineering, biotoxicity evaluation and mechanism study, J. Hazard. Mater. 364 (2019) 691–699, https://doi.org/10.1016/j.jhazmat.2018.10.063.
[56] S. Panneri, P. Ganguly, M. Mohan, B.N. Nair, A.A.P. Mohamed, K.G. Warrier, U. Hareesh, Photoregenerable, bifunctional granules of carbon-doped g-C_3N_4 as adsorptive photocatalyst for the efficient removal of tetracycline antibiotic, ACS Sustainable Chem. Eng. 5 (2017) 1610–1618, https://doi.org/10.1021/acssuschemeng.6b02383.
[57] J. Huang, D. Li, R. Li, Q. Zhang, T. Chen, H. Liu, Y. Liu, W. Lv, G. Liu, An efficient metal-free phosphorus and oxygen co-doped g-C_3N_4 photocatalyst with enhanced visible light photocatalytic activity for the degradation of fluoroquinolone antibiotics, Chem. Eng. J. 374 (2019) 242–253, https://doi.org/10.1016/j.cej.2019.05.175.
[58] L.K.B. Paragas, M.D.G. de Luna, R.A. Doong, Rapid removal of sulfamethoxazole from simulated water matrix by visible-light responsive iodine and potassium co-doped graphitic carbon nitride photocatalysts, Chemosphere 210 (2018) 1099–1107, https://doi.org/10.1016/j.chemosphere.2018.07.109.
[59] M. Wang, C. Jin, Z. Li, M. You, Y. Zhang, T. Zhu, The effects of bismuth (III) doping and ultrathin nanosheets construction on the photocatalytic performance of graphitic carbon nitride for antibiotic degradation, J. Colloid Interface Sci. 533 (2019) 513–525, https://doi.org/10.1016/j.jcis.2018.08.113.
[60] F. Cai, Y. Tang, F. Chen, Y. Yan, W. Shi, Enhanced visible-light-driven photocatalytic degradation of tetracycline by Cr^{3+} doping $SrTiO_3$ cubic nanoparticles, RSC Adv. 5 (2015) 21290–21296, https://doi.org/10.1039/C4RA13821J.
[61] P. Huo, Z. Lu, H. Wang, J. Pan, H. Li, X. Wu, W. Huang, Y. Yan, Enhanced photodegradation of antibiotics solution under visible light with Fe^{2+}/Fe^{3+} immobilized on TiO_2/fly-ash cenospheres by using ions imprinting technology, Chem. Eng. J. 172 (2011) 615–622, https://doi.org/10.1016/j.cej.2011.06.003.
[62] W. Zhang, S. Gao, D. Chen, Preparation of Ce^{3+} doped Bi_2O_3 hollow needle-shape with enhanced visible-light photocatalytic activity, J. Rare Earths 37 (2019) 726–731, https://doi.org/10.1016/j.jre.2018.12.007.
[63] Y. Chen, Q. Wu, L. Liu, J. Wang, Y. Song, The fabrication of self-floating Ti^{3+}/N co-doped TiO_2/diatomite granule catalyst with enhanced photocatalytic performance under visible light irradiation, Appl. Surf. Sci. 467–468 (2019) 514–525, https://doi.org/10.1016/j.apsusc.2018.10.146.
[64] J. Di, J. Xia, M. Ji, H. Li, H. Xu, H. Li, R. Chen, The synergistic role of carbon quantum dots for the improved photocatalytic performance of Bi_2MoO_6, Nanoscale 7 (2015) 11433–11443, https://doi.org/10.1039/C5NR01350J.
[65] Z. Liang, J. Yang, C. Zhou, Q. Mo, Y. Zhang, Carbon quantum dots modified BiOBr microspheres with enhanced visible light photocatalytic performance, Inorg. Chem. Commun. 90 (2018) 97–100, https://doi.org/10.1016/j.inoche.2018.02.013.
[66] S. Sharma, A. Umar, S.K. Mehta, A.O. Ibhadon, S.K. Kansal, Solar light driven photocatalytic degradation of levofloxacin using TiO_2/carbon-dot nanocomposites, New J. Chem. 42 (2018) 7445–7456, https://doi.org/10.1039/C7NJ05118B.
[67] A. Kaur, D.B. Salunke, A. Umar, S.K. Mehta, A. Sinha, S.K. Kansal, Visible light driven photocatalytic degradation of fluoroquinolone levofloxacin drug using Ag_2O/TiO_2 quantum dots: a mechanistic study and degradation pathway, New J. Chem. 41 (2017) 12079–12090, https://doi.org/10.1039/C7NJ02053H.
[68] J. Di, J. Xia, M. Ji, B. Wang, S. Yin, H. Xu, Z. Chen, H. Li, Carbon quantum dots induced ultrasmall BiOI nanosheets with assembled hollow structures for broad spectrum photocatalytic activity and mechanism insight, Langmuir 32 (2016) 2075–2084, https://doi.org/10.1021/acs.langmuir.5b04308.
[69] M. Ji, Z. Zhang, J. Xia, J. Di, Y. Liu, R. Chen, S. Yin, S. Zhang, H. Li, Enhanced photocatalytic performance of carbon quantum dots/BiOBr composite and mechanism investigation, Chin. Chem. Lett. 29 (2018) 805–810, https://doi.org/10.1016/j.cclet.2018.05.002.
[70] G. Gong, Y. Liu, B. Mao, B. Wang, L. Tan, D. Li, Y. Liu, W. Shi, Mechanism study on the photocatalytic efficiency enhancement of MoS_2 modified Zn-$AgIn_5S_8$ quantum dots, RSC Adv. 6 (2016) 99023–99033, https://doi.org/10.1039/c6ra19949f.
[71] J. Bai, Y. Li, P. Jin, J. Wang, L. Liu, Facile preparation 3D ZnS nanospheres-reduced graphene oxide composites for enhanced photodegradation of norfloxacin, J. Alloy. Compd. 729 (2017) 809–815, https://doi.org/10.1016/j.jallcom.2017.07.057.
[72] J. Lyu, J. Shao, Y. Wang, Y. Qiu, J. Li, T. Li, Y. Peng, F. Liu, Construction of a porous core-shell homojunction for the photocatalytic degradation of antibiotics, Chem. Eng. J. 358 (2019) 614–620, https://doi.org/10.1016/j.cej.2018.10.085.
[73] R. Hailili, Z.-Q. Wang, X.-Q. Gong, C. Wang, Octahedral-shaped perovskite CaCu3Ti4O12 with dual defects and coexposed (001), (111) facets for visible-light photocatalysis, Appl. Catal. B 254 (2019) 86–97, https://doi.org/10.1016/j.apcatb.2019.03.086.
[74] S. Bao, Z. Wang, X. Gong, C. Zeng, Q. Wu, B. Tian, J. Zhang, AgBr tetradecahedrons with co-exposed 100 and 111 facets: simple fabrication and enhancing spatial charge separation using facet heterojunctions, J. Mater. Chem. A 4 (2016) 18570–18577, https://doi.org/10.1039/c6ta06594e.
[75] J. Li, F. Liu, Y. Li, Fabrication of an Ag/Ag_2MoO_4 plasmonic photocatalyst with enhanced photocatalytic performance for the degradation of ciprofloxacin, New J. Chem. 42 (2018) 12054–12061, https://doi.org/10.1039/c8nj02327a.
[76] S.S. Boxi, S. Paria, Visible Light Induced Enhanced Photocatalytic Degradation of Organic Pollutants in Aqueous Media Using Ag Doped Hollow TiO_2 Nanospheres, RSC Adv. 5 (2015) 37657–37668, https://doi.org/10.1039/C5RA03421C.
[77] F. Cao, J. Wang, Y. Wang, J. Zhou, W. Fan, An in-situ Bi-decorated BiOBr Photocatalyst for Synchronously Treating Multiple Antibiotics in Water, Nanoscale Advances 1 (2019) 1124, https://doi.org/10.1039/c8na00197a.
[78] W. Zhu, L. Zhong, Z. Yan, X. Yan, Deposition of Silver nanoparticles onto two dimensional BiOCl nanodiscs for enhanced visible light photocatalytic and

biocidal activities, RSC Adv. 6 (2016) 64911–64920, https://doi.org/10.1039/c6ra09964e.
[79] E. Jiang, X. Liu, H. Che, C. Liu, H. Dong, G. Che, Visible-light-driven Ag/Bi_3O_4Cl nanocomposite photocatalyst with enhanced photocatalytic activity for degradation of tetracycline, RSC Adv. 8 (2018) 37200–37207, https://doi.org/10.1039/C8RA07482H.
[80] C. Tian, T. Xu, L. Sha, Q. Yan, Y. Wu, Cellulose Nanofibrils Anchored Ag on Graphitic Carbon Nitride for Efficient Photocatalysis under Visible Light, Environ. Sci. Nano 5 (2018) 1–44, https://doi.org/10.1039/C8EN00570B.
[81] L. Zhao, W. Song, O. Chao, W. Hao, D. Zeng, C. Xie, Enhanced visible-light photocatalytic performance of highly-dispersed Pt/g-C_3N_4 nanocomposites by one-step solvothermal treatment, RSC Adv. 7 (2017) 33552–33557, https://doi.org/10.1039/c7ra04931e.
[82] Z. Wei, J. Liu, W. Fang, M. Xu, Z. Qin, Z. Jiang, W. Shangguan, Photocatalytic hydrogen evolution with simultaneous antibiotic wastewater degradation via the visible-light-responsive bismuth spheres-g-C_3N_4 nanohybrid: Waste to energy insight, Chem. Eng. J. 358 (2019) 944–954, https://doi.org/10.1016/j.cej.2018.10.096.
[83] P. Demircivi, E.B. Simsek, Visible-light-enhanced photoactivity of perovskite-type W-doped $BaTiO_3$ photocatalyst for photodegradation of tetracycline, J. Alloy. Compd. 774 (2019) 795–802, https://doi.org/10.1016/j.jallcom.2018.09.354.
[84] J. Guo, Y. Li, D. Hu, H. Liu, Preparation of transition-metal-doped ZnO nano-photocatalysts and their performance on photocatalytic degradation of antibiotic wastewater, Desalin. Water Treat. (2014) 1–8, https://doi.org/10.1080/19443994.2014.961171.
[85] M. Salimi, M. Behbahani, H.R. Sobhi, M. Gholami, A.J. Jafari, R.R. Kalantary, M. Farzadkia, A. Esrafili, A new nano-photocatalyst based on Pt and Bi co-doped TiO_2 for efficient visible-light photo degradation of amoxicillin, New J. Chem. 43 (2019) 1562–1568, https://doi.org/10.1039/c8nj05020a.
[86] J. Xue, S. Ma, Y. Zhou, Z. Zhang, M. He, Facile photochemical synthesis of Au/Pt/g-C_3N_4 with plasmon-enhanced photocatalytic activity for antibiotic degradation, ACS Appl. Mater. Interfaces 7 (2015) 9630–9637, https://doi.org/10.1021/acsami.5b01212.
[87] K. Wang, Y. Li, G. Zhang, J. Li, X. Wu, 0D Bi nanodots/2D Bi_3NbO_7 nanosheets heterojunctions for efficient visible light photocatalytic degradation of antibiotics: Enhanced molecular oxygen activation and mechanism insight, Appl. Catal. B 240 (2019) 39–49, https://doi.org/10.1016/j.apcatb.2018.08.063.
[88] F. Chen, Q. Yang, J. Sun, F. Yao, S. Wang, Y. Wang, X. Wang, X. Li, C. Niu, D. Wang, Enhanced photocatalytic degradation of tetracycline by AgI/$BiVO_4$ heterojunction under visible-light irradiation: mineralization efficiency and mechanism, ACS Appl. Mater. Interfaces 8 (2016) 32887–32900, https://doi.org/10.1021/acsami.6b12278.
[89] Y.-B. Du, L. Zhang, M. Ruan, C.-G. Niu, X.-J. Wen, C. Liang, X.-G. Zhang, G.-M. Zeng, Template-free synthesis of three-dimensional porous CdS/TiO_2 with high stability and excellent visible photocatalytic activity, Mater. Chem. Phys. 212 (2018) 69–77, https://doi.org/10.1016/j.matchemphys.2018.03.033.
[90] W. Fan, M. Li, H. Bai, D. Xu, C. Chen, C. Li, Y. Ge, W. Shi, Fabrication of $MgFe_2O_4$/MoS_2 heterostructure nanowires for photoelectrochemical catalysis, Langmuir 32 (2016) 1629–1636, https://doi.org/10.1021/acs.langmuir.5b03887.
[91] P. Huo, Y. Tang, M. Zhou, J. Li, Z. Ye, C. Ma, L. Yu, Y. Yan, Fabrication of $ZnWO_4$-CdS heterostructure photocatalysts for visible light induced degradation of ciprofloxacin antibiotics, J. Ind. Eng. Chem. 37 (2016) 340–346, https://doi.org/10.1016/j.jiec.2016.03.043.
[92] B. Ji, J. Zhang, C. Zhang, N. Li, T. Zhao, F. Chen, L. Hu, S. Zhang, Z. Wang, Vertically aligned ZnO@ ZnS nanorod chip with improved photocatalytic activity for antibiotics degradation, ACS Applied Nano Materials 1 (2018) 793–799, https://doi.org/10.1021/acsanm.7b00242.
[93] M. Li, S. Yin, T. Wu, J. Di, M. Ji, B. Wang, Y. Chen, J. Xia, H. Li, Controlled preparation of MoS_2/$PbBiO_2I$ hybrid microspheres with enhanced visible-light photocatalytic behaviour, J. Colloid Interface Sci. 517 (2018) 278–287, https://doi.org/10.1016/j.jcis.2018.01.096.
[94] W. Li, Z. Wen, S. Tian, L. Shan, Y. Xiong, Citric acid-assisted hydrothermal synthesis of a self-modified Bi_2SiO_5/$Bi_{12}SiO_{20}$ heterojunction for efficient photocatalytic degradation of aqueous pollutants, Catal. Sci. Technol. 8 (2018) 1051–1061, https://doi.org/10.1039/x0xx00000x.
[95] C. Liu, G. Wu, J. Chen, K. Huang, W. Shi, Fabrication of a visible-light-driven photocatalyst and degradation of tetracycline based on the photoinduced interfacial charge transfer of $SrTiO_3$/Fe_2O_3 nanowires, New J. Chem. 40 (2016) 5198–5208, https://doi.org/10.1039/c5nj03167b.
[96] Z. Ma, L. Deng, G. Fan, Y. He, Hydrothermal synthesis of p-C_3N_4/f-BiOBr composites with highly efficient degradation of methylene blue and tetracycline, Spectrochim. Acta Part A Mol. Biomol. Spectrosc. 214 (2019) 103–110, https://doi.org/10.1016/j.saa.2019.02.008.
[97] H.F. Motlagh, M. Haghighi, M. Shabani, Sono-solvothermal fabrication of ball-flowerlike $Bi_2O_7Sn_2$-$Bi_7O_9I_3$ nanophotocatalyst with efficient solar-light-driven activity for degradation of antibiotic tetracycline, Sol. Energy 180 (2019) 25–38.
[98] A. Ren, C. Liu, Y. Hong, W. Shi, S. Lin, P. Li, Enhanced visible-light-driven photocatalytic activity for antibiotic degradation using magnetic $NiFe_2O_4$/Bi_2O_3 heterostructures, Chem. Eng. J. 258 (2014) 301–308, https://doi.org/10.1016/j.cej.2014.07.071.
[99] T. Soltani, A. Tayyebi, B.-K. Lee, Photolysis and photocatalysis of tetracycline by sonochemically heterojunctioned $BiVO_4$/reduced graphene oxide under visible-light irradiation, J. Environ. Manage. 232 (2019) 713–721, https://doi.org/10.1016/j.jenvman.2018.11.133.
[100] G. Wu, L. Xiao, W. Gu, W. Shi, D. Jiang, C. Liu, Fabrication and excellent visible-light-driven photodegradation activity for antibiotics of $SrTiO_3$ nanocube coated CdS microsphere heterojunctions, RSC Adv. 6 (2016) 19878–19886, https://doi.org/10.1039/c5ra21651f.
[101] J. Xia, J. Zhao, J. Chen, J. Di, M. Ji, L. Xu, Z. Chen, H. Li, Facile fabrication of g-C_3N_4/$BiPO_4$ hybrid materials via a reactable ionic liquid for the photocatalytic degradation of antibiotic ciprofloxacin, J. Photochem. Photobiol., A 339 (2017) 59–66, https://doi.org/10.1016/j.jphotochem.2017.02.010.
[102] H. Xu, H. Zhao, Y. Song, W. Yan, Y. Xu, H. Li, L. Huang, S. Yin, Y. Li, Q. Zhang, g-C_3N_4/Ag_3PO_4 composites with synergistic effect for increased photocatalytic activity under the visible light irradiation, Mater. Sci. Semicond. Process. 39 (2015) 726–734, https://doi.org/10.1016/j.mssp.2015.04.013.
[103] J. Xu, B. Luo, W. Gu, Y. Jian, F. Wu, Y. Tang, H. Shen, Fabrication of In_2S_3/$NaTaO_3$ composites for enhancing the photocatalytic activity toward the degradation of tetracycline, New J. Chem. 42 (2018) 5052–5058, https://doi.org/10.1039/C7NJ05123A.
[104] Y. Xu, Y. Ma, H. Ji, S. Huang, M. Xie, Y. Zhao, H. Xu, H. Li, Enhanced long-wavelength light utilization with polyaniline/bismuth-rich bismuth oxyhalide composite towards photocatalytic degradation of antibiotics, J. Colloid Interface Sci. 537 (2019) 101–111, https://doi.org/10.1016/j.jcis.2018.10.109.
[105] C. Yang, J. Cheng, Y. Chen, Y. Hu, CdS nanoparticles immobilized on porous carbon polyhedrons derived from a metal-organic framework with enhanced visible light photocatalytic activity for antibiotic degradation, Appl. Surf. Sci. 420 (2017) 252–259, https://doi.org/10.1016/j.apsusc.2017.05.102.
[106] X. Yuan, L. Jiang, J. Liang, Y. Pan, J. Zhang, H. Wang, L. Leng, Z. Wu, R. Guan, G. Zeng, In-situ synthesis of 3D microsphere-like In_2S_3/$InVO_4$ heterojunction with efficient photocatalytic activity for tetracycline degradation under visible light irradiation, Chem. Eng. J. 356 (2019) 371–381, https://doi.org/10.1016/j.cej.2018.09.079.
[107] J. Zhao, M. Ji, J. Di, Y. Ge, P. Zhang, J. Xia, H. Li, Synthesis of g-C_3N_4/Bi_4O_5Br 2 via reactable ionic liquid and its cooperation effect for the enhanced photocatalytic behavior towards ciprofloxacin degradation, J. Photochem. Photobiol., A 347 (2017) 168–176.
[108] Y. Zhao, X. Liang, Y. Wang, H. Shi, E. Liu, J. Fan, X. Hu, Degradation and removal of Ceftriaxone sodium in aquatic environment with Bi_2WO_6/g-C_3N_4 photocatalyst, J. Colloid Interface Sci. 523 (2018) 7–17, https://doi.org/10.1016/j.jcis.2018.03.078.
[109] H. Zhen, M.A. Khan, M. Xia, W. Lei, F. Wang, Controllable synthesis of flower-root shaped Bi_2O_3/Bi_2MoO_6 heterostructures as an efficient photocatalyst under visible light irradiation, J. Photochem. Photobiol., A 372 (2019) 78–88, https://doi.org/10.1016/j.jphotochem.2018.11.021.
[110] S.-R. Zhu, Q. Qi, Y. Fang, W.-N. Zhao, M.-K. Wu, L. Han, Covalent triazine framework modified BiOBr nanoflake with enhanced photocatalytic activity for antibiotic removal, Cryst. Growth Des. 18 (2017) 883–891, https://doi.org/10.1021/acs.cgd.7b01367.
[111] X. Zhu, J. Liu, Z. Zhao, J. Yan, Y. Xu, Y. Song, H. Ji, H. Xu, H. Li, Hydrothermal synthesis of mpg-C_3N_4 and Bi_2WO_6 nest-like structure nanohybrids with enhanced visible light photocatalytic activities, RSC Adv. 7 (2017) 38682–38690, https://doi.org/10.1039/c7ra06681c.
[112] Y. Jin, D. Jiang, D. Li, M. Chen, Construction of ultrafine TiO_2 nanoparticle and $SnNb_2O_6$ nanosheet 0D/2D heterojunctions with abundant interfaces and significantly improved photocatalytic activity, Catal. Sci. Technol. 7 (2017) 2308–2317, https://doi.org/10.1039/c7cy00366h.
[113] W. Liu, Z. Dai, Y. Liu, A. Zhu, D. Zhong, J. Wang, J. Pan, Intimate contacted two-dimensional/zero-dimensional composite of bismuth titanate nanosheets supported ultrafine bismuth oxychloride nanoparticles for enhanced antibiotic residue degradation, J. Colloid Interface Sci. 529 (2018) 23–33, https://doi.org/10.1016/j.jcis.2018.05.112.
[114] M. Ji, J. Di, Y. Ge, J. Xia, H. Li, 2D–2D stacking of graphene-like g-C_3N_4/Ultrathin Bi_4O_5Br 2 with matched energy band structure towards antibiotic removal, Appl. Surf. Sci. 413 (2017) 372–380, https://doi.org/10.1016/j.apsusc.2017.03.287.
[115] K. Qian, L. Xia, Z. Jiang, W. Wei, L. Chen, J. Xie, In situ chemical transformation synthesis of $Bi_4Ti_3O_{12}$/I–BiOCl 2D/2D heterojunction systems for water pollution treatment and hydrogen production, Catal. Sci. Technol. 7 (2017) 3863–3875, https://doi.org/10.1039/C7CY01162H.
[116] C. Zhou, C. Lai, P. Xu, G. Zeng, D. Huang, Z. Li, C. Zhang, M. Cheng, L. Hu, J. Wan, Rational design of carbon-doped carbon nitride/$Bi_{12}O_{17}Cl_2$ composites: a promising candidate photocatalyst for boosting visible-light-driven photocatalytic degradation of tetracycline, ACS Sustainable Chem. Eng. 6 (2018) 6941–6949, https://doi.org/10.1021/acssuschemeng.8b00782.
[117] Y. Ao, J. Bao, P. Wang, C. Wang, J. Hou, Bismuth oxychloride modified titanium phosphate nanoplates: a new p-n type heterostructured photocatalyst with high activity for the degradation of different kinds of organic pollutants, J. Colloid Interface Sci. 476 (2016) 71–78, https://doi.org/10.1016/j.jcis.2016.05.021.
[118] F. Guo, W. Shi, H. Wang, M. Han, H. Li, H. Huang, Y. Liu, Z. Kang, Facile fabrication of a CoO/g-C_3N_4 p-n heterojunction with enhanced photocatalytic activity and stability for tetracycline degradation under visible light, Catal. Sci. Technol. 7 (2017) 3325–3331, https://doi.org/10.1039/c7cy00960g.
[119] C. Liu, P. Li, G. Wu, B. Luo, S. Lin, A. Ren, W. Shi, Enhanced photoelectrochemical and photocatalytic activity by Cu_2O/$SrTiO_3$ p–n heterojunction via a facile deposition–precipitation technique, RSC Adv. 5 (2015) 33938–33945, https://doi.org/10.1039/c5ra03086b.
[120] S. Li, J. Chen, Y. Liu, K. Xu, J. Liu, In situ anion exchange strategy to construct flower-like BiOCl/BiOCOOH pn heterojunctions for efficiently photocatalytic removal of aqueous toxic pollutants under solar irradiation, J. Alloy. Compd. 781 (2019) 582–588, https://doi.org/10.1016/j.jallcom.2018.12.114.
[121] S. Ma, J. Xue, Y. Zhou, Z. Zhang, Enhanced visible-light photocatalytic activity of Ag_2O/g-C_3N_4 p–n heterojunctions synthesized via a photochemical route for

degradation of tetracycline hydrochloride, RSC Adv. 5 (2015) 40000–40006, https://doi.org/10.1039/c5ra04075b.
[122] P. Suyana, P. Ganguly, B.N. Nair, A.P. Mohamed, K. Warrier, U. Hareesh, Co_3O_4-C_3N_4 p-n nano-heterojunctions for the simultaneous degradation of a mixture of pollutants under solar irradiation, Environ. Sci. Nano 4 (2017) 212–221, https://doi.org/10.1039/c6en00410e.
[123] J. Wang, G. Zhang, J. Li, K. Wang, Novel three-dimensional flowerlike BiOBr/Bi_2SiO_5 p-n heterostructured nanocomposite for degradation of tetracycline: Enhanced visible light photocatalytic activity and mechanism, ACS Sustainable Chem. Eng. 6 (2018) 14221–14229, https://doi.org/10.1021/acssuschemeng.8b02869.
[124] X.-J. Wen, C.-G. Niu, L. Zhang, G.-M. Zeng, Fabrication of SnO_2 nanoparticles/BiOI n-p heterostructure for wider spectrum visible-light photocatalytic degradation of antibiotic oxytetracycline hydrochloride, ACS Sustainable Chem. Eng. 5 (2017) 5134–5147, https://doi.org/10.1021/acssuschemeng.7b00501.
[125] M. Yan, Y. Hua, F. Zhu, W. Gu, J. Jiang, H. Shen, W. Shi, Fabrication of nitrogen doped graphene quantum dots-BiOI/$MnNb_2O_6$ p-n junction photocatalysts with enhanced visible light efficiency in photocatalytic degradation of antibiotics, Appl. Catal. B 202 (2017) 518–527, https://doi.org/10.1016/j.apcatb.2016.09.039.
[126] R. Jiang, D. Wu, G. Lu, Z. Yan, J. Liu, R. Zhou, M. Nkoom, Fabrication of Fe_3O_4 quantum dots modified BiOCl/$BiVO_4$ pn heterojunction to enhance photocatalytic activity for removing broad-spectrum antibiotics under visible light, J. Taiwan Inst. Chem. Eng. 96 (2019) 681–690, https://doi.org/10.1016/j.jtice.2019.01.010.
[127] C. Liu, J. Chen, H. Che, K. Huang, P.A. Charpentier, W.Z. Xu, W. Shi, H. Dong, Construction and enhanced photocatalytic activities of a hydrogenated TiO_2 nanobelt coated with CDs/MoS_2 nanosheets, RSC Adv. 7 (2017) 8429–8442, https://doi.org/10.1039/c6ra28479e.
[128] J. Li, M. Zhou, Z. Ye, H. Wang, C. Ma, P. Huo, Y. Yan, Enhanced photocatalytic activity of g-C_3N_4-ZnO/HNT composite heterostructure photocatalysts for degradation of tetracycline under visible light irradiation, RSC Adv. 5 (2015) 91177–91189, https://doi.org/10.1039/C5RA17360D.
[129] S. Zhang, H. Gao, Y. Huang, X. Wang, T. Hayat, J. Li, X. Xu, X. Wang, Ultrathin g-C_3N_4 nanosheets coupled with amorphous Cu-doped FeOOH nanoclusters as 2D/0D heterogeneous catalysts for water remediation, Environ. Sci. Nano 5 (2018) 1179–1190, https://doi.org/10.1039/C8EN00124C.
[130] W.-K. Jo, S. Tonda, Novel CoAl-LDH/g-C_3N_4/RGO ternary heterojunction with notable 2D/2D/2D configuration for highly efficient visible-light-induced photocatalytic elimination of dye and antibiotic pollutants, J. Hazard. Mater. 368 (2019) 778–787, https://doi.org/10.1016/j.jhazmat.2019.01.114.
[131] D. Chen, B. Li, Q. Pu, X. Chen, G. Wen, Z. Li, Preparation of Ag-$AgVO_3$/g-C_3N_4 composite photo-catalyst and degradation characteristics of antibiotics, J. Hazard. Mater. 373 (2019) 303–312, https://doi.org/10.1016/j.jhazmat.2019.03.090.
[132] L. Jing, Y. Xu, C. Qin, J. Liu, S. Huang, M. He, H. Xu, H. Li, Visible-light-driven $ZnFe_2O_4$/Ag/Ag_3VO_4 photocatalysts with enhanced photocatalytic activity under visible light irradiation, Mater. Res. Bull. 95 (2017) 607–615, https://doi.org/10.1016/j.materresbull.2017.06.003.
[133] X. Lu, Y. Wang, X. Zhang, G. Xu, D. Wang, J. Lv, Z. Zheng, Y. Wu, NiS and MoS_2 nanosheet co-modified graphitic C_3N_4 ternary heterostructure for high efficient visible light photodegradation of antibiotic, J. Hazard. Mater. 341 (2018) 10–19, https://doi.org/10.1016/j.jhazmat.2017.07.004.
[134] L. Zhou, W. Zhang, L. Chen, H. Deng, J. Wan, A novel ternary visible-light-driven photocatalyst AgCl/Ag_3PO_4/g-C_3N_4: Synthesis, characterization, photocatalytic activity for antibiotic degradation and mechanism analysis, Catal. Commun. 100 (2017) 191–195, https://doi.org/10.1016/j.catcom.2017.06.049.
[135] N. Shao, J. Wang, D. Wang, P. Corvini, Preparation of three-dimensional Ag_3PO_4/TiO_2@ MoS_2 for enhanced visible-light photocatalytic activity and anti-photocorrosion, Appl. Catal. B 203 (2017) 964–978, https://doi.org/10.1016/j.apcatb.2016.11.008.
[136] B. Priya, P. Raizada, N. Singh, P. Thakur, P. Singh, Adsorptional photocatalytic mineralization of oxytetracycline and ampicillin antibiotics using Bi_2O_3/BiOCl supported on graphene sand composite and chitosan, J. Colloid Interface Sci. 479 (2016) 271–283, https://doi.org/10.1016/j.jcis.2016.06.067.
[137] W. Shi, D. Lu, L. Wang, F. Teng, J. Zhang, Core-shell structured Fe_3O_4@ SiO_2@ CdS nanoparticles with enhanced visible-light photocatalytic activities, RSC Adv. 5 (2015) 106038–106043, https://doi.org/10.1039/C5RA22295H.
[138] Y. Tang, X. Liu, C. Ma, M. Zhou, P. Huo, L. Yu, J. Pan, W. Shi, Y. Yan, Enhanced photocatalytic degradation of tetracycline antibiotics by reduced graphene oxide-CdS/ZnS heterostructure photocatalysts, New J. Chem. 39 (2015) 5150–5160, https://doi.org/10.1039/c5nj00681c.
[139] P. Xu, X. Shen, L. Luo, Z. Shi, Z. Liu, Z. Chen, M. Zhu, L. Zhang, Preparation of TiO_2/Bi_2WO_6 nanostructured heterojunctions on carbon fibers as a weaveable visible-light photocatalyst/photoelectrode, Environ. Sci. Nano 5 (2018) 327–337, https://doi.org/10.1039/C7EN00822H.
[140] Y. Hong, C. Li, B. Yin, D. Li, Z. Zhang, B. Mao, W. Fan, W. Gu, W. Shi, Promoting visible-light-induced photocatalytic degradation of tetracycline by an efficient and stable beta-Bi_2O_3@ g-C_3N_4 core/shell nanocomposite, Chem. Eng. J. 338 (2018) 137–146, https://doi.org/10.1016/j.cej.2017.12.108.
[141] W. Zhu, F. Sun, R. Goei, Y. Zhou, Construction of WO_3-g-C_3N_4 composites as efficient photocatalysts for pharmaceutical degradation under visible light, Catal. Sci. Technol. 7 (2017) 2591–2600, https://doi.org/10.1039/x0xx00000x.
[142] F. Chen, Q. Yang, F. Yao, S. Wang, J. Sun, H. An, K. Yi, Y. Wang, Y. Zhou, L. Wang, Visible-light photocatalytic degradation of multiple antibiotics by AgI nanoparticle-sensitized Bi_5O_7I microspheres: Enhanced interfacial charge transfer based on Z-scheme heterojunctions, J. Catal. 352 (2017) 160–170, https://doi.org/10.1016/j.jcat.2017.04.032.
[143] Y. Gong, Y. Wu, Y. Xu, L. Li, C. Li, X. Liu, L. Niu, All-solid-state Z-scheme CdTe/TiO_2 heterostructure photocatalysts with enhanced visible-light photocatalytic degradation of antibiotic waste water, Chem. Eng. J. 350 (2018) 257–267, https://doi.org/10.1016/j.cej.2018.05.186.
[144] F. Guo, W. Shi, H. Wang, M. Han, W. Guan, H. Huang, Y. Liu, Z. Kang, Study on highly enhanced photocatalytic tetracycline degradation of type II AgI/$CuBi_2O_4$ and Z-scheme AgBr/$CuBi_2O_4$ heterojunction photocatalysts, J. Hazard. Mater. 349 (2018) 111–118, https://doi.org/10.1016/j.jhazmat.2018.01.042.
[145] C. Li, S. Yu, H. Dong, C. Liu, H. Wu, H. Che, G. Chen, Z-scheme mesoporous photocatalyst constructed by modification of Sn_3O_4 nanoclusters on g-C_3N_4 nanosheets with improved photocatalytic performance and mechanism insight, Appl. Catal. B 238 (2018) 284–293, https://doi.org/10.1016/j.apcatb.2018.07.049.
[146] K. Wang, G. Zhang, J. Li, Y. Li, X. Wu, 0D/2D Z-scheme heterojunctions of bismuth tantalate quantum dots/ultrathin g-C_3N_4 nanosheets for highly efficient visible light photocatalytic degradation of antibiotics, ACS Appl. Mater. Interfaces 9 (2017) 43704–43715, https://doi.org/10.1021/acsami.7b14275.
[147] X. Ma, D. Jiang, P. Xiao, Y. Jin, S. Meng, M. Chen, 2D/2D heterojunctions of WO_3 nanosheet/K^+ $Ca_2Nb_3O_{10}$−ultrathin nanosheet with improved charge separation efficiency for significantly boosting photocatalysis, Catal. Sci. Technol. 7 (2017) 3481–3491, https://doi.org/10.1039/x0xx00000x.
[148] H. Yu, B. Huang, H. Wang, X. Yuan, L. Jiang, Z. Wu, J. Zhang, G. Zeng, Facile construction of novel direct solid-state Z-scheme AgI/BiOBr photocatalysts for highly effective removal of ciprofloxacin under visible light exposure: Mineralization efficiency and mechanisms, J. Colloid Interface Sci. 522 (2018) 82–94, https://doi.org/10.1016/j.jcis.2018.03.056.
[149] L. Zhou, W. Zhang, L. Chen, H. Deng, Z-scheme mechanism of photogenerated carriers for hybrid photocatalyst Ag_3PO_4/g-C_3N_4 in degradation of sulfamethoxazole, J. Colloid Interface Sci. 487 (2017) 410–417, https://doi.org/10.1016/j.jcis.2016.10.068.
[150] S. Bao, Q. Wu, S. Chang, B. Tian, J. Zhang, Z-scheme CdS-Au-$BiVO_4$ with enhanced photocatalytic activity for organic contaminant decomposition, Catal. Sci. Technol. 7 (2017) 124–132, https://doi.org/10.1039/C6CY01980C.
[151] Y. Deng, L. Tang, G. Zeng, C. Feng, H. Dong, J. Wang, H. Feng, Y. Liu, Y. Zhou, Y. Pang, Plasmonic resonance excited dual Z-scheme $BiVO_4$/Ag/Cu_2O nanocomposite: synthesis and mechanism for enhanced photocatalytic performance in recalcitrant antibiotic degradation, Environ. Sci. Nano 4 (2017) 1494–1511, https://doi.org/10.1039/c7en00237h.
[152] Z. Lu, Z. Yu, J. Dong, M. Song, L. Yang, X. Liu, Z. Ma, S. Hang, Y. Yan, P. Huo, Facile microwave synthesis of a Z-scheme imprinted $ZnFe_2O_4$/Ag/PEDOT with the specific recognition ability towards improving photocatalytic activity and selectivity for tetracycline, Chem. Eng. J. 337 (2018) 228–241, https://doi.org/10.1016/j.cej.2017.12.115.
[153] P. Mondal, J. Satra, U.K. Ghorui, N. Saha, D.N. Srivastava, B. Adhikary, Facile Fabrication of Novel Hetero-Structured Organic-Inorganic High-Performance Nanocatalyst: A Smart System for Enhanced Catalytic Activity toward Ciprofloxacin Degradation and Oxygen Reduction, ACS Applied Nano Materials 1 (2018) 6015–6026, https://doi.org/10.1021/acsanm.8b00937.
[154] Q. Li, Z. Guan, D. Wu, X. Zhao, S. Bao, B. Tian, J. Zhang, Z-scheme BiOCl-Au-CdS heterostructure with enhanced sunlight-driven photocatalytic activity in degrading water dyes and antibiotics, ACS Sustainable Chem. Eng. 5 (2017) 6958–6968, https://doi.org/10.1021/acssuschemeng.7b01157.
[155] Y. Yang, Z. Zeng, C. Zhang, D. Huang, G. Zeng, R. Xiao, C. Lai, C. Zhou, H. Guo, W. Xue, Construction of iodine vacancy-rich BiOI/Ag@AgI Z-scheme heterojunction photocatalysts for visible-light-driven tetracycline degradation: transformation pathways and mechanism insight, Chem. Eng. J. 349 (2018) 808–821, https://doi.org/10.1016/j.cej.2018.05.093.
[156] X. Yuan, L. Jiang, X. Chen, L. Leng, H. Wang, Z. Wu, T. Xiong, J. Liang, G. Zeng, Highly efficient visible-light-induced photoactivity of Z-scheme Ag_2CO_3/Ag/WO_3 photocatalysts for organic pollutant degradation, Environ. Sci. Nano 4 (2017) 2175–2185, https://doi.org/10.1039/C7EN00713B.
[157] M. Ren, J. Chen, P. Wang, J. Hou, J. Qian, C. Wang, Y. Ao, Construction of silver iodide/silver/Bismuth Tantalate Z-scheme photocatalyst for effective visible light degradation of organic pollutants, J. Colloid Interface Sci. 532 (2018) 190–200, https://doi.org/10.1016/j.jcis.2018.07.141.
[158] S.K. Patra, S. Rahut, J.K. Basu, Enhanced Z-scheme photocatalytic activity of a π-conjugated heterojunction: MIL-53 (Fe)/Ag/g-C_3N_4, New J. Chem. 42 (2018) 18598–18607, https://doi.org/10.1039/c8nj04080j.
[159] Q. Liu, J. Shen, X. Yang, T. Zhang, H. Tang, 3D reduced graphene oxide aerogel-mediated Z-scheme photocatalytic system for highly efficient solar-driven water oxidation and removal of antibiotics, Appl. Catal. B 232 (2018) 562–573, https://doi.org/10.1016/j.apcatb.2018.03.100.
[160] K. Hu, C. Chen, Y. Zhu, G. Zeng, B. Huang, W. Chen, S. Liu, C. Lei, B. Li, Y. Yang, Ternary Z-scheme heterojunction of Bi_2WO_6 with reduced graphene oxide (rGO) and meso-tetra (4-carboxyphenyl) porphyrin (TCPP) for enhanced visible-light photocatalysis, J. Colloid Interface Sci. 540 (2019) 115–125, https://doi.org/10.1016/j.jcis.2019.01.013.
[161] B. Shao, X. Liu, Z. Liu, G. Zeng, Q. Liang, C. Liang, Y. Cheng, W. Zhang, Y. Liu, S. Gong, A novel double Z-scheme photocatalyst Ag_3PO_4/Bi_2S_3/Bi_2O_3 with enhanced visible-light photocatalytic performance for antibiotic degradation, Chem. Eng. J. 6 (2019) 16426–16436, https://doi.org/10.1016/j.cej.2019.03.013.
[162] X. Hu, X. Liu, J. Tian, Y. Li, H. Cui, Towards full-spectrum (UV, visible, and near-infrared) photocatalysis: achieving an all-solid-state Z-scheme between Ag_2O and TiO_2 using reduced graphene oxide as the electron mediator, Catal. Sci. Technol. 7 (2017) 4193–4205, https://doi.org/10.1039/C7CY01349C.
[163] H.-Y. Liu, C. Liang, C.-G. Niu, D.-W. Huang, Y.-B. Du, H. Guo, L. Zhang, Y.-Y. Yang, G.-M. Zeng, Facile assembly of g-C_3N_4/Ag_2CO_3/graphene oxide with a novel dual

Z-scheme system for enhanced photocatalytic pollutant degradation, Appl. Surf. Sci. 475 (2019) 421–434, https://doi.org/10.1016/j.apsusc.2019.01.018.
[164] M. Yan, F. Zhu, W. Gu, L. Sun, W. Shi, Y. Hua, Construction of nitrogen-doped graphene quantum dots-$BiVO_4$/g-C_3N_4 Z-scheme photocatalyst and enhanced photocatalytic degradation of antibiotics under visible light, RSC Adv. 6 (2016) 61162–61174, https://doi.org/10.1039/c6ra07589d.
[165] J. Wang, H. Chen, L. Tang, G. Zeng, Y. Liu, M. Yan, Y. Deng, H. Feng, J. Yu, L. Wang, Antibiotic removal from water: A highly efficient silver phosphate-based Z-scheme photocatalytic system under natural solar light, Sci. Total Environ. 639 (2018) 1462–1470, https://doi.org/10.1016/j.scitotenv.2018.05.258.
[166] Z. Pan, W. Ma, L. Wang, Construction of a magnetic Z-scheme photocatalyst with enhanced oxidation/reduction abilities and recyclability for the degradation of tetracycline, RSC Adv. 6 (2016) 114374–114382, https://doi.org/10.1039/c6ra24096h.
[167] B. Shao, Z. Liu, G. Zeng, Z. Wu, Y. Liu, M. Cheng, M. Chen, Y. Liu, W. Zhang, H. Feng, Nitrogen-Doped Hollow Mesoporous Carbon Spheres Modified g-C_3N_4/Bi_2O_3 Direct Dual Semiconductor Photocatalytic System with Enhanced Antibiotics Degradation under Visible Light, ACS Sustainable Chem. Eng. 6 (2018) 16424–16436, https://doi.org/10.1021/acssuschemeng.8b03480.
[168] L. Hao, H. Huang, Y. Guo, Y. Zhang, Multifunctional Bi2O2(OH)(NO3) nanosheets with 001 active exposing facets: efficient photocatalysis, dye-sensitization, and piezoelectric-catalysis, ACS Sustainable Chem. Eng. 6 (2018) 1848–1862, https://doi.org/10.1021/acssuschemeng.7b03223.
[169] X. Wu, K. Li, Y. Li, G. Zhang, Motivating visible light photocatalytic activity of ultrathin Bi2O2(OH)xCl2−x solid solution with exposed 001 facets by the co-effect of oxygen vacancy and OH replacement, Nanoscale 10 (2018) 15294–15302, https://doi.org/10.1039/C8NR04469D.
[170] J. Xu, Z. Bian, X. Xin, A. Chen, H. Wang, Size dependence of nanosheet BiVO4 with oxygen vacancies and exposed 0 0 1 facets on the photodegradation of oxytetracycline, Chem. Eng. J. 337 (2018) 684–696, https://doi.org/10.1016/j.cej.2017.12.133.
[171] Y. Ma, Q. Liu, Q. Wang, D. Qu, J. Shi, Insight into the origin of photoreactivity of various well-defined Bi_2WO_6 crystals: exposed heterojunction-like surface and oxygen defects, RSC Adv. 6 (2016) 18916–18923, https://doi.org/10.1039/c5ra27295e.
[172] W. Liu, Y. Shang, A. Zhu, P. Tan, Y. Liu, L. Qiao, D. Chu, X. Xiong, J. Pan, Enhanced performance of doped BiOCl nanoplates for photocatalysis: understanding from doping insight into improved spatial carrier separation, J. Mater. Chem. A 5 (2017) 12542–12549, https://doi.org/10.1039/C7TA02724A.
[173] Z. Jiang, X. Lv, D. Jiang, J. Xie, D. Mao, Natural leaves-assisted synthesis of nitrogen-doped, carbon-rich nanodots-sensitized, Ag-loaded anatase TiO2 square nanosheets with dominant 001 facets and their enhanced catalytic applications, J. Mater. Chem. A 1 (2013) 14963–14972, https://doi.org/10.1039/c3ta13248j.
[174] W. Wang, J. Fang, S. Shao, M. Lai, C. Lu, Compact and uniform TiO_2@ g-C_3N_4 core-shell quantum heterojunction for photocatalytic degradation of tetracycline antibiotics, Appl. Catal. B 217 (2017) 57–64, https://doi.org/10.1016/j.apcatb.2017.05.037.
[175] Z. Zhu, W. Fan, Z. Liu, H. Dong, Y. Yan, P. Huo, Construction of an attapulgite intercalated mesoporous g-C_3N_4 with enhanced photocatalytic activity for antibiotic degradation, J. Photochem. Photobiol., A 359 (2018) 102–110, https://doi.org/10.1016/j.jphotochem.2018.04.003.
[176] A. Dehghan, M.H. Dehghani, R. Nabizadeh, N. Ramezanian, M. Alimohammadi, A.A. Najafpoor, Adsorption and visible-light photocatalytic degradation of tetracycline hydrochloride from aqueous solutions using 3D hierarchical mesoporous BiOI: synthesis and characterization, process optimization, adsorption and degradation modeling, Chem. Eng. Res. Des. 129 (2018) 217–230, https://doi.org/10.1016/j.cherd.2017.11.003.
[177] J. Di, J. Xia, Y. Ge, L. Xu, H. Xu, M. He, Q. Zhang, H. Li, Reactable ionic liquid-assisted rapid synthesis of BiOI hollow microspheres at room temperature with enhanced photocatalytic activity, J. Mater. Chem. A 2 (2014) 15864–15874, https://doi.org/10.1039/c4ta02400a.
[178] G. Gupta, A. Umar, A. Kaur, S. Sood, A. Dhir, S. Kansal, Solar light driven photocatalytic degradation of Ofloxacin based on ultra-thin bismuth molybdenum oxide nanosheets, Mater. Res. Bull. 99 (2018) 359–366, https://doi.org/10.1016/j.materresbull.2017.11.033.
[179] R. Karthik, J.V. Kumar, S.-M. Chen, P.S. Kumar, V. Selvam, V. Muthuraj, A selective electrochemical sensor for caffeic acid and photocatalyst for metronidazole drug pollutant - A dual role by rod-like SrV_2O_6, Sci. Rep. 7 (2017) 7254, https://doi.org/10.1038/s41598-017-07423-1.
[180] Q. Chen, H. Liu, Y. Xin, X. Cheng, TiO_2 nanobelts-Effect of calcination temperature on optical, photoelectrochemical and photocatalytic properties, Electrochim. Acta 111 (2013) 284–291, https://doi.org/10.1016/j.electacta.2013.08.049.
[181] C. Bojer, J. Schöbel, T. Martin, M. Ertl, H. Schmalz, J. Breu, Clinical wastewater treatment: Photochemical removal of an anionic antibiotic (ciprofloxacin) by mesostructured high aspect ratio ZnO nanotubes, Appl. Catal. B 204 (2017) 561–565, https://doi.org/10.1016/j.apcatb.2016.12.003.
[182] R. Hailili, Z.-Q. Wang, M. Xu, Y. Wang, X.-Q. Gong, T. Xu, C. Wang, Layered nanostructured ferroelectric perovskite $Bi_5FeTi_3O_{15}$ for visible light photodegradation of antibiotics, J. Mater. Chem. A 5 (2017) 21275–21290, https://doi.org/10.1039/c7ta06618j.
[183] Q. Chen, Y. Mao, N. Bing, Y. Zou, L. Zhu, Preparation and optical properties of three-dimensional navel-like Bi_2WO_6 hierarchical microspheres, Chin. Chem. Lett. 30 (2018) 783–786, https://doi.org/10.1016/j.cclet.2018.10.036.
[184] D. Hernández-Uresti, A. Vázquez, S. Obregón, M. Ruíz-Gómez, Novel g-C_3N_4 photocatalytic coatings with spearhead-like morphology prepared by an electrophoretic deposition route, Mater. Lett. 200 (2017) 59–62, https://doi.org/10.1016/j.matlet.2017.04.097.
[185] S. Chen, W. Lu, J. Han, H. Zhong, T. Xu, G. Wang, W. Chen, Robust three-dimensional g-C_3N_4@cellulose aerogel enhanced by cross-linked polyester fibers for simultaneous removal of hexavalent chromium and antibiotics, Chem. Eng. J. 359 (2019) 119–129, https://doi.org/10.1016/j.cej.2018.11.110.
[186] X. Yang, Z. Chen, J. Fang, Q. Yang, W. Zhao, X. Qian, D. Zhou, C. Liu, M. Chen, Freestanding 3D MoS_2 nanosheets/graphene aerogel heterostructure as a recyclable photocatalyst for efficiently degrading antibiotic residues, Mater. Lett. 252 (2019) 5–7, https://doi.org/10.1016/j.matlet.2019.05.084.
[187] S. Bai, N. Zhang, C. Gao, Y. Xiong, Defect engineering in photocatalytic materials, Nano Energy 53 (2018) 296–336, https://doi.org/10.1016/j.nanoen.2018.08.058.
[188] N. Zhang, C. Gao, Y. Xiong, Defect engineering: a versatile tool for tuning the activation of key molecules in photocatalytic reactions, Journal of Energy Chemistry 37 (2019) 43–57, https://doi.org/10.1016/j.jechem.2018.09.010.
[189] D. Chen, Y. Zou, S. Wang, Surface chemical-functionalization of ultrathin two-dimensional nanomaterials for electrocatalysis, Mater. Today Energy 12 (2019) 250–268, https://doi.org/10.1016/j.mtener.2019.01.006.
[190] H.L. Tan, R. Amal, Y.H. Ng, Alternative strategies in improving the photocatalytic and photoelectrochemical activities of visible light-driven $BiVO_4$: a review, J. Mater. Chem. A 5 (2017) 16498–16521, https://doi.org/10.1039/c7ta04441k.
[191] C. Du, Q. Zhang, Z. Lin, B. Yan, C. Xia, G. Yang, Half-unit-cell $ZnIn_2S_4$ monolayer with sulfur vacancies for photocatalytic hydrogen evolution, Appl. Catal. B 248 (2019) 193–201, https://doi.org/10.1016/j.apcatb.2019.02.027.
[192] Y. Han, J. Zhou, J. Dong, Electronic and magnetic properties of MoS_2 nanoribbons with sulfur line vacancy defects, Appl. Surf. Sci. 346 (2015) 470–476, https://doi.org/10.1016/j.apsusc.2015.02.016.
[193] G. Li, C. Fu, J. Wu, J. Rao, S.-C. Liou, X. Xu, B. Shao, K. Liu, E. Liu, N. Kumar, X. Liu, M. Fahlman, J. Gooth, G. Auffermann, Y. Sun, C. Felser, B. Zhang, Synergistically creating sulfur vacancies in semimetal-supported amorphous MoS_2 for efficient hydrogen evolution, Appl. Catal. B 254 (2019) 1–6, https://doi.org/10.1016/j.apcatb.2019.04.080.
[194] X. Li, Y. Cheng, Q. Wu, J. Xu, Y. Wang, Synergistic effect of the rearranged sulfur vacancies and sulfur interstitials for 13-fold enhanced photocatalytic H_2 production over defective $Zn_2In_2S_5$ nanosheets, Appl. Catal. B 240 (2019) 270–276, https://doi.org/10.1016/j.apcatb.2018.09.008.
[195] H. Shang, T. Wang, W. Zhang, Sulfur vacancy formation at different MoS_2 edges during hydrodesulfurization process: A DFT study, Chem. Eng. Sci. 195 (2019) 208–217, https://doi.org/10.1016/j.ces.2018.11.049.
[196] I. Eliyahu, Y.S. Horowitz, L. Oster, I. Mardor, S. Druzhyna, S. Biderman, Kinetic modeling of Fluorine vacancy/F center creation in LiF:Mg, Ti including vacancy-interstitial recombination: Evaluating the factors leading to the lack of supralinearity in the optical absorption F center concentration dose response, Nucl. Instrum. Methods Phys. Res., Sect. B 343 (2015) 15–25, https://doi.org/10.1016/j.nimb.2014.11.017.
[197] Q. Wang, Z. Liu, D. Liu, G. Liu, M. Yang, F. Cui, W. Wang, Ultrathin two-dimensional $BiOBr_xI_{1-x}$ solid solution with rich oxygen vacancies for enhanced visible-light-driven photoactivity in environmental remediation, Appl. Catal. B 236 (2018) 222–232, https://doi.org/10.1016/j.apcatb.2018.05.029.
[198] B. Anzaldo Olivares, O.P. Moreno, G.H. Téllez, E.R. Rosas, F.J.M. Bustamante, M.E. Castro Sánchez, P. Sharma, A. Mendoza, R.G. Pérez, Green emission band induced by crystal defects in halogenated (-Br, -Cl, -F) chiral imines with a benzo [b]thiophene-based moiety, Opt. Mater. 94 (2019) 337–347, https://doi.org/10.1016/j.optmat.2019.06.007.
[199] Y. Yang, Z. Zeng, Z. Chen, D. Huang, G. Zeng, X. Rong, L. Cui, C. Zhou, G. Hai, W. Xue, Construction of iodine vacancy-rich BiOI/Ag@AgI Z-scheme heterojunction photocatalysts for visible-light-driven tetracycline degradation: transformation pathways and mechanism insight, Chem. Eng. J. 349 (2018) 808–821, https://doi.org/10.1016/j.cej.2018.05.093.
[200] J. Cao, W. Nie, L. Huang, Y. Ding, K. Lv, H. Tang, Photocatalytic activation of sulfite by nitrogen vacancy modified graphitic carbon nitride for efficient degradation of carbamazepine, Appl. Catal. B 241 (2019) 18–27, https://doi.org/10.1016/j.apcatb.2018.09.007.
[201] J. Cao, C. Pan, Y. Ding, W. Li, K. Lv, H. Tang, Constructing nitrogen vacancy introduced g-C_3N_4 p-n homojunction for enhanced photocatalytic activity, J. Environ. Chem. Eng. 7 (2019) 102984, , https://doi.org/10.1016/j.jece.2019.102984.
[202] L. Liang, L. Shi, F. Wang, L. Yao, Y. Zhang, W. Qi, Synthesis and photo-catalytic activity of porous g-C3N4: Promotion effect of nitrogen vacancy in H2 evolution and pollutant degradation reactions, Int. J. Hydrogen Energy 44 (2019) 16315–16326, https://doi.org/10.1016/j.ijhydene.2019.05.001.
[203] M. Ji, R. Chen, J. Di, Y. Liu, K. Li, Z. Chen, J. Xia, H. Li, Oxygen vacancies modulated Bi-rich bismuth oxyiodide microspheres with tunable valence band position to boost the photocatalytic activity, J. Colloid Interface Sci. 533 (2019) 612–620, https://doi.org/10.1016/j.jcis.2018.08.097.
[204] J. Liu, F. Xie, R. Li, T. Li, Z. Jia, Y. Wang, Y. Wang, X. Zhang, C. Fan, TiO_{2-x}/Ag_3PO_4 photocatalyst: Oxygen vacancy dependent visible light photocatalytic performance and BPA degradative pathway, Mater. Sci. Semicond. Process. 97 (2019) 1–10, https://doi.org/10.1016/j.mssp.2019.03.002.
[205] W. Qi, F. Zhang, X. An, H. Liu, J. Qu, Oxygen vacancy modulation of {010}-dominated TiO_2 for enhanced photodegradation of Sulfamethoxazole, Catal. Commun. 118 (2019) 35–38, https://doi.org/10.1016/j.catcom.2018.09.014.
[206] Z. Song, X. Dong, J. Fang, C. Xiong, N. Wang, X. Tang, Improved photocatalytic degradation of perfluorooctanoic acid on oxygen vacancies-tunable bismuth oxychloride nanosheets prepared by a facile hydrolysis, J. Hazard. Mater. 377 (2019) 371–380, https://doi.org/10.1016/j.jhazmat.2019.05.084.
[207] M. Singh, D. Jampaiah, A.E. Kandjani, Y.M. Sabri, E. Della Gaspera, P. Reineck,

M. Judd, J. Langley, N. CoxJ., van Embden, Oxygen-deficient photostable Cu_2O for enhanced visible light photocatalytic activity, Nanoscale 10 (2018) 6039–6050, https://doi.org/10.1039/C7NR08388B.
[208] Y. Bai, L. Ye, T. Chen, L. Wang, X. Shi, X. Zhang, D. Chen, Facet-Dependent Photocatalytic N_2 Fixation of Bismuth-Rich Bi_5O_7I Nanosheets, ACS Appl. Mater. Interfaces 8 (2016) 27661–27668, https://doi.org/10.1021/acsami.6b08129.
[209] J. Di, C. Chen, C. Zhu, M. Ji, J. Xia, C. Yan, W. Hao, S. Li, H. Li, Z. Liu, Bismuth vacancy mediated single unit cell Bi_2WO_6 nanosheets for boosting photocatalytic oxygen evolution, Appl. Catal. B 238 (2018) 119–125, https://doi.org/10.1016/j.apcatb.2018.06.066.
[210] X. Jin, L. Ye, H. Xie, G. Chen, Bismuth-rich bismuth oxyhalides for environmental and energy photocatalysis, Coord. Chem. Rev. 349 (2017) 84–101, https://doi.org/10.1016/j.ccr.2017.08.010.
[211] S. Cao, B. Fan, Y. Feng, H. Chen, F. Jiang, X. Wang, Sulfur-doped g-C_3N_4 nanosheets with carbon vacancies: General synthesis and improved activity for simulated solar-light photocatalytic nitrogen fixation, Chem. Eng. J. 353 (2018) 147–156, https://doi.org/10.1016/j.cej.2018.07.116.
[212] Y. Pan, Y.Q. Li, Q.H. Zheng, Y. Xu, Point defect of titanium sesquioxide Ti_2O_3 as the application of next generation Li-ion batteries, J. Alloy. Compd. 786 (2019) 621–626, https://doi.org/10.1016/j.jallcom.2019.02.054.
[213] T. Wang, L. Liu, G. Ge, M. Liu, W. Zhou, K. Chang, F. Yang, D. Wang, J. Ye, Two-dimensional titanium oxide nanosheets rich in titanium vacancies as an efficient cocatalyst for photocatalytic water oxidation, J. Catal. 367 (2018) 296–305, https://doi.org/10.1016/j.jcat.2018.09.026.
[214] F. Zuo, L. Wang, T. Wu, Z. Zhang, D. Borchardt, P. Feng, Self-doped Ti^{3+} enhanced photocatalyst for hydrogen production under visible light, J. Am. Chem. Soc. 132 (2010) 11856–11857, https://doi.org/10.1002/chin.201049012.
[215] X. Chen, L. Liu, Y.Y. Peter, S.S. Mao, Increasing solar absorption for photocatalysis with black hydrogenated titanium dioxide nanocrystals, Science 331 (2011) 746–750, https://doi.org/10.1126/science.1198640.
[216] M.K. Nowotny, L.R. Sheppard, T. Bak, J. Nowotny, Defect chemistry of titanium dioxide. Application of defect engineering in processing of TiO2-based photocatalysts, The Journal of Physical Chemistry C 112 (2008) 5275–5300, https://doi.org/10.1002/chin.200831228.
[217] L. Ren, W. Zhou, B. Sun, H. Li, P. Qiao, Y. Xu, J. Wu, K. Lin, H. Fu, Defects-engineering of magnetic γ-Fe_2O_3 ultrathin nanosheets/mesoporous black TiO_2 hollow sphere heterojunctions for efficient charge separation and the solar-driven photocatalytic mechanism of tetracycline degradation, Appl. Catal. B 240 (2019) 319–328, https://doi.org/10.1016/j.apcatb.2018.08.033.
[218] X. Liu, H. Xu, L.R. Grabstanowicz, S. Gao, Z. Lou, W. WangB. huang, Y. Dai, T. Xu,, Ti^{3+} self-doped TiO_{2-x} anatase nanoparticles via oxidation of TiH_2 in H_2O_2, Catal. Today 225 (2014) 80–89, https://doi.org/10.1016/j.cattod.2013.08.025.
[219] M. Wen, S. Zhang, W. Dai, G. Li, D. Zhang, In situ synthesis of Ti^{3+} self-doped mesoporous TiO_2 as a durable photocatalyst for environmental remediation, Chin. J. Catal. 36 (2015) 2095–2102, https://doi.org/10.1016/s1872-2067(15)60992-5.
[220] M. Xing, W. Fang, M. Nasir, Y. Ma, J. Zhang, M. Anpo, Self-doped Ti^{3+}-enhanced TiO_2 nanoparticles with a high-performance photocatalysis, J. Catal. 297 (2013) 236–243, https://doi.org/10.1016/j.jcat.2012.10.014.
[221] X. Wang, Y. Li, X. Liu, S. Gao, B. Huang, Y. Dai, Preparation of Ti^{3+} self-doped TiO_2 nanoparticles and their visible light photocatalytic activity, Chin. J. Catal. 36 (2015) 389–399, https://doi.org/10.1016/s1872-2067(14)60234-5.
[222] J. Wang, P. Yang, B. Huang, Self-doped TiO_{2-x} nanowires with enhanced photocatalytic activity: Facile synthesis and effects of the Ti^{3+}, Appl. Surf. Sci. 356 (2015) 391–398, https://doi.org/10.1016/j.apsusc.2015.08.029.
[223] X. Deng, H. Zhang, R. Guo, Q. Ma, Y. Cui, X. Cheng, M. Xie, Q. Cheng, Effect of Ti^{3+} on enhancing photocatalytic and photoelectrochemical properties of TiO_2 nanorods/nanosheets photoelectrode, Sep. Purif. Technol. 192 (2018) 329–339, https://doi.org/10.1016/j.seppur.2017.10.029.
[224] M.A. Mohamed, M.F.M. Zain, L. Jeffery Minggu, M.B. Kassim, J. Jaafar, N.A. Saidina Amin, M.S. Mastuli, H. Wu, R.J. Wong, Y.H. Ng, Bio-inspired hierarchical hetero-architectures of in-situ C-doped g-C_3N_4 grafted on C, N co-doped ZnO micro-flowers with booming solar photocatalytic activity, J. Ind. Eng. Chem. 77 (2019) 393–407, https://doi.org/10.1016/j.jiec.2019.05.003.
[225] A. Fakhri, R. Khakpour, Synthesis and characterization of carbon or/and boron-doped CdS nanoparticles and investigation of optical and photoluminescence properties, J. Lumin. 160 (2015) 233–237, https://doi.org/10.1016/j.jlumin.2014.12.019.
[226] Q. Gu, J. Liu, Z. Gao, C. Xue, Homogenous boron-doping in self-sensitized carbon nitride for enhanced visible-light photocatalytic activity, Chemistry-An Asian Journal 11 (2016) 3169–3173, https://doi.org/10.1002/asia.201601201.
[227] R.P. Cavalcante, R.F. Dantas, H. Wender, B. Bayarri, O. González, J. Giménez, S. Esplugas, A. Machulek, Photocatalytic treatment of metoprolol with B-doped TiO_2: Effect of water matrix, toxicological evaluation and identification of intermediates, Appl. Catal. B 176–177 (2015) 173–182, https://doi.org/10.1016/j.apcatb.2015.04.007.
[228] A.E. Giannakas, M. Antonopoulou, C. Daikopoulos, Y. Deligiannakis, I. Konstantinou, Characterization and catalytic performance of B-doped, B-N co-doped and B–N–F tri-doped TiO_2 towards simultaneous Cr(VI) reduction and benzoic acid oxidation, Appl. Catal. B 184 (2016) 44–54, https://doi.org/10.1016/j.apcatb.2015.11.009.
[229] J. Zheng, Z. Liu, X. Liu, X. Yan, D. Li, W. Chu, Facile hydrothermal synthesis and characteristics of B-doped TiO_2 hybrid hollow microspheres with higher photocatalytic activity, J. Alloy. Compd. 509 (2011) 3771–3776, https://doi.org/10.1016/j.jallcom.2010.12.152.
[230] Z. Liu, K. Sun, M. Wei, Z. Ma, Phosphorus-doped cerium vanadate nanorods with enhanced photocatalytic activity, J. Colloid Interface Sci. 531 (2018) 618–627, https://doi.org/10.1016/j.jcis.2018.07.077.
[231] N. Farhadian, R. Akbarzadeh, M. Pirsaheb, T.C. Jen, Y. Fakhri, A. Asadi, Chitosan modified N, S-doped TiO_2 and N, S-doped ZnO for visible light photocatalytic degradation of tetracycline, Int. J. Biol. Macromol. 132 (2019) 360–373, https://doi.org/10.1016/j.ijbiomac.2019.03.217.
[232] Y. Jia, C. Wu, B.W. Lee, C. Liu, S. Kang, T. Lee, Y.C. Park, R. Yoo, W. Lee, Magnetically separable sulfur-doped $SnFe_2O_4$/graphene nanohybrids for effective photocatalytic purification of wastewater under visible light, J. Hazard. Mater. 338 (2017) 447–457, https://doi.org/10.1016/j.jhazmat.2017.05.057.
[233] H. Huang, Y. Song, N. Li, D. Chen, Q. Xu, H. Li, J. He, J. Lu, One-step in-situ preparation of N-doped TiO_2@C derived from Ti_3C_2 MXene for enhanced visible-light driven photodegradation, Appl. Catal. B 251 (2019) 154–161, https://doi.org/10.1016/j.apcatb.2019.03.066.
[234] W.C. Huang, J.-M. Ting, Novel nitrogen-doped anatase TiO_2 mesoporous bead photocatalysts for enhanced visible light response, Ceram. Int. 43 (2017) 9992–9997, https://doi.org/10.1016/j.ceramint.2017.05.012.
[235] T. Suwannaruang, P. Kidkhunthod, N. Chanlek, S. Soontaranon, K. Wantala, High anatase purity of nitrogen-doped TiO_2 nanorice particles for the photocatalytic treatment activity of pharmaceutical wastewater, Appl. Surf. Sci. 478 (2019) 1–14, https://doi.org/10.1016/j.apsusc.2019.01.158.
[236] V. Vaiano, O. Sacco, D. Sannino, P. Ciambelli, Photocatalytic removal of spiramycin from wastewater under visible light with N-doped TiO_2 photocatalysts, Chem. Eng. J. 261 (2015) 3–8, https://doi.org/10.1016/j.cej.2014.02.071.
[237] P. Dumrongrojthanath, A. Phuruangrat, S. Thongtem, T. Thongtem, Hydrothermal preparation of visible-light-driven Br-doped Bi_2WO_6 photocatalyst, Mater. Lett. 209 (2017) 501–504, https://doi.org/10.1016/j.matlet.2017.08.089.
[238] M. Guo, H. He, J. Cao, H. Lin, S. Chen, Novel I-doped $Bi_{12}O_{17}Cl_2$ photocatalysts with enhanced photocatalytic activity for contaminants removal, Mater. Res. Bull. 112 (2019) 205–212, https://doi.org/10.1016/j.materresbull.2018.12.023.
[239] H. Sekhar, D.N. Rao, Spectroscopic studies on Fe^{3+} doped CdS nanopowders prepared by simple coprecipitation method, J. Alloy. Compd. 517 (2012) 103–110, https://doi.org/10.1016/j.jallcom.2011.12.039.
[240] X. Yan, C. Xue, B. Yang, G. Yang, Novel three-dimensionally ordered macroporous Fe^{3+}-doped TiO_2 photocatalysts for H_2 production and degradation applications, Appl. Surf. Sci. 394 (2017) 248–257, https://doi.org/10.1016/j.apsusc.2016.10.077.
[241] D.P. Dutta, P. Raval, Effect of transition metal ion (Cr^{3+}, Mn^{2+} and Cu^{2+}) doping on the photocatalytic properties of $ZnWO_4$ nanoparticles, J. Photochem. Photobiol., A 357 (2018) 193–200, https://doi.org/10.1016/j.jphotochem.2018.02.026.
[242] Y. Zou, Y. Gong, B. Lin, N.P. Mellott, Photodegradation of methylene blue in the visible spectrum: An efficient W^{6+} ion doped anatase titania photocatalyst via a solvothermal method, Vacuum 126 (2016) 63–69, https://doi.org/10.1016/j.vacuum.2016.01.018.
[243] J. Wang, Y. Sun, C. Wu, Z. Cui, P. Rao, Enhancing photocatalytic activity of Bi_2MoO_6 via surface co-doping with Ni^{2+} and Ti^{4+} ions, J. Phys. Chem. Solids 129 (2019) 209–216, https://doi.org/10.1016/j.jpcs.2019.01.014.
[244] A. Gaurav, R. Beura, J.S. Kumar, P. Thangadurai, Study on the effect of copper ion doping in zinc oxide nanomaterials for photocatalytic applications, Mater. Chem. Phys. 230 (2019) 162–171, https://doi.org/10.1016/j.matchemphys.2019.03.056.
[245] F. Li, H. Li, L.-X. Guan, M.-M. Yao, Nanocrystalline Co^{2+}/F^- codoped TiO_2–SiO_2 composite films for environmental applications, Chem. Eng. J. 252 (2014) 1–10, https://doi.org/10.1016/j.cej.2014.04.107.
[246] Y. Liu, G. Zhu, J. Gao, R. Zhu, M. Hojamberdiev, C. Wang, X. Wei, P. Liu, A novel synergy of Er^{3+}/Fe^{3+} co-doped porous Bi_5O_7I microspheres with enhanced photocatalytic activity under visible-light irradiation, Appl. Catal. B 205 (2017) 421–432, https://doi.org/10.1016/j.apcatb.2016.12.061.
[247] A. Petala, D. Tsikritzis, M. Kollia, S. Ladas, S. Kennou, D.I. Kondarides, Synthesis and characterization of N-doped TiO_2 photocatalysts with tunable response to solar radiation, Appl. Surf. Sci. 305 (2014) 281–291, https://doi.org/10.1016/j.apsusc.2014.03.062.
[248] M. Wang, P. Guo, Y. Zhang, C. Lv, T. Liu, T. Chai, Y. Xie, Y. Wang, T. Zhu, Synthesis of hollow lantern-like Eu(III)-doped g-C_3N_4 with enhanced visible light photocatalytic perfomance for organic degradation, J. Hazard. Mater. 349 (2018) 224–233, https://doi.org/10.1016/j.jhazmat.2018.01.058.
[249] Q. Que, Y. Xing, Z. He, Y. Yang, X. Yin, W. Que, Bi_2O_3/Carbon quantum dots heterostructured photocatalysts with enhanced photocatalytic activity, Mater. Lett. 209 (2017) 220–223, https://doi.org/10.1016/j.matlet.2017.07.115.
[250] S. Sharma, V. Dutta, P. Singh, P. Raizada, A. Rahmani-Sani, A. Hosseini-Bandegharaei, V.K. Thakur, Carbon quantum dot supported semiconductor photocatalysts for efficient degradation of organic pollutants in water: A review, J. Cleaner Prod. 228 (2019) 755–769, https://doi.org/10.1016/j.jclepro.2019.04.292.
[251] J. Zhang, M. Kuang, J. Wang, R. Liu, S. Xie, Z. Ji, Fabrication of carbon quantum dots/TiO_2/Fe_2O_3 composites and enhancement of photocatalytic activity under visible light, Chem. Phys. Lett. 730 (2019) 391–398, https://doi.org/10.1016/j.cplett.2019.06.011.
[252] Z. Zhang, L. Wu, P. Wang, Y. Zhang, S. Wan, X. Guo, W. Jin, J. Zhang, Carbon quantum dots modified $La_2Ti_2O_7$ nanosheets for visible light photocatalysis, Mater. Lett. 230 (2018) 72–75, https://doi.org/10.1016/j.matlet.2018.07.086.
[253] F. Zhao, Y. Rong, J. Wan, Z. Hu, Z. Peng, B. Wang, High photocatalytic performance of carbon quantum dots/TNTs composites for enhanced photogenerated charges separation under visible light, Catal. Today 315 (2018) 162–170, https://doi.org/10.1016/j.cattod.2018.02.019.

[254] A. Yuan, H. Lei, F. Xi, J. Liu, L. Qin, Z. Chen, X. Dong, Graphene quantum dots decorated graphitic carbon nitride nanorods for photocatalytic removal of antibiotics, J Colloid Interface Sci 548 (2019) 56–65, https://doi.org/10.1016/j.jcis.2019.04.027.

[255] M.I. Aziz, F. Mughal, H.M. Naeem, A. Zeb, M.A. Tahir, M.A. Basit, Evolution of photovoltaic and photocatalytic activity in anatase-TiO_2 under visible light via simplistic deposition of CdS and PbS quantum-dots, Mater. Chem. Phys. 229 (2019) 508–513, https://doi.org/10.1016/j.matchemphys.2019.03.042.

[256] Y. Zhu, Y. Wang, Z. Chen, L. Qin, L. Yang, L. Zhu, P. Tang, T. Gao, Y. Huang, Z. Sha, G. Tang, Visible light induced photocatalysis on CdS quantum dots decorated TiO_2 nanotube arrays, Appl. Catal. A: Gen. 498 (2015) 159–166, https://doi.org/10.1016/j.apcata.2015.03.035.

[257] R. Jiang, D. Wu, G. Lu, Z. Yan, J. Liu, R. Zhou, M. Nkoom, Fabrication of Fe_3O_4 quantum dots modified BiOCl/$BiVO_4$ p-n heterojunction to enhance photocatalytic activity for removing broad-spectrum antibiotics under visible light, J. Taiwan Inst. Chem. Eng. 96 (2019) 681–690, https://doi.org/10.1016/j.jtice.2019.01.010.

[258] X. Lin, C. Liu, J. Wang, S. Yang, J. Shi, Y. Hong, Graphitic carbon nitride quantum dots and nitrogen-doped carbon quantum dots co-decorated with $BiVO_4$ microspheres: A ternary heterostructure photocatalyst for water purification, Sep. Purif. Technol. 226 (2019) 117–127, https://doi.org/10.1016/j.seppur.2019.05.093.

[259] X. Qian, Z. Chen, X. Yang, W. Zhao, C. Liu, T. Sun, D. Zhou, Q. Yang, G. Wei, M. Fan, Perovskite cesium lead bromide quantum dots: a new efficient photocatalyst for degrading antibiotic residues in organic system, J. Clean. Prod. 249 (2019) 119335, , https://doi.org/10.1016/j.jclepro.2019.119335.

[260] Y. Liu, C.F. Li, X.Y. Li, W.B. Yu, W.D. Dong, H. Zhao, Z.Y. Hu, Z. Deng, C. Wang, S.J. Wu, H. Chen, J. Liu, Z. Wang, L.H. Chen, Y. Li, B.L. Su, Molybdenum disulfide quantum dots directing zinc indium sulfide heterostructures for enhanced visible light hydrogen production, J. Colloid Interface Sci. 551 (2019) 111–118, https://doi.org/10.1016/j.jcis.2019.05.001.

[261] K.-Q. Lu, Q. Quan, N. Zhang, Y.-J. Xu, Multifarious roles of carbon quantum dots in heterogeneous photocatalysis, Journal of Energy Chemistry 25 (2016) 927–935, https://doi.org/10.1016/j.jechem.2016.09.015.

[262] J. Liu, J. Huo, M. Zhang, X. Dong, Branched TiO_2 nanorod arrays owning the surface anatase/rutile junctions for dye sensitized solar cells, Thin Solid Films 623 (2017) 25–30, https://doi.org/10.1016/j.tsf.2016.12.042.

[263] J. Liu, X. Yu, Q. Liu, R. Liu, X. Shang, S. Zhang, W. Li, W. Zheng, G. Zhang, H. Cao, Z. Gu, Surface-phase junctions of branched TiO_2 nanorod arrays for efficient photoelectrochemical water splitting, Appl. Catal. B 158–159 (2014) 296–300, https://doi.org/10.1016/j.apcatb.2014.04.032.

[264] L.-X. Pang, X.-Y. Wang, X.-D. Tang, Enhanced photocatalytic performance of porous TiO_2 nanobelts with phase junctions, Solid State Sci. 39 (2015) 29–33, https://doi.org/10.1016/j.solidstatesciences.2014.11.004.

[265] Y. Qiu, F. Ouyang, Fabrication of TiO_2 hierarchical architecture assembled by nanowires with anatase/TiO_2(B) phase-junctions for efficient photocatalytic hydrogen production, Appl. Surf. Sci. 403 (2017) 691–698, https://doi.org/10.1016/j.apsusc.2017.01.255.

[266] X. Wang, S. Shen, Z. Feng, C. Li, Time-resolved photoluminescence of anatase/rutile TiO_2 phase junction revealing charge separation dynamics, Chin. J. Catal. 37 (2016) 2059–2068, https://doi.org/10.1016/s1872-2067(16)62574-3.

[267] Y. Zhou, C. Chen, N. Wang, Y. Li, H. Ding, Stable Ti^{3+} Self-Doped Anatase-Rutile Mixed TiO_2 with Enhanced Visible Light Utilization and Durability, The Journal of Physical Chemistry C 120 (2016) 6116–6124, https://doi.org/10.1021/acs.jpcc.6b00655.

[268] Y.-D. Zhou, Z.-Y. Zhao, Interfacial structure and properties of TiO_2 phase junction studied by DFT calculations, Appl. Surf. Sci. 485 (2019) 8–21, https://doi.org/10.1016/j.apsusc.2019.04.193.

[269] R. Liu, H. Li, L. Duan, H. Shen, Q. Zhang, X. Zhao, Influences of annealing atmosphere on phase transition temperature, optical properties and photocatalytic activities of TiO_2 phase-junction microspheres, J. Alloy. Compd. 789 (2019) 1015–1021, https://doi.org/10.1016/j.jallcom.2019.02.198.

[270] C. Byrne, L. Moran, D. Hermosilla, N. Merayo, Á. Blanco, S. Rhatigan, S. Hinder, P. Ganguly, M. Nolan, S.C. Pillai, Effect of Cu doping on the anatase-to-rutile phase transition in TiO_2 photocatalysts: theory and experiments, Appl. Catal. B 246 (2019) 266–276, https://doi.org/10.1016/j.apcatb.2019.01.058.

[271] Z. Ai, G. Zhao, Y. Zhong, Y. Shao, B. Huang, Y. Wu, X. Hao, Phase junction CdS: high efficient and stable photocatalyst for hydrogen generation, Appl. Catal. B 221 (2018) 179–186, https://doi.org/10.1016/j.apcatb.2017.09.002.

[272] Y. Shi, L. Luo, Y. Zhang, Y. Chen, S. Wang, L. Li, Y. Long, F. Jiang, Synthesis and characterization of α/β-Bi_2O_3 with enhanced photocatalytic activity for 17α-ethynylestradiol, Ceram. Int. 43 (2017) 7627–7635, https://doi.org/10.1016/j.ceramint.2017.03.057.

[273] W. Zhao, X. Liu, X. Yang, C. Liu, X. Qian, T. Sun, W. Chang, J. Zhang, Z. Chen, Synthesis of Novel 1T/2H-MoS_2 from MoO_3 Nanowires with Enhanced Photocatalytic Performance, Nanomaterials 10 (2020) 1124, https://doi.org/10.3390/nano10061124.

[274] Y. Chen, J. He, J. Li, M. Mao, Z. Yan, W. Wang, J. Wang, Hydrilla derived $ZnIn_2S_4$ photocatalyst with hexagonal-cubic phase junctions: A bio-inspired approach for H_2 evolution, Catal. Commun. 87 (2016) 1–5, https://doi.org/10.1016/j.catcom.2016.08.031.

[275] Y. Ma, X. Wang, C. Li, Charge separation promoted by phase junctions in photocatalysts, Chin. J. Catal. 36 (2015) 1519–1527, https://doi.org/10.1016/s1872-2067(15)60874-9.

[276] K. Yang, X. Li, C. Yu, D. Zeng, F. Chen, K. Zhang, W. Huang, H. Ji, Review on heterophase/homophase junctions for efficient photocatalysis: The case of phase transition construction, Chin. J. Catal. 40 (2019) 796–818, https://doi.org/10.1016/s1872-2067(19)63290-0.

[277] Z.-J. Jia, Z.-Y. Zhao, Properties of phase transition and interfaces of Cu_2ZnSnS_4 with hetero-phase junctions, Appl. Surf. Sci. 481 (2019) 1044–1052, https://doi.org/10.1016/j.apsusc.2019.03.201.

[278] C. Lv, G. Chen, X. Zhou, C. Zhang, Z. Wang, B. Zhao, D. Li, Oxygen-Induced Bi^{5+}-Self-Doped $Bi_4V_2O_{11}$ with a p-n Homojunction Toward Promoting the Photocatalytic Performance, ACS Appl Mater Interfaces 9 (2017) 23748–23755, https://doi.org/10.1021/acsami.7b05302.

[279] J. Pan, G. Liu, Facet control of photocatalysts for water splitting, Semiconductors for Photocatalysis (2017) 349–391.

[280] H.L. Tan, X. Wen, R. Amal, Y.H. Ng, BiVO4 010 and 110 relative exposure extent: governing factor of surface charge population and photocatalytic activity, J. Phys. Chem. Lett. 7 (2016) 1400–1405, https://doi.org/10.1021/acs.jpclett.6b00428.

[281] H. Wu, H.L. Tan, C.Y. Toe, J. Scott, L. Wang, R. Amal, Y.H. Ng, Photocatalytic and photoelectrochemical systems: similarities and differences, Adv. Mater. 32 (2020) 1904717, https://doi.org/10.1002/adma.201904717.

[282] F. He, S. Wang, H. Zhao, Y. Wang, J. Zhang, Q. Yan, P. Dong, Z. Tai, L. Chen, Y. Wang, C. Zhao, Construction of Schottky-type Ag-loaded fiber-like carbon nitride photocatalysts for tetracycline elimination and hydrogen evolution, Appl. Surf. Sci. 485 (2019) 70–80, https://doi.org/10.1016/j.apsusc.2019.04.164.

[283] A. Gołąbiewska, W. Lisowski, M. Jarek, G. Nowaczyk, M. Michalska, S. Jurga, A. Zaleska-Medynska, The effect of metals content on the photocatalytic activity of TiO_2 modified by Pt/Au bimetallic nanoparticles prepared by sol-gel method, Molecular Catalysis 442 (2017) 154–163, https://doi.org/10.1016/j.mcat.2017.09.004.

[284] X. Yang, Z. Chen, D. Zhou, W. Zhao, X. Qian, Q. Yang, T. Sun, C. Shen, Ultra-low Au-Pt Co-decorated TiO_2 nanotube arrays: construction and its improved visible-light-induced photocatalytic properties, Sol. Energy Mater. Sol. Cells 201 (2019) 110065, , https://doi.org/10.1016/j.solmat.2019.110065.

[285] W. Li, B. Li, M. Meng, Y. Cui, Y. Wu, Y. Zhang, H. Dong, Y. Feng, Bimetallic Au/Ag decorated TiO_2 nanocomposite membrane for enhanced photocatalytic degradation of tetracycline and bactericidal efficiency, Appl. Surf. Sci. 487 (2019) 1008–1017, https://doi.org/10.1016/j.apsusc.2019.05.162.

[286] P. Lisowski, J.C. Colmenares, D. Łomot, O. Chernyayeva, D. Lisovytskiy, Preparation by sonophotodeposition method of bimetallic photocatalysts Pd-Cu/TiO_2 for sustainable gaseous selective oxidation of methanol to methyl formate, J. Mol. Catal. A: Chem. 411 (2016) 247–256, https://doi.org/10.1016/j.molcata.2015.10.031.

[287] K.L. Reddy, S. Kumar, A. Kumar, V. Krishnan, Wide spectrum photocatalytic activity in lanthanide-doped upconversion nanophosphors coated with porous TiO_2 and Ag-Cu bimetallic nanoparticles, J. Hazard. Mater. 367 (2019) 694–705, https://doi.org/10.1016/j.jhazmat.2019.01.004.

[288] H. Huang, C. Liu, H. Ou, T. Ma, Y. Zhang, Self-sacrifice transformation for fabrication of type-I and type-II heterojunctions in hierarchical BixOyIz/g-C_3N_4 for efficient visible-light photocatalysis, Appl. Surf. Sci. 470 (2019) 1101–1110, https://doi.org/10.1016/j.apsusc.2018.11.193.

[289] Y. Zhu, T. Wan, X. Wen, D. Chu, Y. Jiang, Tunable Type I and II heterojunction of CoO_x nanoparticles confined in g-C_3N_4 nanotubes for photocatalytic hydrogen production, Appl. Catal. B 244 (2019) 814–822, https://doi.org/10.1016/j.apcatb.2018.12.015.

[290] A.J. Bard, Photoelectrochemistry and heterogeneous photo-catalysis at semiconductors, Journal of Photochemistry 10 (1979) 59–75, https://doi.org/10.1016/0047-2670(79)80037-4.

[291] H. Li, W. Tu, Y. Zhou, Z. Zou, Z-Scheme Photocatalytic Systems for Promoting Photocatalytic Performance: Recent Progress and Future Challenges, Adv. Sci. 3 (2016) 1500389, https://doi.org/10.1002/advs.201500389.

[292] P. Zhou, J. Yu, M. Jaroniec, All-solid-state Z-scheme photocatalytic systems, Adv. Mater. 26 (2014) 4920–4935, https://doi.org/10.1002/adma.201400288.

[293] J. Low, C. Jiang, B. Cheng, S. Wageh, A.A. Al-Ghamdi, J. Yu, A review of direct Z-scheme photocatalysts, Small Methods 1 (2017) 1700080, https://doi.org/10.1002/smtd.201700080.

[294] J. Low, J. Yu, M. Jaroniec, S. Wageh, A.A. Al-Ghamdi, Heterojunction photocatalysts, Adv. Mater. 29 (2017) 1601694, https://doi.org/10.1002/adma.201601694.

[295] D. Zhou, B. Yu, Q. Chen, H. Shi, Y. Zhang, D. Li, X. Yang, W. Zhao, C. Liu, G. Wei, Z. Chen, Improved visible light photocatalytic activity on Z-scheme g-C_3N_4 decorated TiO_2 nanotube arrays by a simple impregnation method, Mater. Res. Bull. 124 (2020) 110757, , https://doi.org/10.1016/j.materresbull.2019.110757.

[296] D. Zhou, Z. Chen, Q. Yang, C. Shen, G. Tang, S. Zhao, J. Zhang, D. Chen, Q. Wei, X. Dong, Facile construction of g-C_3N_4 nanosheets/TiO_2 nanotube arrays as Z-scheme photocatalyst with enhanced visible-light performance, ChemCatChem 8 (2016) 3064–3073, https://doi.org/10.1002/cctc.201600828.

[297] Y. Tang, D. Zhang, Y. Li, B. Huang, H. Li, X. Pu, Y. Geng, Fabrication of magnetically recoverable Ag/$CuNb_2O_6$/$CuFe_2O_4$ ternary heterojunction composite for highly efficient photocatalytic degradation of pollutants, Sep. Purif. Technol. 220 (2019) 78–88, https://doi.org/10.1016/j.seppur.2019.03.049.

[298] X. Wang, H. Fan, P. Ren, Effects of exposed facets on photocatalytic properties of WO_3, Adv. Powder Technol. 28 (2017) 2549–2555, https://doi.org/10.1016/j.apt.2017.07.005.

[299] B. Peng, P.K. Ang, K.P. Loh, Two-dimensional dichalcogenides for light-harvesting applications, Nano Today 10 (2015) 128–137, https://doi.org/10.1016/j.nantod.2015.01.007.

[300] Y. Li, C. Gao, R. Long, Y. Xiong, Photocatalyst design based on two-dimensional materials, Mater. Today Chem. 11 (2019) 197–216, https://doi.org/10.1016/j.mtchem.2018.11.002.

[301] C. Tan, X. Cao, X.J. Wu, Q. He, J. Yang, X. Zhang, J. Chen, W. Zhao, S. Han,

G.H. Nam, M. Sindoro, H. Zhang, Recent Advances in Ultrathin Two-Dimensional Nanomaterials, Chem. Rev. 117 (2017) 6225–6331, https://doi.org/10.1021/acs.chemrev.6b00558.
[302] K. Yang, J. Li, L. Zhou, T. Zhang, L. Fu, Synthetic strategies of two-dimensional porous materials towards highly effective catalysts, FlatChem 15 (2019) 100109, , https://doi.org/10.1016/j.flatc.2019.100109.
[303] X. Chia, M. Pumera, Inverse Opal-like Porous $MoSe_x$ Films for Hydrogen Evolution Catalysis: Overpotential-Pore Size Dependence, ACS Appl. Mater. Interfaces 10 (2018) 4937–4945, https://doi.org/10.1021/acsami.7b17800.
[304] Z. Lei, S. Xu, P. Wu, Ultra-thin and porous $MoSe_2$ nanosheets: facile preparation and enhanced electrocatalytic activity towards the hydrogen evolution reaction, PCCP 18 (2016) 70–74, https://doi.org/10.1039/c5cp06483j.
[305] Y. Li, K. Yin, L. Wang, X. Lu, Y. Zhang, Y. Liu, D. Yan, Y. Song, S. Luo, Engineering MoS_2 nanomesh with holes and lattice defects for highly active hydrogen evolution reaction, Appl. Catal. B 239 (2018) 537–544, https://doi.org/10.1016/j.apcatb.2018.05.080.
[306] L. Wang, X. Li, J. Zhang, H. Liu, W. Jiang, H. Zhao, One-pot synthesis of holey MoS_2 nanostructures as efficient electrocatalysts for hydrogen evolution, Appl. Surf. Sci. 396 (2017) 1719–1725, https://doi.org/10.1016/j.apsusc.2016.11.235.
[307] S. Wang, H. Li, H. Sawada, C.S. Allen, A.I. Kirkland, J.C. Grossman, J.H. Warner, Atomic structure and formation mechanism of sub-nanometer pores in 2D monolayer MoS_2, Nanoscale 9 (2017) 6417–6426, https://doi.org/10.1039/c7nr01127j.
[308] J. Ge, L. Zhang, J. Xu, Y. Liu, D. Jiang, P. Du, Nitrogen photofixation on holey g-C_3N_4 nanosheets with carbon vacancies under visible-light irradiation, Chin. Chem. Lett. 31 (2019) 792–796, https://doi.org/10.1016/j.cclet.2019.05.030.
[309] S. Guo, Y. Zhu, Y. Yan, Y. Min, J. Fan, Q. Xu, Holey structured graphitic carbon nitride thin sheets with edge oxygen doping via photo-Fenton reaction with enhanced photocatalytic activity, Appl. Catal. B 185 (2016) 315–321, https://doi.org/10.1016/j.apcatb.2015.11.030.
[310] Y. Jiang, Z. Sun, C. Tang, Y. Zhou, L. Zeng, L. Huang, Enhancement of photocatalytic hydrogen evolution activity of porous oxygen doped g-C_3N_4 with nitrogen defects induced by changing electron transition, Appl. Catal. B 240 (2019) 30–38, https://doi.org/10.1016/j.apcatb.2018.08.059.
[311] S. Kang, L. Zhang, C. Yin, Y. Li, L. Cui, Y. Wang, Fast flash frozen synthesis of holey few-layer g-C_3N_4 with high enhancement of photocatalytic reactive oxygen species evolution under visible light irradiation, Appl. Catal. B 211 (2017) 266–274, https://doi.org/10.1016/j.apcatb.2017.04.050.
[312] Y. Li, R. Jin, Y. Xing, J. Li, S. Song, X. Liu, M. Li, R. Jin, Macroscopic Foam-Like Holey Ultrathin g-C_3N_4 Nanosheets for Drastic Improvement of Visible-Light Photocatalytic Activity, Adv. Energy Mater. 6 (2016) 1601273, https://doi.org/10.1002/aenm.201601273.
[313] Y. Li, Z. Ruan, Y. He, J. Li, K. Li, Y. Jiang, X. Xu, Y. Yuan, K. Lin, In situ fabrication of hierarchically porous g-C_3N_4 and understanding on its enhanced photocatalytic activity based on energy absorption, Appl. Catal. B 236 (2018) 64–75, https://doi.org/10.1016/j.apcatb.2018.04.082.
[314] Q. Liang, Z. Li, Z.-H. Huang, F. Kang, Q.-H. Yang, Holey Graphitic Carbon Nitride Nanosheets with Carbon Vacancies for Highly Improved Photocatalytic Hydrogen Production, Adv. Funct. Mater. 25 (2015) 6885–6892, https://doi.org/10.1002/adfm.201503221.
[315] Q. Liu, X. Wang, Q. Yang, Z. Zhang, X. Fang, A novel route combined precursor-hydrothermal pretreatment with microwave heating for preparing holey g-C_3N_4 nanosheets with high crystalline quality and extended visible light absorption, Appl. Catal. B 225 (2018) 22–29, https://doi.org/10.1016/j.apcatb.2017.11.044.
[316] X. She, L. Liu, H. Ji, Z. Mo, Y. Li, L. Huang, D. Du, H. Xu, H. Li, Template-free synthesis of 2D porous ultrathin nonmetal-doped g-C_3N_4 nanosheets with highly efficient photocatalytic H_2 evolution from water under visible light, Appl. Catal. B 187 (2016) 144–153, https://doi.org/10.1016/j.apcatb.2015.12.046.
[317] L. Shi, K. Chang, H. Zhang, X. Hai, L. Yang, T. Wang, J. Ye, Drastic Enhancement of Photocatalytic Activities over Phosphoric Acid Protonated Porous g-C_3N_4 Nanosheets under Visible Light, Small 12 (2016) 4431–4439, https://doi.org/10.1002/smll.201601668.
[318] T. Song, P. Zhang, T. Wang, A. Ali, H. Zeng, Alkali-assisted fabrication of holey carbon nitride nanosheet with tunable conjugated system for efficient visible-light-driven water splitting, Appl. Catal. B 224 (2018) 877–885, https://doi.org/10.1016/j.apcatb.2017.11.039.
[319] T. Song, P. Zhang, T. Wang, A. Ali, H. Zeng, Vopor-polymerization strategy to carbon-rich holey few-layer carbon nitride nanosheets with large domain size for superior photocatalytic hydrogen evolution, Appl. Surf. Sci. 464 (2019) 195–204, https://doi.org/10.1016/j.apsusc.2018.09.062.
[320] D. Zhang, Y. Guo, Z. Zhao, Porous defect-modified graphitic carbon nitride via a facile one-step approach with significantly enhanced photocatalytic hydrogen evolution under visible light irradiation, Appl. Catal. B 226 (2018) 1–9, https://doi.org/10.1016/j.apcatb.2017.12.044.
[321] J.-W. Zhang, S. Gong, N. Mahmood, L. Pan, X. Zhang, J.-J. Zou, Oxygen-doped nanoporous carbon nitride via water-based homogeneous supramolecular assembly for photocatalytic hydrogen evolution, Appl. Catal. B 221 (2018) 9–16, https://doi.org/10.1016/j.apcatb.2017.09.003.
[322] S. Zhao, Y. Zhang, Y. Zhou, Y. Wang, K. Qiu, C. Zhang, J. Fang, X. Sheng, Facile one-step synthesis of hollow mesoporous g-C_3N_4 spheres with ultrathin nanosheets for photoredox water splitting, Carbon 126 (2018) 247–256, https://doi.org/10.1016/j.carbon.2017.10.033.